JPL Publication 87-38

Airborne Visible/Infrared Imaging Spectrometer (AVIRIS)

A Description of the Sensor, Ground Data Processing Facility, Laboratory Calibration, and First Results

Gregg Vane
Editor

November 15, 1987

National Aeronautics and
Space Administration

Jet Propulsion Laboratory
California Institute of Technology
Pasadena, California

The research described in this publication was carried out by the Jet Propulsion Laboratory, California Institute of Technology, under a contract with the National Aeronautics and Space Administration.

ABSTRACT

The papers in this document were presented at the Imaging Spectroscopy II Conference of the 31st Annual International Symposium on Optical and Optoelectronic Applied Science and Engineering, in San Diego, California, on August 20 and 21, 1987. They describe the design and performance of the Airborne Visible/Infrared Imaging Spectrometer (AVIRIS) sensor and its subsystems, the ground data processing facility, laboratory calibration, and first results.

FIRST AVIRIS COLOR IMAGE

This false color image of Mountain View, California, was acquired with the Airborne Visible/Infrared Imaging Spectrometer (AVIRIS) aboard the NASA Ames U-2 aircraft from approximately 20 km. The image data were processed at the Jet Propulsion Laboratory AVIRIS Ground Data Processing Facility. Using radiometrically corrected data, the image was produced from three 10-nm-wide spectral bands centered at 557, 665, and 910 nm. These spectral bands were assigned the colors blue, green, and red, respectively. In this rendition, red corresponds to healthy vegetation and blue/green corresponds to water. Note the degree of shading in the water in the southern part of San Francisco Bay and in the evaporation ponds to the east of Moffett Field (the image is oriented with north to the right). This shading is indicative of variations in the concentration and composition of suspended particulates in the water. Note also the spatial quality of the image. No geometric rectification was applied beyond the roll correction performed on board the aircraft. The dikes between the evaporation ponds are approximately 20 m wide, which is the ground instantaneous field of view of AVIRIS.

CONTENTS

INTRODUCTION

The Airborne Visible/Infrared Imaging Spectrometer (AVIRIS) began its first summer of operations aboard the NASA Ames U-2 research aircraft in 1987, three years after design and construction of the instrument began. The papers in this document describe in detail the major subsystems of AVIRIS, the AVIRIS ground data processing facility, the laboratory calibration performed on the instrument prior to the 1987 summer flight season, and some first results obtained from the sensor over test sites in California and Nevada. The papers, totalling ten in all, were presented at the Imaging Spectroscopy II Conference at the annual meeting of the Society of Photo-Optical Instrumentation Engineers in San Diego, California, in August 1987.

AVIRIS is the second in a series of imaging spectrometers for earth remote sensing under development at the Jet Propulsion Laboratory for NASA. While the earlier instrument, the Airborne Imaging Spectrometer (AIS), was an engineering test bed for infrared detector arrays for spaceborne imaging spectrometers, AVIRIS was designed to be an operational sensor for routine collection of high calibre scientific data until an observatory-class imaging spectrometer in earth orbit, the High Resolution Imaging Spectrometer (HIRIS), becomes available on the Earth Observing System (Eos) in the mid-1990s. The first season of operations with AVIRIS was dedicated to a NASA-sponsored data evaluation and technology assessment program to determine the full performance potential of the AVIRIS system. Insight gained from this program and the engineering knowledge gained by the AVIRIS project during calibration and flight testing will be used during the 1987-88 winter in guiding modifications to the sensor that are designed to bring the sensor and data processing facilities to their full operating potential. Improvements in signal stability and signal-to-noise performance, for example, are expected during the final modification phase. The goal is to place AVIRIS in its fully operational mode for a vigorous science data collection campaign in 1988, and to continue in that mode for the next several years, providing the science community with the necessary data for developing the means of efficiently utilizing the data to be provided by HIRIS and similar spaceborne instruments.

Gregg Vane
Jet Propulsion Laboratory

A system overview of the Airborne Visible/Infrared Imaging Spectrometer (AVIRIS)

Wallace M. Porter and Harry T. Enmark
Jet Propulsion Laboratory, California Institute of Technology
4800 Oak Grove Drive, Pasadena, California 91109

ABSTRACT

The AVIRIS instrument has been designed to do high spectral resolution remote sensing of the Earth. Utilizing both silicon and indium antimonide line array detectors, AVIRIS covers the spectral region from 0.41 μm to 2.45 μm in 10-nm bands. It was designed to fly aboard NASA's U2 and ER2 aircraft, where it will simulate the performance of future spacecraft instrumentation. Flying at an altitude of 20 km, it has an instantaneous field of view (IFOV) of 20 m and views a swath over 10 km wide. With an ability to record 40 minutes of data, it can, during a single flight, capture 500 km of flight line.

1.0 INTRODUCTION

The science of remote sensing has advanced especially rapidly over the last several years through observational research using increasingly capable sensor systems. As technology has advanced, making possible sensors of higher spatial, spectral, and radiometric performance, the ability to discriminate among features on the Earth's surface has also advanced. Just as the 7-band Thematic Mapper aboard Landsats 4 and 5 represented a significant step beyond the earlier 4-channel Multispectral Scanner, the Airborne Visible/Infrared Imaging Spectrometer (AVIRIS) technology described here, with its 224 contiguous spectral channels, will provide a quantum leap ahead of instruments now available and initiate a new, extremely powerful class of Earth remote sensing instruments.

Results from recent experiments with the high spectral resolution Airborne Imaging Spectrometer (AIS)[1] have shown the utility of using this class of instrument for Earth surface material discrimination and identification.[2] As a result of this research, AVIRIS has been designed to take advantage of the typically narrow diagnostic absorption features of these surface materials throughout the 0.4-μm to 2.45-μm region of the spectrum by providing 224 contiguous spectral bands 10 nm wide over this region.

The origins of imaging spectrometry at the Jet Propulsion Laboratory (JPL) lie in the design of the Near Infrared Mapping Spectrometer (NIMS) to be flown on the Galileo spacecraft in 1989.[3] NIMS will use cross-track scanning and platform motion to generate spatial information together with a linear array of discrete detectors to provide signals from spectral energy dispersed by a grating in the spectrometer. The AVIRIS concept grew from the NIMS experience, from development and use of the AIS, from development activity in indium antimonide line array detectors, and from work designing an instrument for the USDA Forest Service called FLAME, which used scanning infrared optics and which served as a starting point for the AVIRIS scanner design.

The second-generation instrument described here will image the entire spectral region from 0.4 μm to 2.45 μm over a swath 614 pixels wide, which, besides providing high spectral resolution spectra of each pixel, permits feature identification and location from the data. The data base acquired from the AVIRIS program should make possible the next major step in Earth remote sensing--an Earth-orbiting imaging spectrometer.

2.0 CONCEPT

The AVIRIS instrument is essentially a group of four spectrometers that view the ground through a scanner while being carried over the test site in an aircraft. At any one moment the spectrometers are viewing a spot on the ground 20 meters square. This pixel is viewed simultaneously in 224 spectral bands. A spatial image is built up through the scanner motion, which defines an image line 614 pixels wide perpendicular to the aircraft direction, and through the aircraft motion, which defines the length of the image frame (see Figure 1). The data are collected on a tape recorder for later analysis.

The recorded data set forms a data cube of which two axes represent spatial dimensions and the third represents a spectral dimension, as shown in Figures 1 and 2. The spectral data carry information corresponding to the composition of the ground being viewed and the intervening atmosphere. Computer processing of the data will produce an image of the test site in any of the 224 spectral bands, the spectrum corresponding to any of the pixels in the scene, or an image of the test site with those pixels corresponding to a perpendicular spectra marked off.

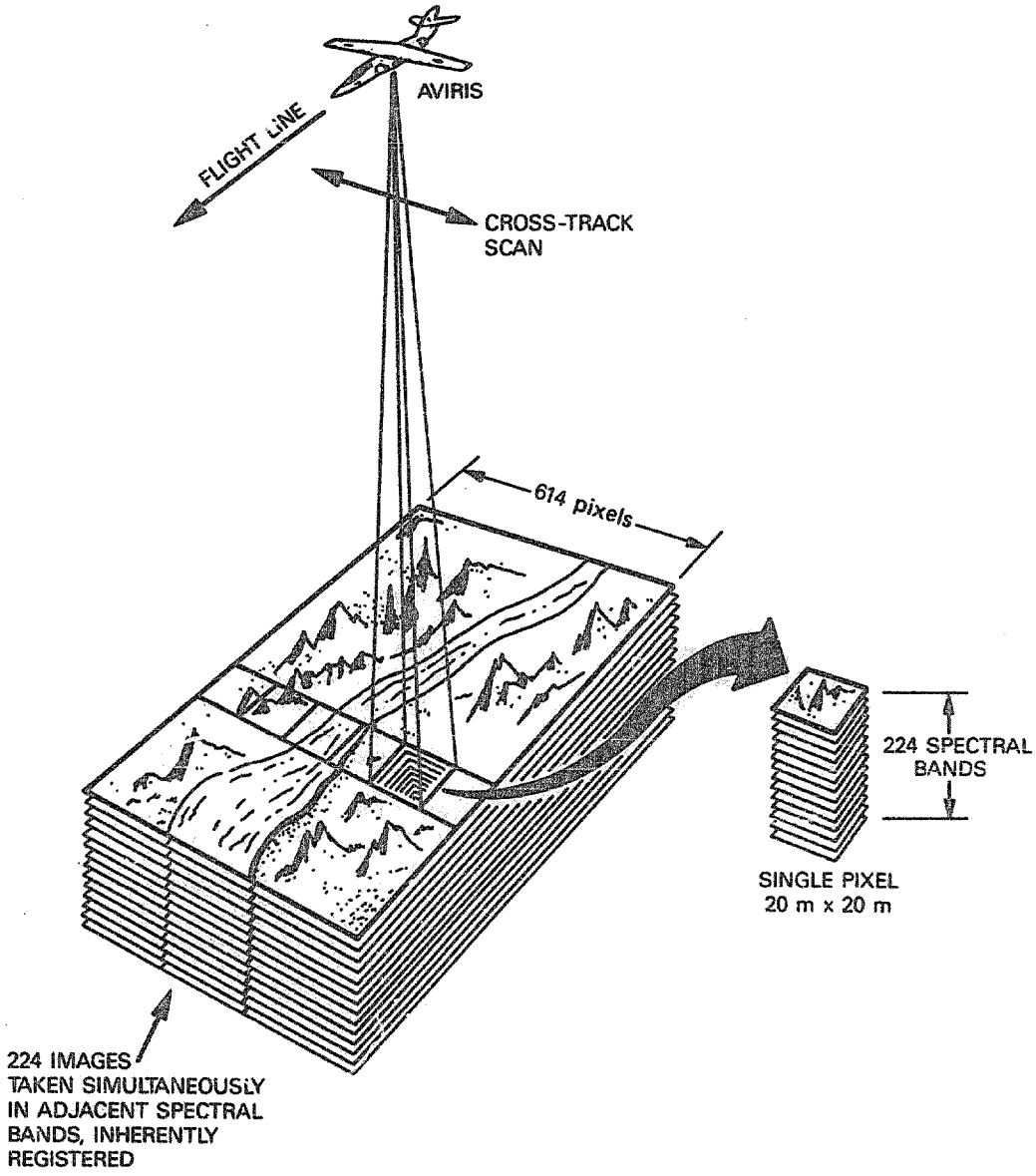

Figure 1. AVIRIS data collection.

3.0 DESIGN CRITERIA

The performance parameters for the AVIRIS instrument were determined, for the most part, from several key science requirements. Some compromise was necessary to accommodate the environmental constraints imposed by the U2 aircraft and to match the performance available from the chosen detectors.

The spectral sampling requirement for the AVIRIS instrument was determined by two key science requirements: The desire to detect shifts in the chlorophyll spectrum on the order of 10 to 40 nm at 0.7 μm, and the desire to resolve spectral features as narrow as the kaolinite doublet at 2.2 μm. Previous work with the AIS instrument had determined that the 10-nm sampling chosen for AVIRIS would be adequate. The instrument's longwave cutoff point of 2.45 μm was chosen to avoid viewing thermal emissions.

Signal-to-noise ratio (S/N) requirements were determined by analysis to be at least 100 to 1 at 0.7 μm for detection of the chlorophyll shift and 50 to 1 for detection of the kaolinite doublet. These requirements were for a surface albedo of 0.5 viewed through a standard LOWTRAN atmosphere with 23-km visibility.

The ground instantaneous field of view (GIFOV) was chosen to be 20 m. A GIFOV of 10 m would have been preferred, but with the scan rate already set at 12 scans/sec by the aircraft flight parameters and the scanner dimensions set by a requirement to use an existing scanner, this would have required a shorter detector integration time than could

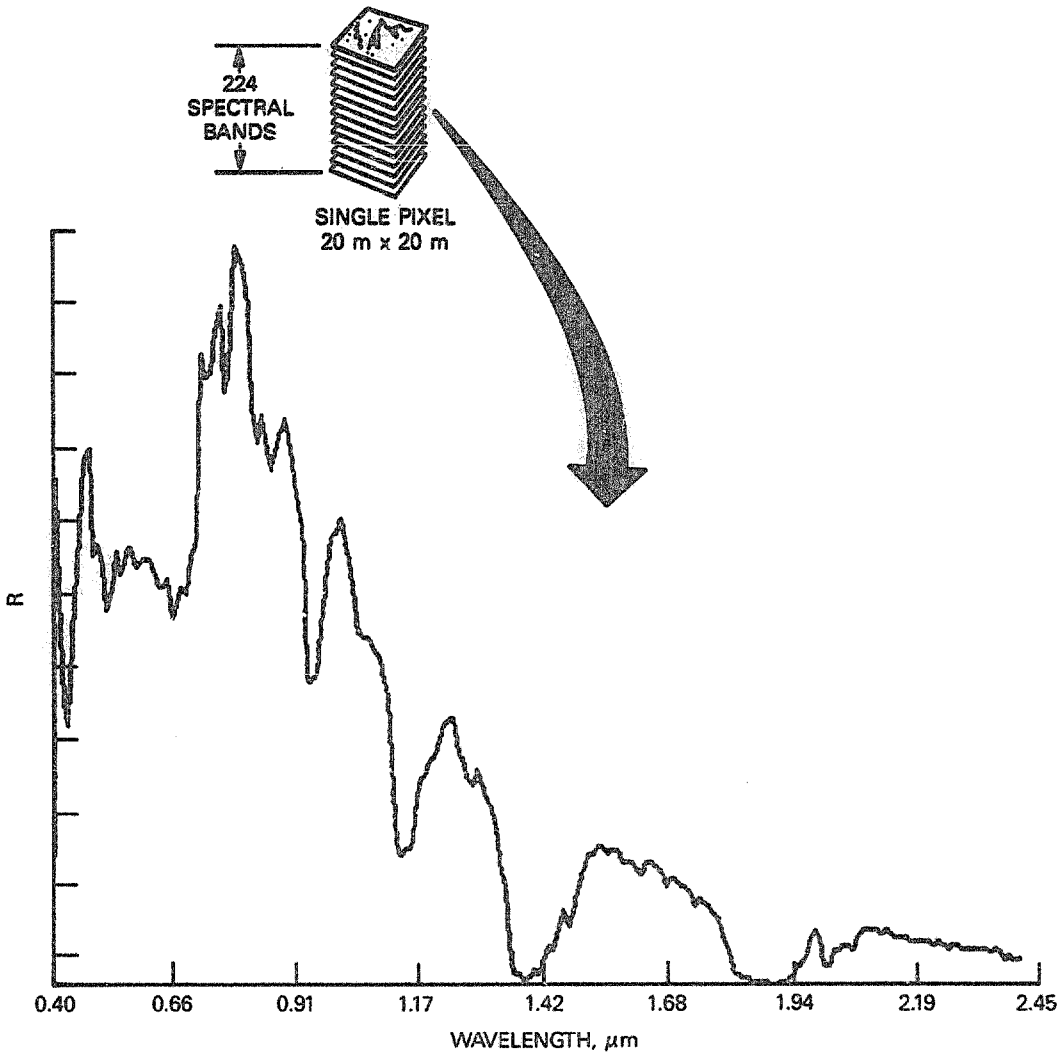

Figure 2. Spectrum from single pixel.

have been achieved. The field of view (FOV) was chosen to be 30 deg. This provides 614 spatial pixels in the scan direction and a swath width of over 10 km.

One remaining consideration that influenced the basic design of AVIRIS was the need to keep the instrument's operation as simple as possible. The pilot is confined in a high altitude suit which makes it awkward for him to operate the instrument. In addition, he has a full-time job simply flying the aircraft. For these reasons, AVIRIS has only two basic control functions--power and record.

4.0 INSTRUMENT DESCRIPTION

AVIRIS is modular in construction, consisting of six optical subsystems and five electrical subsystems. The optical subsystems (a scanner, four spectrometers, and a calibration source) are coupled together through optical fibers. The use of optical fibers to interconnect optics (thought to be unique in this application) was necessitated by the need to incorporate four separate spectrometers while keeping each spectral band less than one octave wide, to avoid spectral contamination from grating overlap. This concept provided additional benefits in that it greatly simplified the mechanical layout of the instrument and allowed the various subsystems to be aligned and tested independently of each other.

The electronics are packaged by major function, and include the signal chain, the digital control section, data buffers, the roll correction gyro, and the power supplies. This provides considerable isolation between the signal chains and other noisier circuitry. Full advantage was taken of the U2's and ER2's payload capacity to provide complete RFI shielding for each package.

Figure 3 shows the AVIRIS instrument and the placement of its major subsystems, including the scanner and foreoptics; the spectrometers and dewars; the electronic pack-

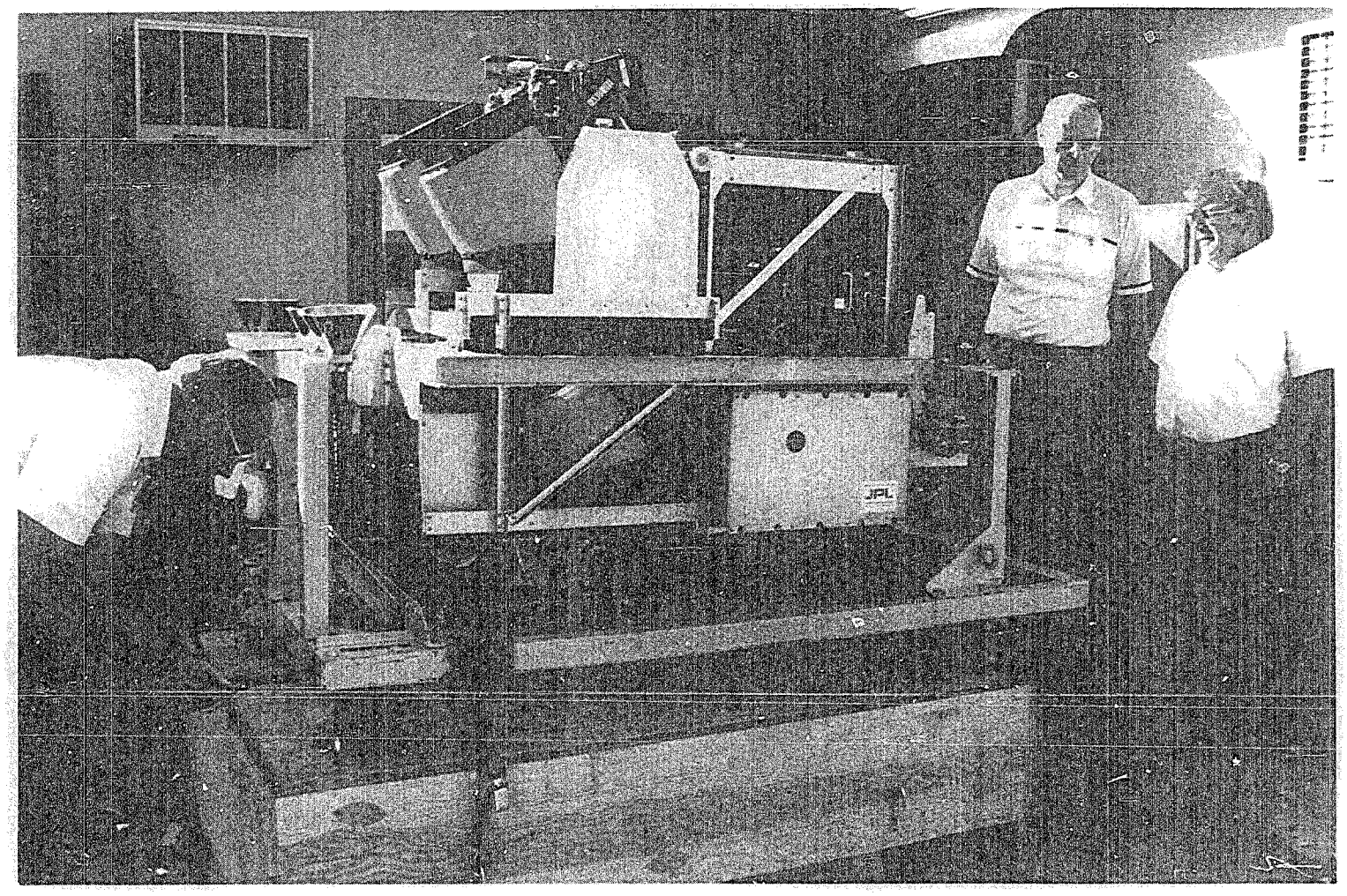

Figure 3. AVIRIS.

ages; and the tape recorder. The weight of the instrument is 720 lbs, and the instrument fits in an envelope 33 in. wide by 63 in. long by 46 in. high.

A functional block diagram of AVIRIS that indicates the relationship between the major subsystems is shown in Figure 4. The instrument is operated under the control of the

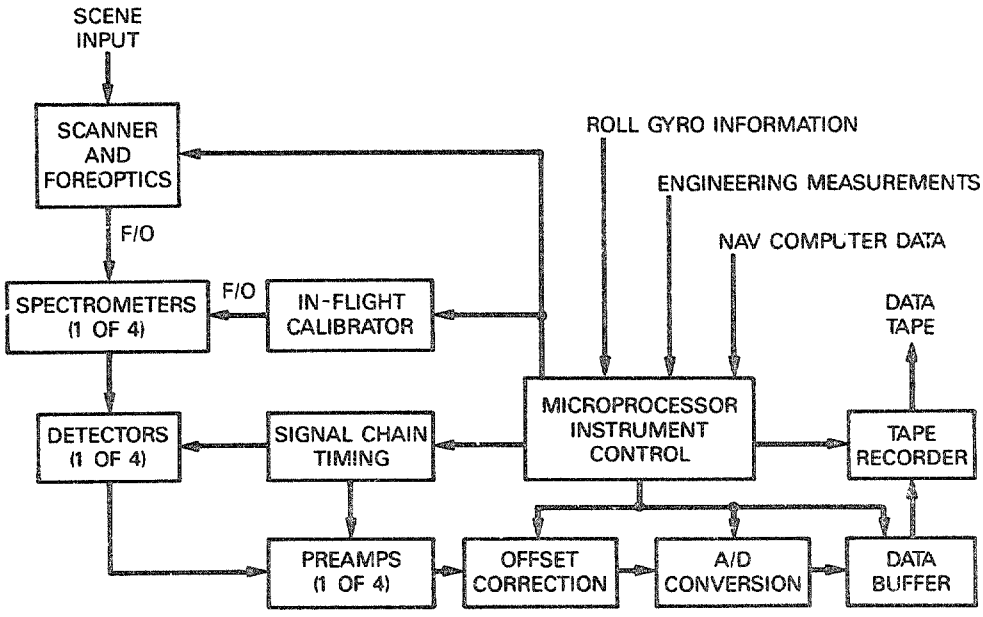

Figure 4. AVIRIS functional block diagram.

digital control subsystem (the heart of which is an Intel 8085A-2 microprocessor) in response to inputs from the power switch and the record switch. When the instrument is powered up, it goes through an initialization sequence, which includes synchronization of the shutters in the foreoptics and onboard calibrator, homing of the calibrator's filter wheel, and a self-check of the instrument's status. Included in the initialization sequence is the focusing of the foreoptics to accommodate changes due to temperature.

When the record switch is actuated by the pilot, the control section conditions the instrument by doing an offset correction for each of the 224 detector elements and resetting the roll correction gyro. The control section then puts the instrument through a calibration sequence measuring dark current and the calibrator output through each of its filter positions prior to the start of data recording. A similar calibration sequence is performed at the end of the data run. The calibration data are recorded on the high-density tape (HDT) on which the science data are recorded.

The control subsystem also interfaces with the plane's navigation computer to receive flight parameter data, which are recorded along with the science and calibration data. Data pertaining to the operation of the instrument are also recorded.

Viewing of the scene is done with the scanner operating at a rate of 12 scans/sec. The scanner operates in a scan-flyback mode with an efficiency of 70% and is momentum-compensated. During the flyback time, the dark-current performance of the detectors is measured and recorded. To avoid recording blank spots on the tape, the data taken during the active portion of each scan are rate-buffered and sent to the tape recorder during both the scan and flyback period. With a data rate of 17 Mbits/sec, the recorder can record 40 minutes of data on a flight. Four data channels, representing each of the four spectrometers, are read simultaneously from the scanner, requiring further buffering to get the output of each of the 224 spectrometer detector elements in the proper order on the HDT.

The scanner operates continuously, with its drive phase locked to the data system's master clock. An encoder signals the start of each scan. Aircraft roll compensation is accomplished by matching this start signal to the output of the roll gyro and delaying the start of data collection on the scan line enough to put the center pixel in the nadir position.

A foreoptics assembly mounted on top of the scanner collects the light from the pixel being viewed and sends it to the four spectrometers via four optical fibers. The four optical fibers, each 200 μm, or one pixel, in diameter, lie in a row looking at adjacent pixels on the ground. Buffers in the digital section recombine their output in the proper sequence before the data are sent to the tape recorder. The fibers carrying the visible and near-infrared part of the spectrum to their respective spectrometers are made of silica glass. The other two fibers, which carry the shortwave infrared to their respective spectrometers, are made of fluoride glass.

It is necessary to compensate for thermal focus shifts in the scanner and foreoptics by adjusting the focus position of the fiber bundle. This is done under microprocessor control by moving the end of the fiber bundle in and out with a stepper motor. The microprocessor measures the temperature of the optical assembly and adjusts the focus accordingly, using a stored table of position values. Focus is maintained over a temperature range of -30 deg to +30 deg C.

The four spectrometers are heated to maintain proper focus in the aircraft environment. Each spectrometer takes the signal received from the foreoptics and focuses a portion of its spectral content on a line array detector mounted in a dewar. The visible portion of the spectrum is monitored by a 32-element line array silicon detector. The short-wavelength infrared is monitored in the other three spectrometers by three 64-element line array indium antimonide detectors.

The aircraft flight parameters and the spatial imaging requirements define the detector integration time to be 87 μsec. This has presented some challenges in the instrument's design. The readout rate of the detectors is being pushed to near its limit, requiring special attention to be paid to the timing stability of the detector drive waveforms as well as to transients in the detector output waveforms.

The short integration time produces a small output signal on the order of only a few percent of what the detectors are capable of. Because of this, element-to-element variations in the detector outputs are a significant fraction of the full-scale signal. To keep the signal chain from saturating on these extraneous signals, the onboard microprocessor measures the dark current offset of each detector element just prior to a data run and applies these offsets as a correction to the data as they are being collected. An additional concern is created by the fact that changes in the integrated dark current

corresponding to a temperature change of just a few degrees centigrade will also drive the signal chain into saturation. To prevent this, the dewars, which operate at liquid nitrogen temperatures, are fitted with constant pressure relief valves. Even though the ambient pressure changes during a flight from 14.7 psi on the ground to 4.5 psi at altitude, the pressure inside the dewars varies no more than a few tenths of a psi so that the detector temperatures are stable within one degree centigrade.

A detailed listing of the AVIRIS instrument parameters appears in the appendix.

5.0 CURRENT INSTRUMENT PERFORMANCE

The AVIRIS instrument is currently in the field for its first flight season. The calibration data taken prior to releasing it for flight and the flight data taken this season show the instrument to be working within all of its design requirements except for its signal-to-noise (S/N) performance. This S/N performance is summarized in Table 1. The requirement at 0.7 μm has been met. While the requirement at 2.2 μm has yet to be met, this performance has been adequate to allow the detection of the kaolinite doublet in the data taken to date. A comparison of the measured to predicted S/N indicates that additional performance can be achieved. The shortfall in S/N is due to excess noise and not a deficit of signal. Several noise mechanisms have been identified and are scheduled to be addressed this fall during an upgrade of the instrument.

Table 1. Signal-to-Noise Performance

Band	Wavelength (μm)	Required S/N	Measured S/N[a]
A	0.7	100:1	150:1
B	1.0	None	140:1
C	1.6	None	70:1
D	2.2	50:1	30:1

[a] The measured performance is for integrating sphere data corrected for viewing a scene with 50% albedo through a standard mid-latitude, midsummer atmosphere with 23-km visibility.

The geometric performance of AVIRIS meets all of the design requirements; an example of its high quality can be seen in the image shown in Figure 5. This photograph, which represents one of 224 spectral bands, was processed by only a simple stretch. The picture is a view of a portion of San Francisco in the 1.026-μm spectral band. The Golden Gate Bridge, which is about one AVIRIS pixel wide, shows clearly, as do the two support towers. Note the lack of geometrical distortion and the uniform shading across the width of the picture. Geometric performance as measured during calibration is presented in Table 2.

The spectral performance of AVIRIS also meets its design requirements and is presented in Table 3.

An additional difficulty has been encountered with the AVIRIS instrument this first flight season; this difficulty has to do with the stability of the spectrometers' signal output. The temperature control currently being used does not maintain the spectrometers completely in focus. Additionally, the method used to mount the spectrometers to the instrument frame distorts their geometry and lowers their performance. These problems will be corrected during the instrument upgrade activity this fall.

6.0 CONCLUSION

The successful design and implementation of the Airborne Visible/Infrared Imaging Spectrometer places the remote sensing science community on the threshold of a new era. In spite of the limitations noted in instrument performance during the initial operating season, early data returns indicate great utility to the science community. After completion of the NASA-sponsored performance evaluation period in 1987, upgrades will be performed to the instrument which will bring it to a fully operational state. AVIRIS is expected to be the major source of high spectral resolution imagery until the High-

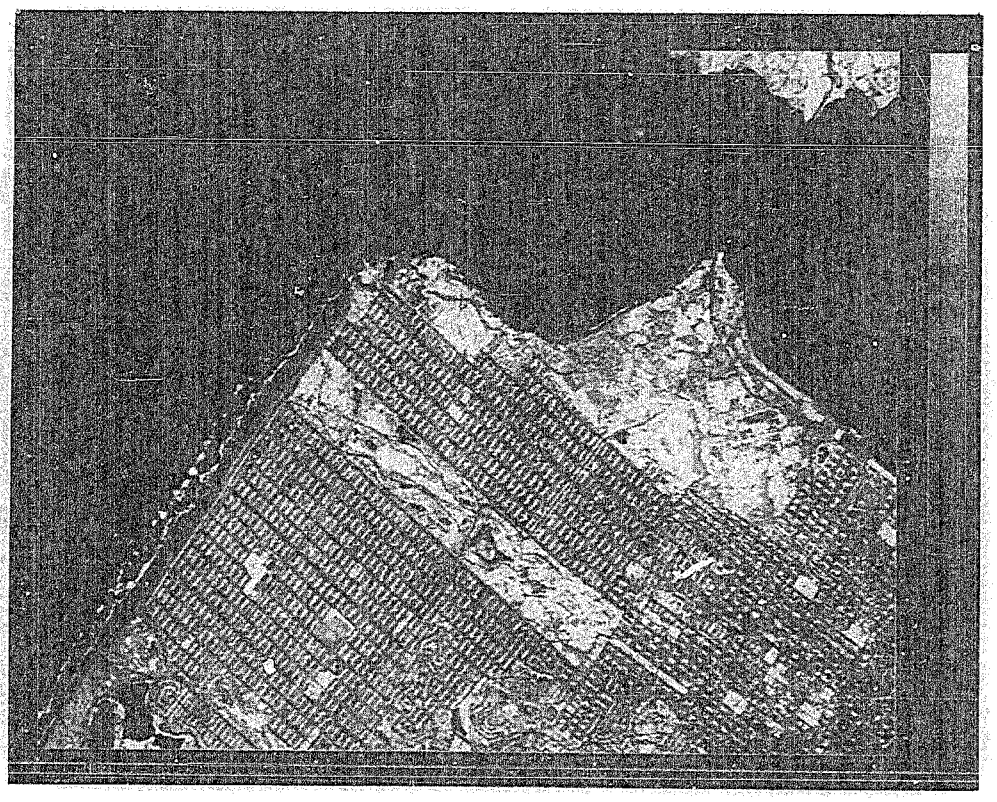

Figure 5. AVIRIS data product view of San Francisco in the 1.026-μm spectral band.

Table 2. Geometric Performance

Parameter	Required Performance	Measured Performance
Swath width (from U2)	≥ 10 km	10.5 km
IFOV	≤ 1 mrad	0.95 mrad
Spatial oversample	≥ 15%	17%
Scan dynamics		
Scan rate	12 scans/sec	12 scans/sec
Cumulative pixel position error over scan (pixel size = 1.0 mrad)	0.5 mrad	0.26 mrad
Maximum pixel-to-pixel position error	0.1 mrad	0.06 mrad
Angular motion of scan drive housing due to vibration	0.1 mrad	0.01 mrad

Table 3. Spectral Performance

Parameter	Required Performance	Measured Performance
Spectral coverage	0.4 to 2.4 μm	0.41 to 2.45 μm
Spectral sampling interval	≤ 10 nm	9.6 to 9.9 nm

Resolution Imaging Spectrometer (HIRIS) is launched on the NASA Earth Observing System (Eos) in the mid-1990s.

7.0 REFERENCES

1. G. Vane, A. F. H. Goetz, and J. B. Wellman, 1983, Airborne Imaging Spectrometer: A New Tool for Remote Sensing, Proceedings of the 1983 International Geoscience and Remote Sensing Symposium, IEEE Catalog No. 83CH1837-4.

2. G. Vane, 1985, High Spectral Resolution Remote Sensing of the Earth, Sensors V.2, No. 12, pp. 11-20.

3. I. Aptaker, in press, Near-Infrared Mapping Spectrometer for Investigation of Jupiter and its Satellites (SPIE Paper 834-24), proceedings of the SPIE conference held on August 17-21, 1987, in San Diego, California.

8.0 ACKNOWLEDGMENT

The research described in this paper was carried out by the Jet Propulsion Laboratory, California Institute of Technology, under a contract with the National Aeronautics and Space Administration.

9.0 APPENDIX: AVIRIS INSTRUMENT PARAMETERS

MISSION PARAMETERS
- Flight altitude - 20 km
- Ground-track velocity - 740 km/hr
- Velocity/height - 20 knots/km

PHYSICAL CHARACTERISTICS
- Weight - 720 lbs
- Width - 33 in.
- Length - 63 in.
- Height - 46 in.
- Window - 16.8 in. in diameter
  2.75 in. below scanner
- Power requirements - 28 VDC, 41 amps
  115 VAC, 400 Hz, 1 phase, 0.5 KVA
- Thermal operating environment - 0 to 30 deg C

OPTICS

Foreoptics
- FOV - 33 deg
- Active FOV - 30 deg
- IFOV - 1 mrad
- Effective focal length - 19.76 cm
- Effective pupil diameter - 14.5 cm
- Performance - Point source at infinity, 90% energy in 50 μm
- A-Omega Product - 1.297×10^{-4} $cm^2 srad$

Fiberoptics
- Material - Silica (spectrometers A and B)
  Fluoride glass (spectrometers C and D)
- Diameter - 200 μm
- Numerical aperture - 0.45

Spectrometers

Spectrometer A
- Design - Double-pass Schmitt
- Wavelength range - 0.41 to 0.70 μm
- Sampling interval - 9.7 nm
- Number of channels - 31
- Grating - 117.65 l/mm

Spectrometer B
- Design - Double-pass Schmitt
- Wavelength range - 0.68 to 1.27 μm
- Sampling interval - 9.5 nm
- Number of channels - 63
- Grating - 128.205 l/mm

Spectrometer C
Design - Double-pass Schmitt
Wavelength range - 1.25 to 1.86 μm
Sampling interval - 9.8 nm
Number of channels - 63
Grating - 124.2236 l/mm
Spectrometer D
Design - Double-pass Schmitt
Wavelength range - 1.84 to 2.45 μm
Sampling interval - 9.8 nm
Number of channels - 63
Grating - 128.6 l/mm

Calibrator
Light source - Halogen lamp
Filters - Blank
Wide-band low level
Wide-band high level
Holmium oxide

DETECTORS
Spectrometer A
Type - Line array
Number of elements - 32
Material - Silicon
Integration time - 87 μsec
Detector active area - 200 x 200 μm
Dead space between elements - 30 μm
Spectrometer B
Type - Line array
Number of elements - 64
Material - Indium antimonide
Integration time - 87 μsec
Detector active area - 200 x 200 μm
Dead space between elements - 30 μm
Spectrometer C
Type - Line array
Number of elements - 64
Material - Indium antimonide
Integration time - 87 μsec
Detector active area - 200 x 200 μm
Dead space between elements - 30 μm
Spectrometer D
Type - Line array
Number of elements - 64
Material - Indium antimonide
Integration time - 87 μsec
Detector active area - 200 x 200 μm
Dead space between elements - 30 μm

DEWARS
Cryogen - LN_2
Detector positional stability - 500 μin., all axes
Hold time - 4 hr
Operating position - No spillage for 60-deg tilt
Operating pressure - 15.7 psia

SIGNAL PROCESSING/DATA HANDLING
Signal Chains
Number - 4
Gain - Spectrometer A: A_V = 235
Spectrometer B: A_V = 375
Spectrometer C: A_V = 385
Spectrometer D: A_V = 750
Noise - 17-μV rms over 625-kHz equivalent noise bandwidth
Offset - 20% of full scale
Offset stability - Short-term (15-min) offset drift and nonuniformity is compensated to within 20% of full-scale signal
A/D converter - 10 bits
Data Formatting
Science data buffer size - 192 kbits
Detector read rate - 1.37 μsec/spectral element

Spectral elements/pixel - 224
Pixels/scan - 614

Tape Recorder
Make - Ampex AHBR1700i high-bit-rate airborne recording system
Write rate - 17 Mbits/sec
Record time/flight - 40 min

MECHANISMS

Scanner
Scan rate - 12 scans/sec
Scan efficiency - 70%
Cumulative pixel position error - 0.26 GIFOV over scan (pixel size = 1.0 mrad)
Nonrepetitive misalignment - 0.4 GIFOV accumulative between corresponding GIFOVs over line in adjacent scan lines
Nonrepetitive center to center - 0.06 GIFOV variations in sample spacing
Actuator - 3-phase induction motor
Controlling parameter - Master clock
Drive - Cam and follower with momentum compensation

Focus
Temperature range - +30 to -30 deg C
Accuracy - 20 μm
Resolution - 2 μm
Actuator - Stepper motor
Controlling parameter - Foreoptics temperature

Shutter
Shutter rate - 12 Hz
Duty cycle - 70% open
Actuator - Stepper motor

Filter wheel
Number of positions - 4
Actuator - Stepper motor

Airborne Visible/Infrared Imaging Spectrometer (AVIRIS)

Spectrometer Design and Performance

by

Steven A. Macenka
Michael P. Chrisp, Ph.D.

Jet Propulsion Laboratory
California Institute of Technology
Pasadena, California

ABSTRACT

The development of the Airborne Visible/Infrared Imaging Spectrometer (AVIRIS) has been completed at the Jet Propulsion Laboratory, California Institute of Technology. This paper outlines the functional requirements for the spectrometer optics subsystem, and describes the spectrometer optical design. The optical subsystem performance is shown in terms of spectral modulation transfer functions, radial energy distributions and system transmission at selected wavelengths for the four spectrometers. An outline of the spectrometer alignment is included.

1. INTRODUCTION

The Airborne Visible/Infrared Imaging Spectrometer has been developed at the Jet Propulsion Laboratory as a NASA facility instrument to fly on a U2 aircraft. Its purpose is to provide high quality spectral data for remote sensing. The science requirements that had to be met to achieve this are given in Table 1. The spectral range extending from 0.4 μm to 2.4 μm was divided into four parts to provide a uniform signal-to-noise ratio over the whole spectral range. This division was required to maintain the diffraction grating efficiency over the given spectral ranges. One of the prime objectives of the instrument was mineral identification from spectral signatures. To do this, the spectral sampling interval was chosen based on the requirement to resolve the kaolinite doublet at 2.2 μm wavelength, shown in Fig. 1. The intensity modulation of this spectral feature is ≤ 0.05 at a spectral frequency of 0.04 cycles/nanometer (c/nm), or, in terms of spatial frequency in the detector plane, it is 2.0 c/mm. To resolve this doublet required that the modulation transfer function MTF ≥ 0.5 at 2.0 c/mm for the AVIRIS spectrometers. This optical performance guarantees the resolution of the kaolinite doublet and provides an acceptable instrument spectral responsivity function, illustrated for a Gaussian point spread function in Fig. 2.

Table 1. AVIRIS Science Requirements

Spectral Coverage	0.4 to 2.4 μm	Swath Width (from U2)	≥ 10 km
Spectral Sampling Interval	≤ 10 nm	Spatial Oversample	≥ 15%
Signal-to-noise Ratio	≥ 100:1 at 0.7 μm	Calibration	
	≥ 50:1 at 2.2 μm	Relative	0.5%
Instantaneous Field of View (IFOV)	≤ 1 mrad	Absolute	5% to 10%

The AVIRIS optics subsystem consists of a whiskbroom scanner connected by optical fibers to four spectrometers, shown schematically in Fig. 3. As the prismatic scan mirror rotates, the field-of-view is swept across the flight path. In the spectrometers the dispersed spectrum is imaged on cooled linear arrays of silicon detectors for the 0.4 μm to 0.7 μm spectral range and on indium antimonide arrays for the 0.7 μm to 2.45 μm spectral range. An onboard reference source is also connected by optical fibers to the spectrometers, providing information on spectral and radiometric calibration.

2. SPECTROMETER OPTICAL DESIGN

An all-reflective decentered aperture Schmidt design was selected for the AVIRIS spectrometers. The optical schematics of the AVIRIS spectrometers are shown in Fig. 4.

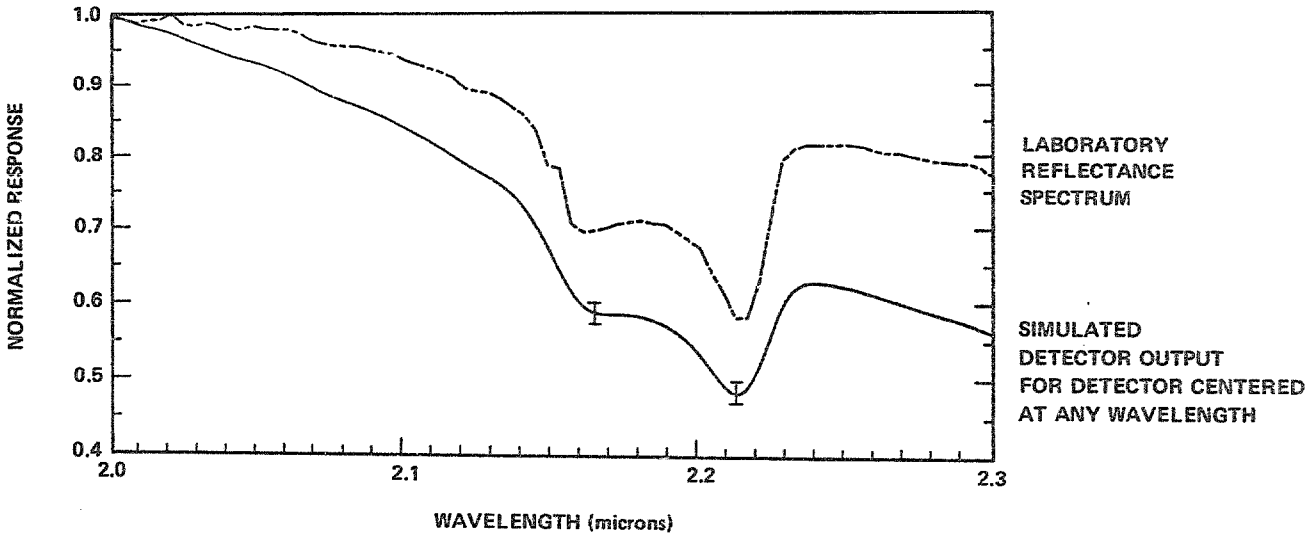

Fig. 1. Kaolinite Doublet Detection

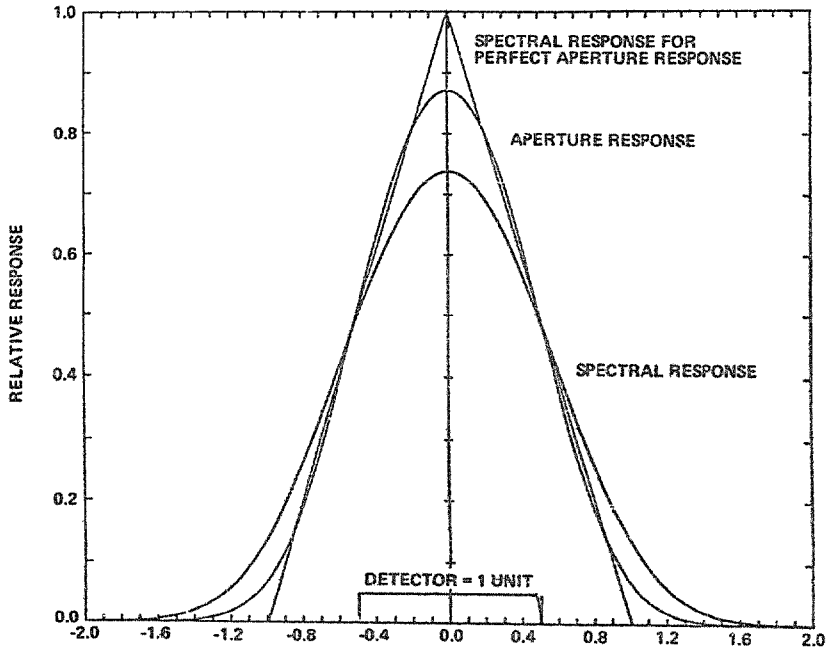

Fig. 2. Aperture Slit Detector Size

The radiant energy emerging from the fiber optic is collimated by a spherical mirror, which is used in double pass in this particular configuration. The reflective diffraction grating is located on the decentered aperture Schmidt corrector at the center of curvature of the collimating mirror. The grating mask forms the aperture stop of the spectrometer. All four AVIRIS spectrometers have the same basic optical layout and only the grating tilt changes significantly from Spectrometers "A" to "D", as required by the spectral range covered by each of the spectrometers. In this configuration, the Schmidt corrector plate is tilted with respect to the optical axis. The optimum surface figure for this particular configuration is an anamorphic aspheric surface. At the time of the AVIRIS implementation, the fabrication of such a surface was too risky and prohibitively expensive, so rotationally symmetric aspheric surfaces were selected for the AVIRIS spectrometer designs. This compromise resulted in a slight degradation of the overall optical performance but still stayed within the system specifications.

The AVIRIS spectrometer optical parameters are listed in Table 2. Shown in this table are the aspheric coefficients of the grating. The grating surface is given by the equation,

$$z = \frac{ch^2}{1 + \left[1 - (1+K)\ c^2h^2\right]^{1/2}} + Ah^4 + Bh^6 + Ch^8 + Dh^{10}$$

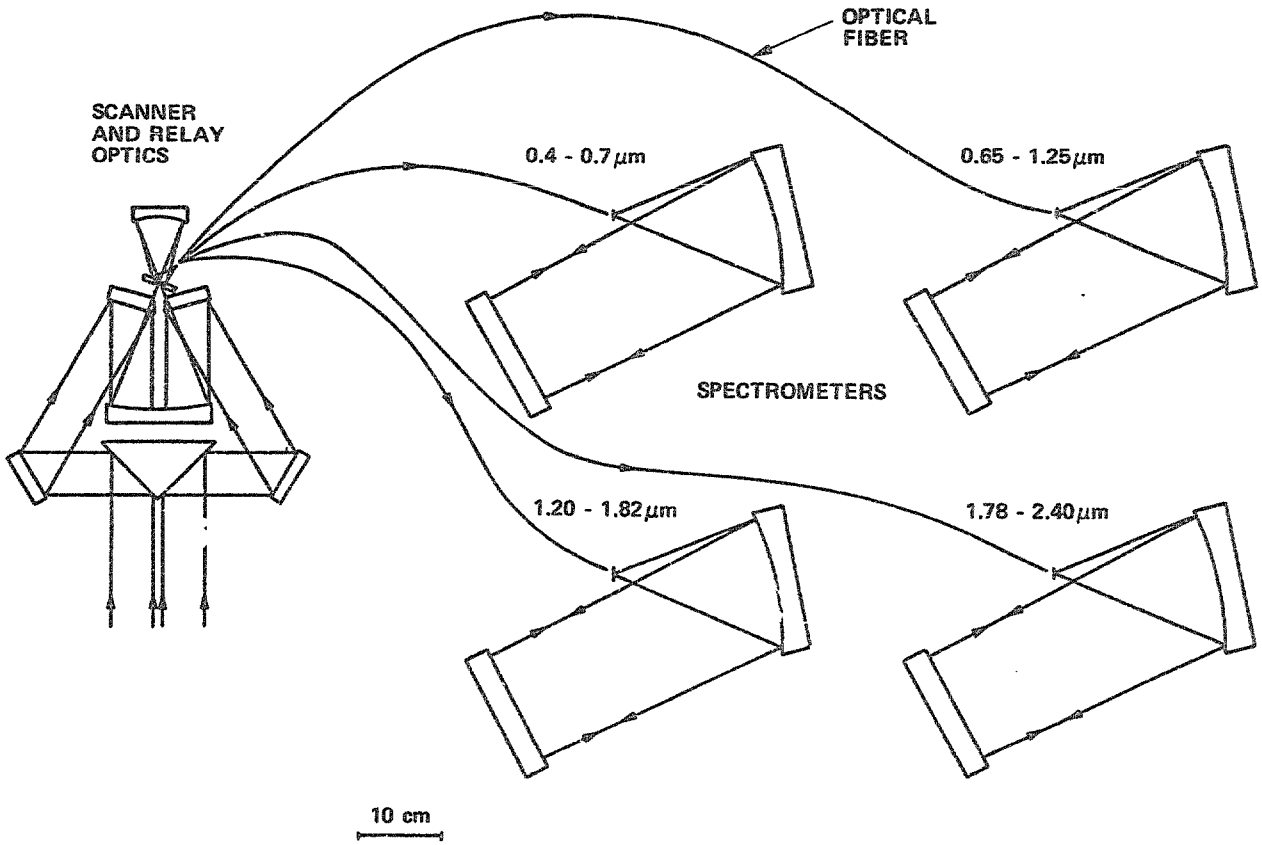

Fig. 3. AVIRIS Optics Schematic

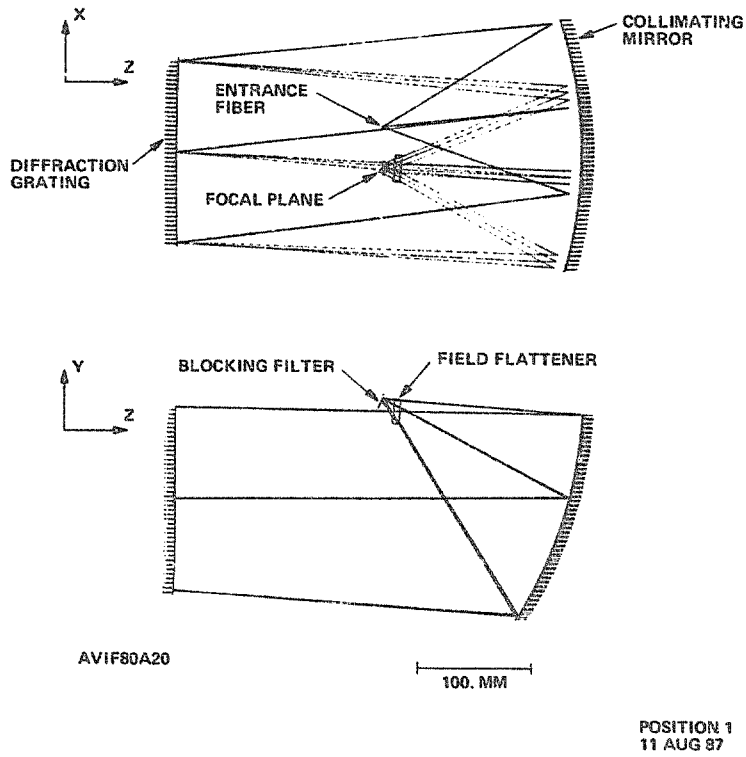

Fig. 4. AVIRIS "A" Spectrometer

In the table, α is the angle of incidence and ß is the angle of diffraction at the blaze wavelength. The blazed diffraction gratings were ruled on single-point diamond-turned aluminum substrates. The only refractive components in the spectrometers are the fused silica field flatteners and the blocking filters. The blocking filter specifications are summarized in Table 3, showing the required filter profiles.

Table 2. AVIRIS Spectrometer Optical Parameters

SPECTROMETER DESIGNATION	λ [nm]	COLLIM. R_2 [mm]	GRATING R_4 [mm]	ASPHERIC COEFFICIENTS A	B	C	D	CONIC CONSTANT	GROOVE SPACING [μm]	α [Deg]	β [Deg]
AVIF80A20	400 λ_B =550 750	379.50	2447.38	-3.0196E-9	-4.8493E-14	3.9799E-19	-1.7251E-23	-7.5968	8.5	7.07	3.35
AVIF80B20	650 λ_B =950 1250	374.41	3235.2	-3.3553E-9	-6.7655E-14	9.2947E-19	-2.8731E-23	-48.8671	7.80	8.83	1.84
AVIF80C20	1200 λ_B=1510 1820	370.51	3028.47	-3.3932E-9	-6.8325E-14	8.5751E-19	-2.5580E-23	-34.1756	8.05	10.70	0.16
AVIF75D20	1780 λ_B=2090 2400	359.75	2872.74	-3.4448E-9	-8.8769E-14	1.448E-18	-3.2394E-23	-52.0452	7.775	14.08	3.98

Table 3. AVIRIS Blocking Filter Specifications

FILTER NO.	SUGGESTED SUBSTRATE	SHORTWAVE STOPBAND λ_0	SHORTWAVE STOPBAND MAX. TRANS	PASSBAND λ_1	PASSBAND λ_2	LONGWAVE STOPBAND λ_3	LONGWAVE STOPBAND MAX TRANS
FILTER 1	SUPRASIL W1	0.35	1E-4	0.4	0.7	----	----
FILTER 2	SUPRASIL W1	0.625	1E-4	0.65	1.25	1.30	1E-4
FILTER 3	SUPRASIL W1	0.91	1E-4	1.20	1.82	2.50	1E-4
FILTER 4	SUPRASIL W1	1.20	1E-4	1.78	2.40	2.50	1E-4

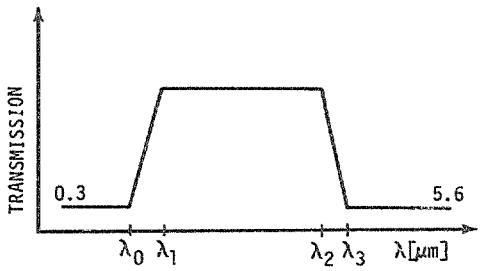

1. Operating Temp : T = 77°K
2. Adhesion of coatings per MIL-M-1308
3. Humidity per MIL-C-675A
4. Abrasion per MIL-C-675A
5. No pinholes within the clear aperture
6. In band transmittance shall be greater than 0.8 for all filters.
7. Transmission curves shall be supplied for all filters.
8. JPL Cog Engineer shall witness acceptance test.

The overall optical system transmittance is given in Tables 4 and 5. Most of the mirrors in the system for visible wavelengths have protected silver coatings. The relative diffraction efficiency measurements were made on plane sample gratings ruled with the same characteristics as the aspheric gratings.

The optical system theoretical performance has been analyzed in terms of spot diagrams (Fig. 5), with radial energy distributions shown in Figs. 6 and 7. Geometrical modulation transfer functions (MTF) and through focus MTF curves at the Nyquist frequency are given in Figs. 8, 9, 10, and 11. The system performance, including the detector MTFs, is given in Fig. 12, which shows that the MTF is greater than the 0.5 design goal at the 2.0 c/mm spatial frequency. Defining the effective spectral resolution for a sinusoidal distribution of radiance as the spectral half wavelength for which the modulation of the distribution of radiance has been reduced by one-half due to the MTF of the system, from Fig. 12, the resulting effective spectral resolution is approximately 10 nm.

Table 4. Transmittance of AVIRIS Optical System - Spectrometers A and B

		SPECTROMETER A				SPECTROMETER B			
		0.4	0.5	0.6	0.7	0.7	0.9	1.1	1.25
1	Hatch window (silica)	0.91	0.94	0.96	0.96	0.96	0.94	0.92	0.92
2	2 Reflections Al (SiO coated)	$(0.86)^2$	$(0.88)^2$	$(0.88)^2$	$(0.87)^2$	$(0.87)^2$	$(0.90)^2$	$(0.95)^2$	$(0.96)^2$
3	7 Reflections Ag	$(0.82)^7$	$(0.98)^7$	$(0.98)^7$	$(0.98)^7$	$(0.98)^7$	$(0.98)^7$	$(0.98)^7$	$(0.98)^7$
4	Fiber Reflection Loss	0.88	0.88	0.88	0.88	0.88	0.88	0.88	0.88
5	NSG Fiber Transmittance	0.81	0.94	0.98	0.98	0.90	0.96	0.98	0.98
6	Relative Diffraction Efficiency	0.43	0.60	0.62	0.59	0.61	0.76	0.58	0.47
7	Window/Field Lens (silica)	0.91	0.91	0.91	0.91	0.91	0.91	0.91	0.91
8	Bandpass Filter	0.84	0.90	0.91	0.91	0.72	0.59	0.69	0.75
9	KDP Blocking Filter	N/A	N/A	N/A	N/A	0.93	0.93	0.93	0.93
	Total Transmittance	0.04	0.26	0.29	0.27	0.19	0.21	0.21	0.19

Note: The vignetting due to the light lost off the detector arrays (~30%) has not been included above.

Table 5. Transmittance of AVIRIS Optical System - Spectrometers C and D

		SPECTROMETER C				SPECTROMETER D				
		1.25	1.4	1.6	1.85	1.85	2.0	2.2	2.4	2.45
1	Hatch window (silica)	0.92	0.92	0.91	0.91	0.91	0.90	0.90	0.89	0.88
2	4 Reflections Al (SiO coated)	$(0.96)^4$	$(0.96)^4$	$(0.97)^4$	$(0.97)^4$	$(0.97)^4$	$(0.97)^4$	$(0.97)^4$	$(0.97)^4$	$(0.97)^4$
3	5 Reflections Ag	$(0.98)^5$	$(0.98)^5$	$(0.98)^5$	$(0.98)^5$	$(0.98)^5$	$(0.98)^5$	$(0.98)^5$	$(0.98)^5$	$(0.98)^5$
4	Fiber Reflection Loss	0.89	0.89	0.89	0.89	0.89	0.89	0.89	0.89	0.89
5	Verre Fluore Fiber Transmittance	0.94	0.92	0.92	0.94	0.94	0.95	0.95	0.96	0.96
6	Relative Diffraction Efficiency	0.65	0.67	0.65	0.55	0.63	0.67	0.66	0.64	0.63
7	Window/Field Lens (silica)	0.91	0.91	0.91	0.91	0.91	0.91	0.91	0.91	0.91
8	Bandpass Filter	0.64	0.75	0.68	0.72	0.73	0.78	0.63	0.57	0.04
	Total Transmittance	0.22	0.26	0.24	0.22	0.26	0.29	0.23	0.20	0.01

Note: The vignetting due to the light lost off the detector arrays (~30%) has not been included above.

3. SPECTROMETER IMPLEMENTATION AND ALIGNMENT

The implementation of the spectrometer designs was challenging due to their high numerical aperture (N.A. = 0.45). To facilitate the alignment of the spectrometers the degrees of freedom were carefully chosen as shown in Fig. 13, enabling the line spectra to be focused and aligned on the arrays. To provide optimum light coupling from the optical fibers into the spectrometers, the fibers are mounted in the sphere arrangement shown in

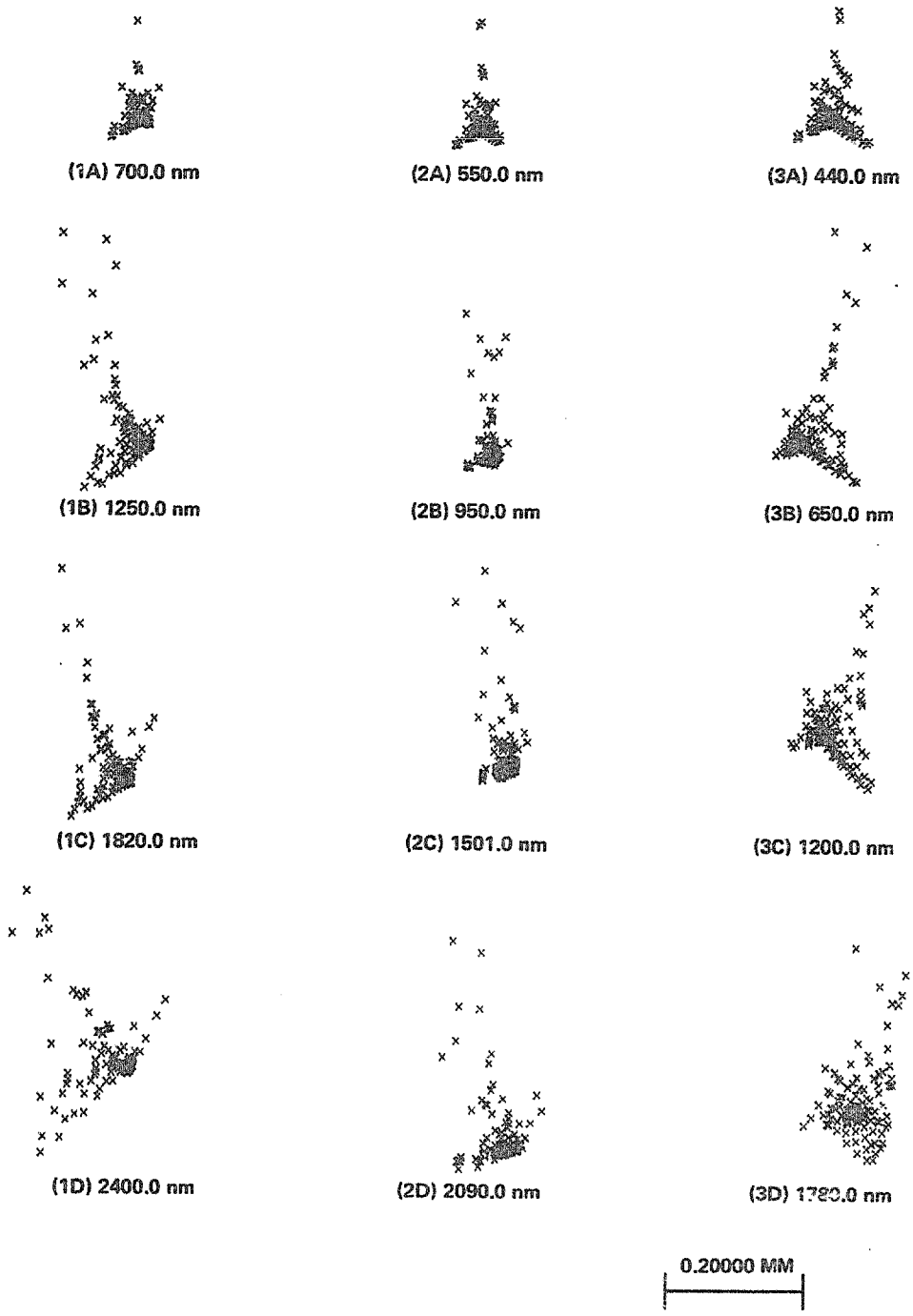

Fig. 5. AVIRIS Spectrometer Spot Diagram

Fig. 14. Rotation of the sphere allows the light from the central fiber (from the fore-optics) to be directed onto the collimating mirror without transverse displacement of the fiber. The grating mount design is shown in Fig. 15. This kinematic mount design allows the grating angle to be changed in two orthogonal directions to position the spectrum on the linear array. The grating is mounted kinematically in a cell to ensure minimal distortion. Spherical washer sets are used to ensure that no torquing forces are experienced by the cell as the shims are varied to change its angle. The mirror mount design is shown in Fig. 16, and again kinematic mount principles were followed to minimize the mirror distortion and provide ease of angular adjustment. The alignment of the spectrometers was accomplished by using higher diffracted orders of a HeNe laser at λ = 632.8 nm. First the higher orders were simulated by computer raytrace, which generated information about the position and image quality (point spread functions) in the spectrometer focal plane. This computer generated raytrace served as a baseline for evaluation of image quality and location in the focal plane during the actual alignment. The only remaining alignment was required for the detector assembly, which included the filters and the field flatteners. Focusing was accomplished by axial displacement of the optical fiber mount shown in Fig. 14.

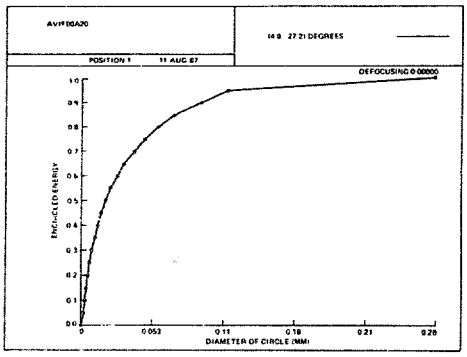

(1A) 700.0 nm

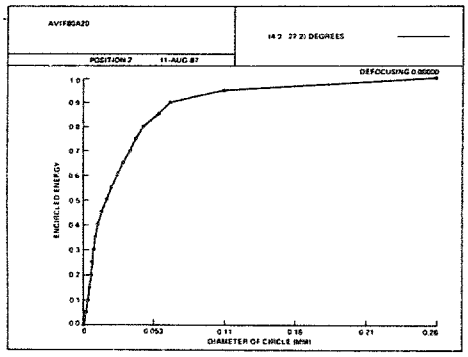

(2A) 550.0 nm

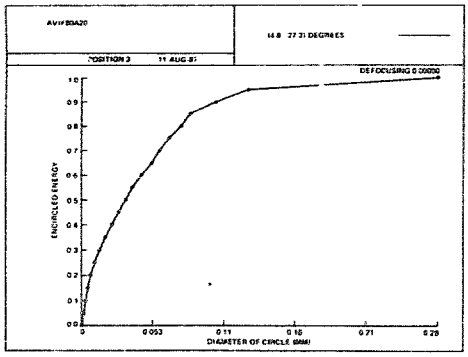

(3A) 440.0 nm

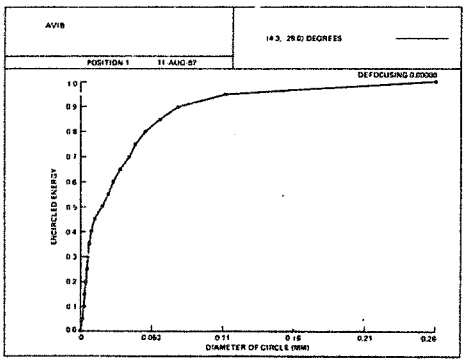

(1B) 1250.0 nm

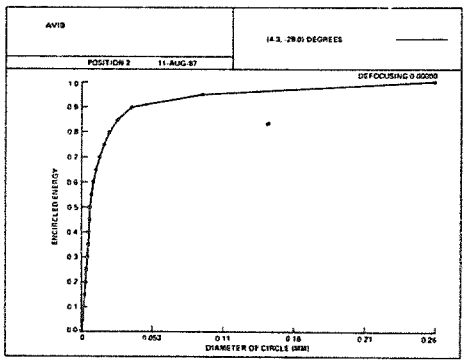

(2B) 950.0 nm

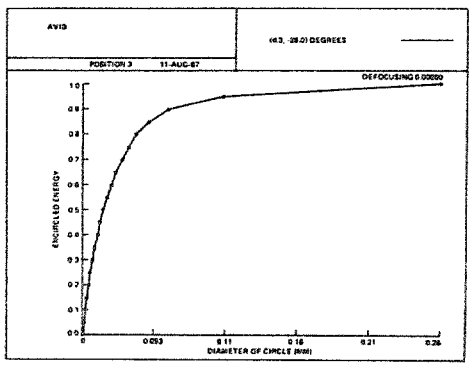

(3B) 650.0 nm

Fig. 6. Radial Energy Distribution

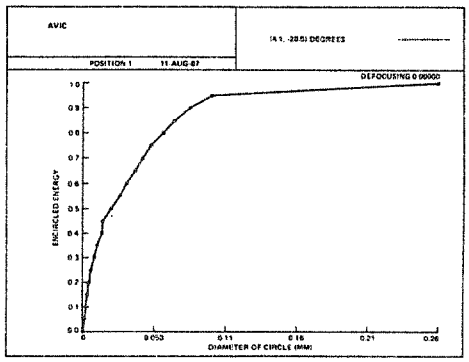

(1C) 1820.0 nm

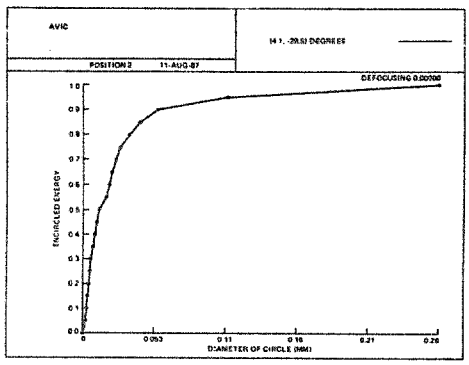

(2C) 1510.0 nm

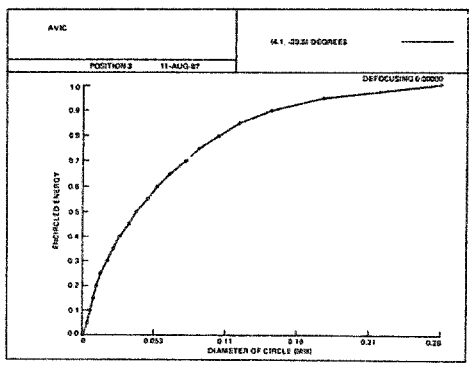

(3C) 1200.0 nm

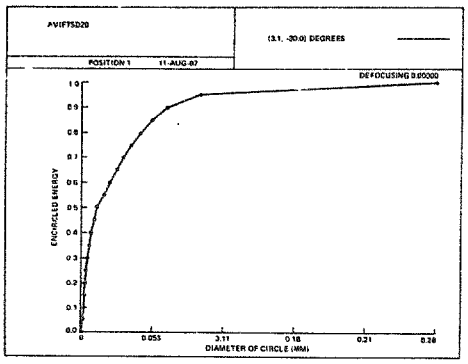

(1D) 2400.0 nm

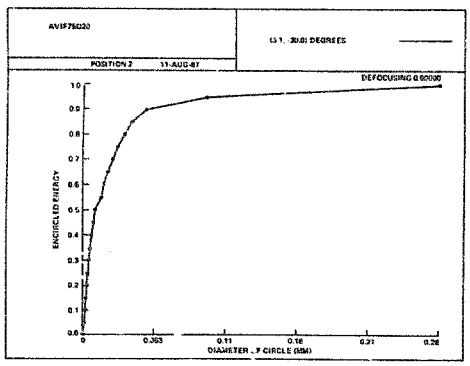

(2D) 2090.0 nm

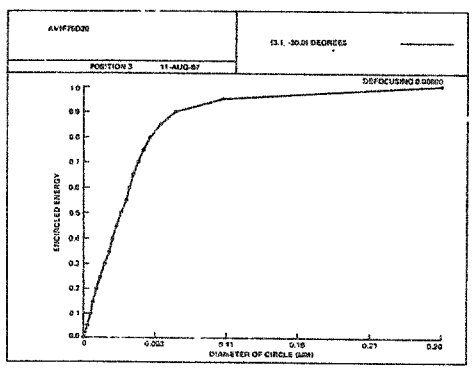

(3D) 1780.0 nm

Fig. 7. Radial Energy Distribution (Continued)

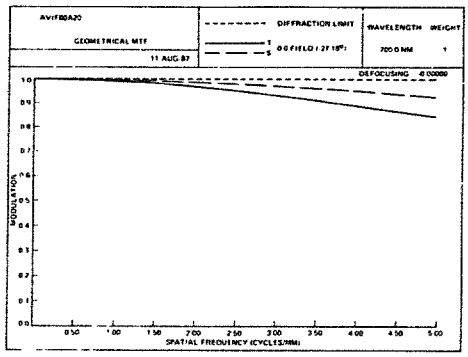

(1A) 700.0 nm

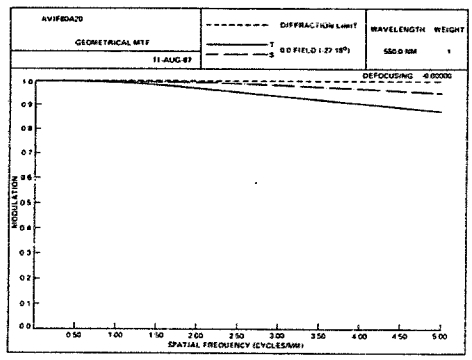

(2A) 550.0 nm

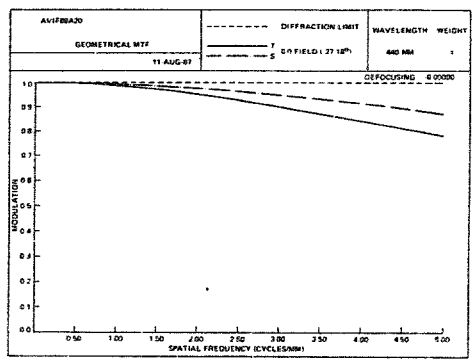

(3A) 440.0 nm

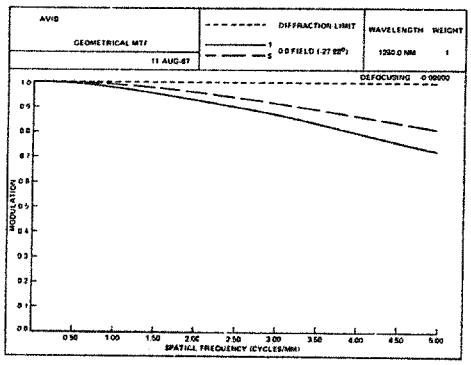

(1B) 1250.0 nm

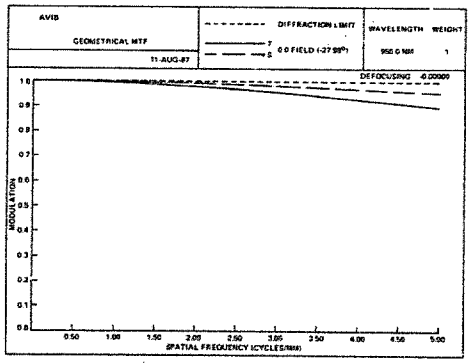

(2B) 950.0 nm

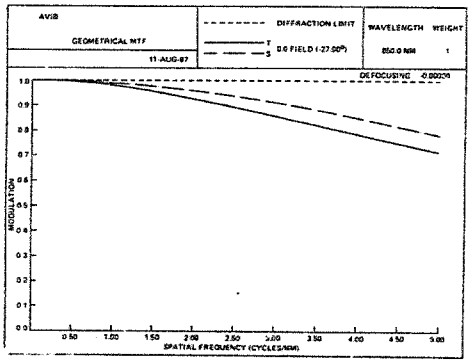

(3B) 650.0 nm

Fig. 8. AVIRIS Geometrical MTF

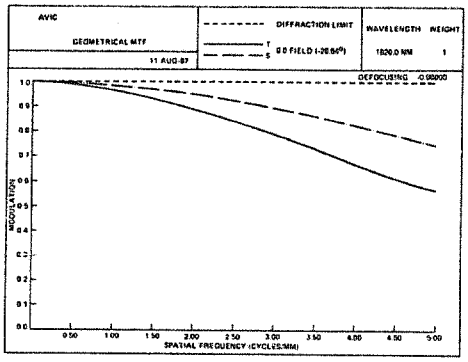

(1C) 1820.0 nm

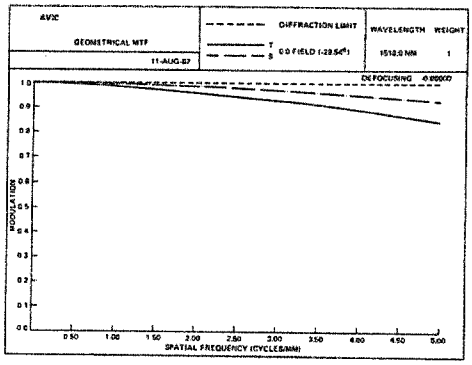

(2C) 1510.0 nm

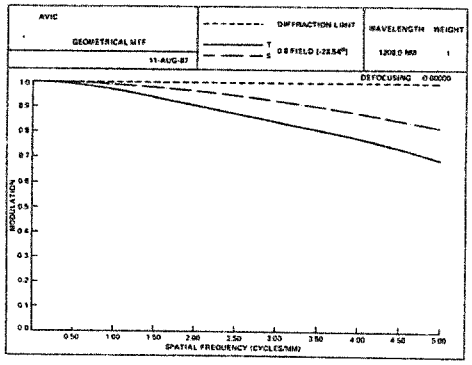

(3C) 1200.0 nm

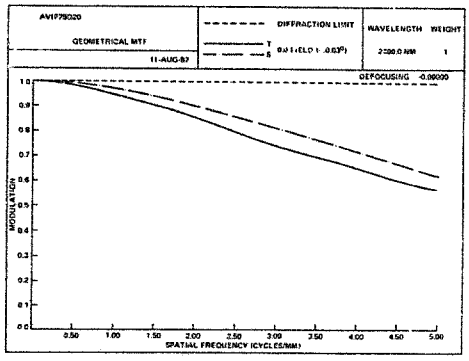

(1D) 2400.0 nm

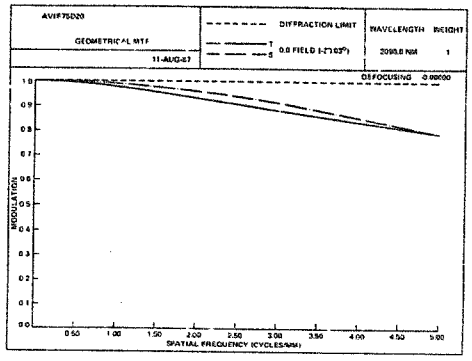

(2D) 2090.0 nm

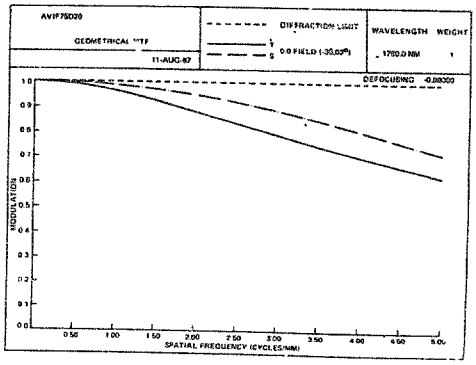

(3D) 1780.0 nm

Fig. 9. AVIRIS Geometrical MTF (Continued)

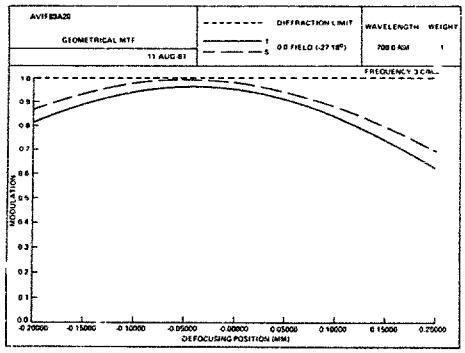

(1A) 700.0 nm

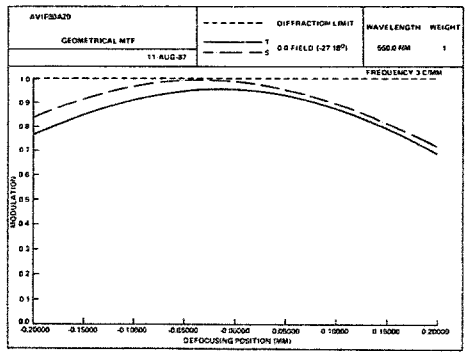

(2A) 550.0 nm

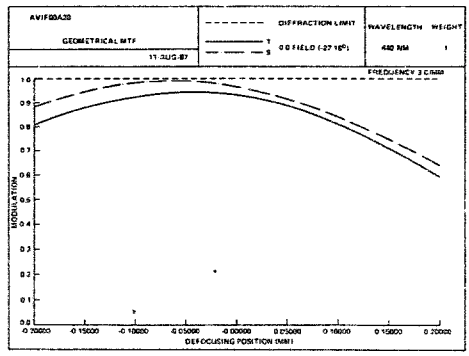

(3A) 440.0 nm

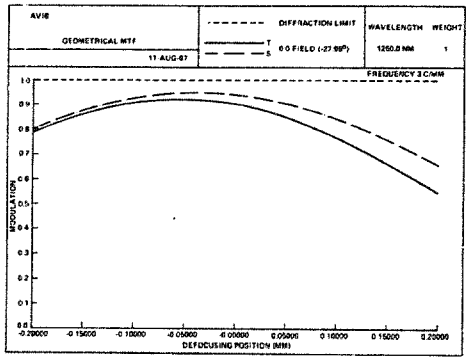

(1B) 1250.0 nm

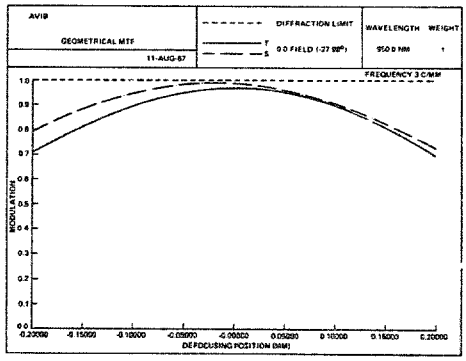

(2B) 950.0 nm

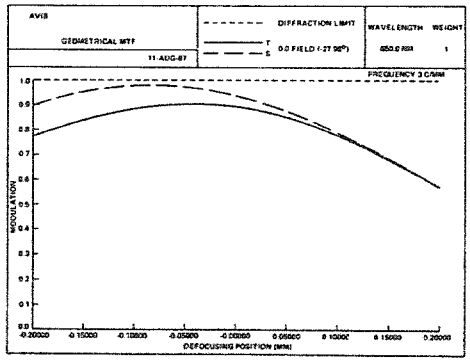

(3B) 650.0 nm

Fig. 10. AVIRIS Through Focus MTF

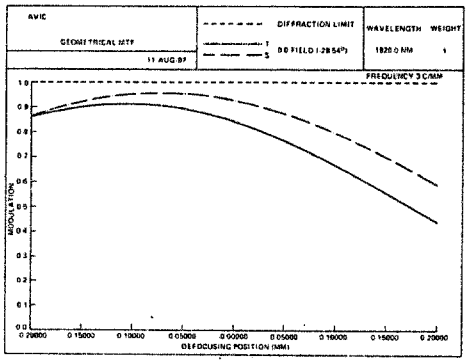

(1C) 1820.0 nm

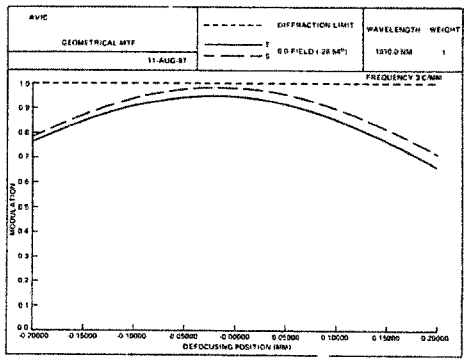

(2C) 1510.0 nm

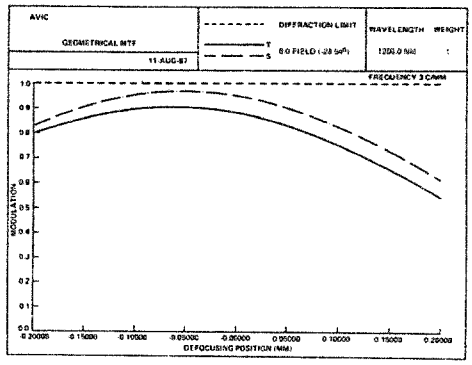

(3C) 1200.0 nm

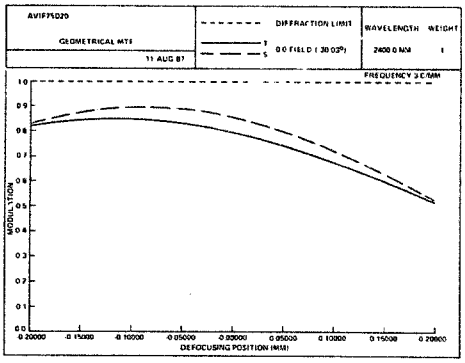

(1D) 2400.0 nm

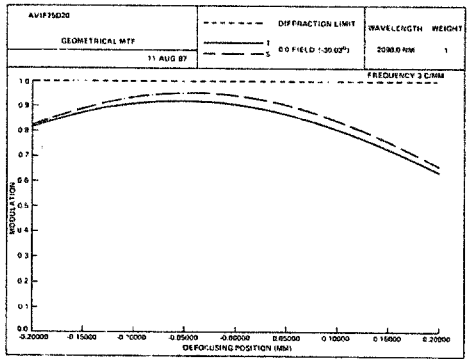

(2D) 2090.0 nm

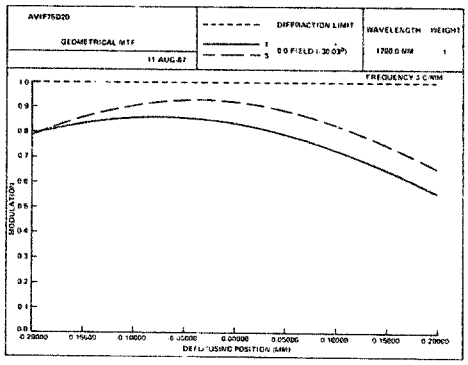

(3D) 1780.0 nm

Fig. 11. AVIRIS Through Focus MTF (Continued)

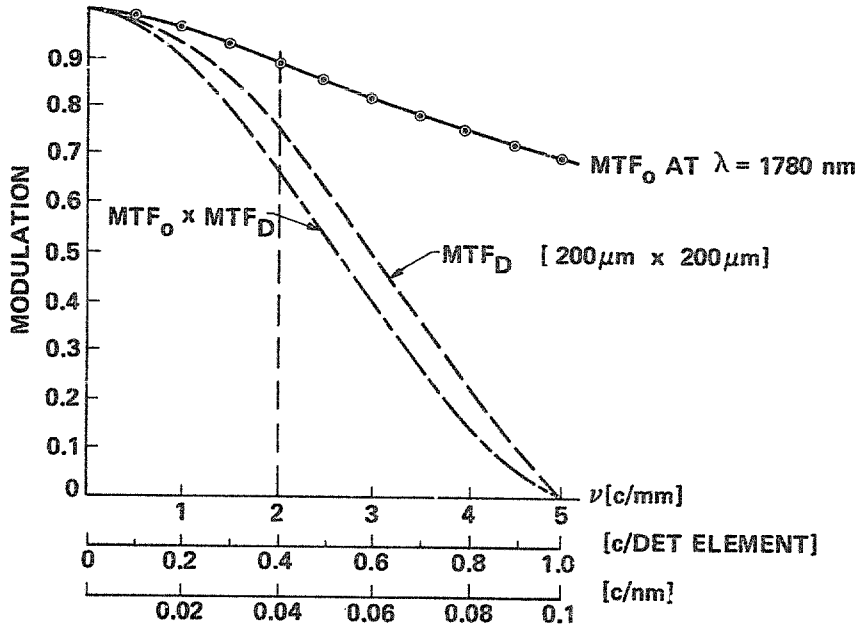

Fig. 12. AVIRIS System Modulation Transfer Function

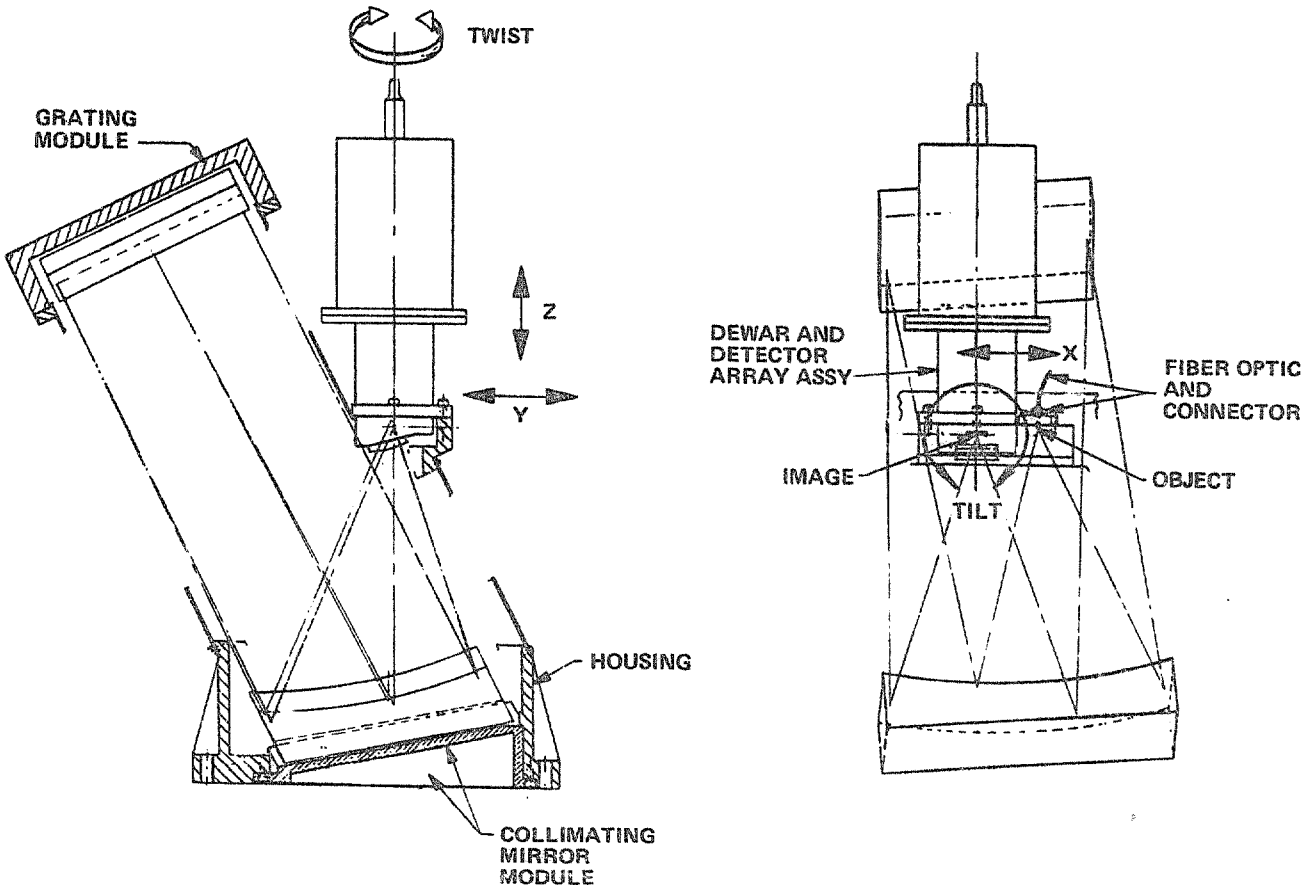

Fig. 13. AVIRIS Spectrometer Schematic

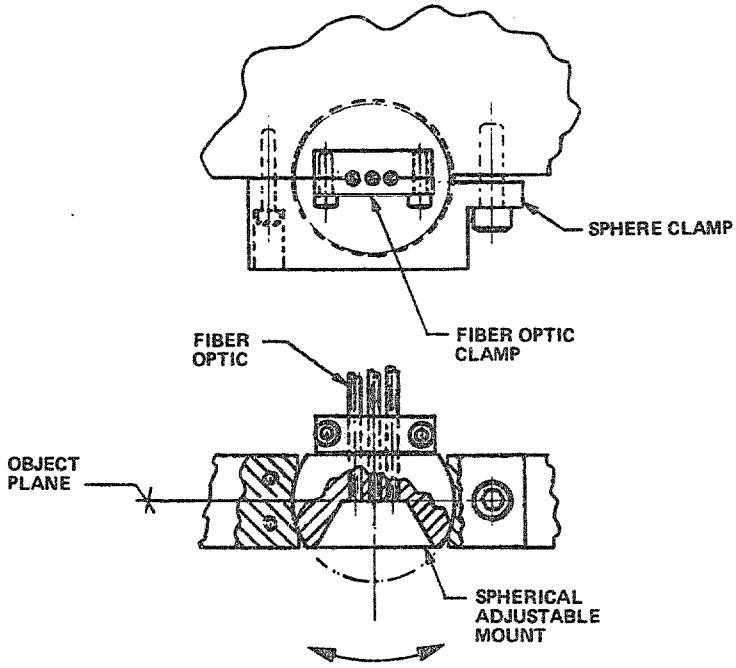

Fig. 14. AVIRIS Fiber Optics Mount

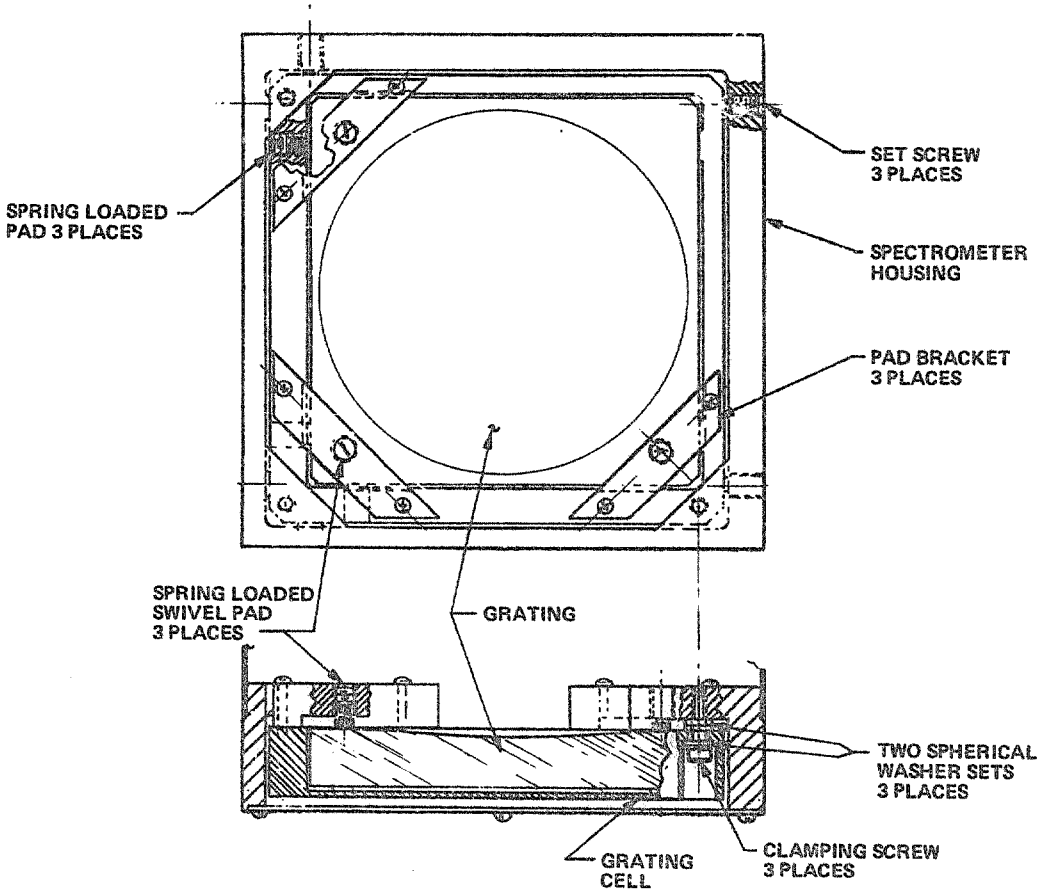

Fig. 15. AVIRIS Grating Mount

4. CONCLUSIONS

Tests of the fabricated spectrometers show that their image quality is sufficient to meet the required design goal of an MTF >0.5 at a spatial frequency of 2.0 c/mm for the spectrometer systems. Since completion of the system integration and radiometric calibration, AVIRIS has completed several test flights. The spectral images of the selected test sites, given in the accompanying papers in this session, are the best indication of the system performance under actual operating conditions.

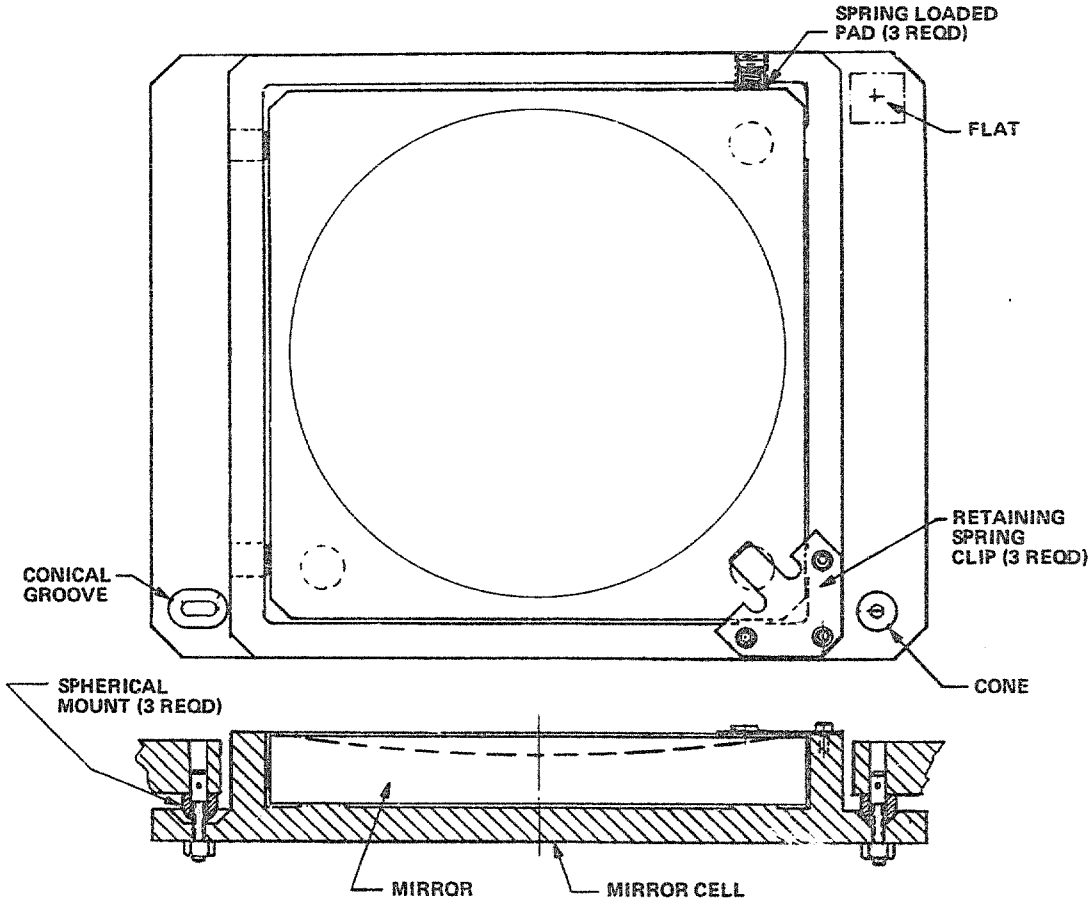

Fig. 16. AVIRIS Mirror Mount (Kinematic)

ACKNOWLEDGEMENTS

We would like to express our thanks to all members of the AVIRIS Design and Development Team for their support. The work described in this paper was supported by the Jet Propulsion Laboratory, California Institute of Technology, under a contract with the National Aeronautics and Space Administration.

REFERENCES

1. M. Herring, J. E. Duval and S. A. Macenka, "Development of the imaging spectrometer: technical challenges and solutions," SPIE 109-15.

2. M. Herring, G. C. Bailey, P. N. Kupferman, and S. A. Macenka, "Astronomical camera using a high-performance indium antimonide linear array," SPIE 501-38.

3. G. Vane, M. Chrisp, H. Enmark, S. Macenka and J. Solomon, "Airborne visible/infrared imaging spectrometer (AVIRIS): an advanced tool for earth remote sensing," Proc. 1984 IEEE Geoscience and Remote Sensing Symp., European Space Agency, SP215, Vol. 2, 1984.

4. C. LaBaw, "Airborne Imaging Spectrometer: an advanced concept instrument," SPIE 430-10.

5. M. P. Chrisp, J. B. Breckinridge, S. A. Macenka, and N. A. Page, "Imaging spectrometers for remote sensing from space," SPIE Vol. 589, 1985.

6. S. A. Macenka, "Near-infrared mapping spectrometer optical subsystem development and testing," SPIE 430-36.

7. P. N. Slater, Remote Sensing, Optics and Optical Systems, pp. 517-522, Addison-Wesley, 1980.

8. P. N. Slater, "Use of MTF in the specification and first-order design of electro-optical and photographic imaging and radiometric systems," Optica Acta, Vol. 22, No. 4, pp. 277-290 (1975).

AVIRIS foreoptics, fiber optics and on-board calibrator

M. P. Chrisp, T. Chrien and L. Steimle

Jet Propulsion Laboratory, California Institute of Technology
4800 Oak Grove Drive, Pasadena, California 91109

ABSTRACT

The foreoptics, fiber optic system and calibration source of the Airborne Visible/Infrared Imaging Spectrometer (AVIRIS) are described. The foreoptics, based on a modified Kennedy scanner, is coupled by optical fibers to the four spectrometers. The optical fibers allow convenient positioning of the spectrometers in the limited space and enable simple compensation of the scanner's thermal defocus (at the -23°C operating temperature) by active control of the fiber focal plane position. A challenging requirement for the fiber optic system was the transmission of the spectral range 1.85 to 2.45 microns at .45 numerical aperture. This was solved with custom fluoride glass fibers from Verre Fluore. The on-board calibration source is also coupled to the spectrometers by the fibers and provides two radiometric levels and a reference spectrum to check the spectrometers' alignment. Results of the performance of the assembled subsystems are presented.

1. INTRODUCTION

The Airborne Visible/Infrared Imaging Spectrometer (AVIRIS) was designed as a NASA facility instrument to fly on-board a U2 aircraft. The objective of the instrument is to provide high resolution spectral data for remote sensing. This spectral data is used to explore techniques for mineral identification, directly from exposed surface spectra and indirectly from the spectra of stressed vegetation. A complete review of the use of high resolution spectral data in remote sensing is given by G. Vane.[1,2] The instrument has been completed and numerous flights have taken place during this year (1987), the results of which are reported in this session.[3]

The instrument consists of a whiskbroom scanner connected by optical fibers to four spectrometers, shown schematically in Figure 1. As the triangular scan mirror rotates, a point on the ground is viewed in turn by each of the four spectrometers. In the spectrometers, the dispersed light is detected by cooled indium antimonide or silicon linear arrays. The calibration source is also connected by optical fibers to the spectrometers and provides information on their spectral alignment and radiometry.

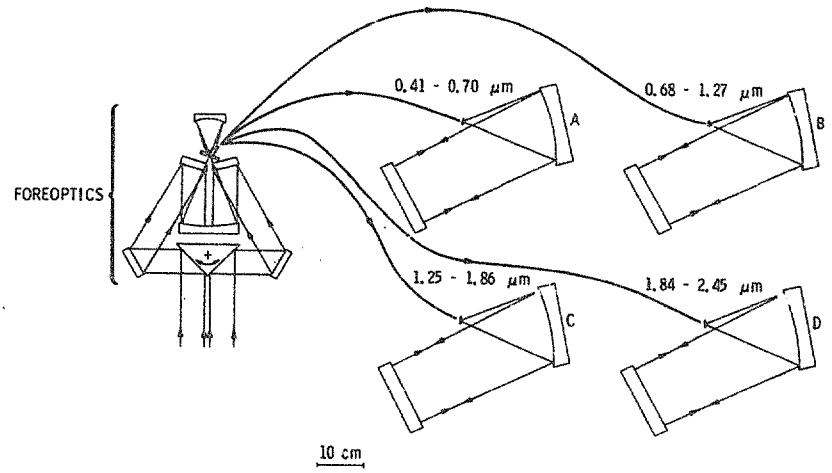

Figure 1. Optical schematic for airborne visible/infrared imaging spectrometer (AVIRIS)

This paper deals with part of the optical system, the foreoptics (scanner), fiber optics and on-board calibration source. The design, implementation, technical challenges and performance of these systems are described. The off-axis Schmidt spectrometers are described in a separate paper by Macenka and Chrisp.[4]

2. DESIGN DESCRIPTION

The main challenge in the design of the optical system was fitting the system into the limited volume available in the U2 bay, which constrained the foreoptics' and spectrometers' configuration. The initial proposed approach to do this (before the optical fibers were introduced) is shown in Figure 2. In this approach the light from the foreoptics is directed by dichroic beamsplitters into the three spectrometers. Note that the spectrometers have to be on the same optical bench structure as the foreoptics, which defines their entrance slit. Any movement between the foreoptics and the spectrometers will cause a spectral shift. This large optical bench structure is a great disadvantage because of the scanner vibration and the temperature excursion of the bay to -23°C at the operating altitude. The introduction of the optical fiber system greatly simplified the design by enabling the spectrometers to have separate optical bench structures which could be positioned independently with respect to the scanner.

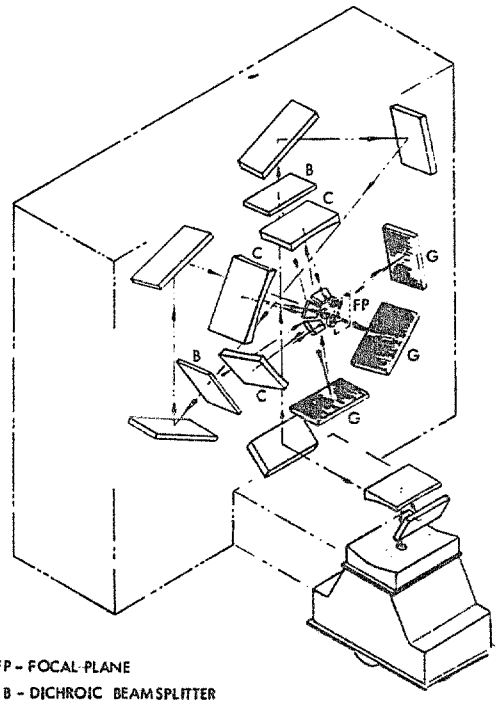

FP - FOCAL PLANE
B - DICHROIC BEAMSPLITTER

Figure 2. Initial design approach

Table 1. Optical system parameters

AΩ PRODUCE	1.3×10^{-4} cm^2 sr
EFFECTIVE PUPIL DIAMETER	14.5 cm
INSTANTANEOUS FIELD OF VIEW (IFOV)	1 mrad
FIELD OF VIEW (FOV)	30°
GROUND RESOLUTION ELEMENT	20 m
SPECTRAL SAMPLES PER GROUND RESOLUTION ELEMENT	220
SCAN RATE	12 scans/sec
SCAN EFFICIENCY	70%
EFFECTIVE FOCAL LENGTH OF FOREOPTICS	20 cm

2.1 Foreoptics

The optical parameters of the foreoptics are given in Table 1. The foreoptics completely determines the spatial performance of the optical system. The foreoptics system is based on a modified Kennedy scanner, which was converted to provide the correct IFOV and to make efficient use of the limited field of view required. The scanner was initially designed with a four sided rotating mirror to scan an FOV of approximately 160°. To efficiently use the required 30° FOV, the rotating mirror was replaced by an oscillating two sided triangular mirror, giving a scan efficiency of 70%. Scans are taken in only one direction and the flyback speed is approximately twice as great as the scan speed. The large facets on the two sided mirror also removed the vignetting in the system, resulting in an aperture increase by a factor of ~1.3.

In the initial system the detectors had originally been placed at the focus of the paraboloid mirror. To provide the correct IFOV of 1 mrad this image is magnified 1.3 times by an ellipsoidal mirror, which relays the image to the fiber optics focal plane via a fold flat with a hole in it. The fibers are placed very close together so the total image field angle required from the foreoptics is only 5 mrad. (The ellipsoid actually increases the usable image field slightly by compensating for the coma from the paraboloid.)

The reduced field of view (30°) for the system enabled the baffling of the original design to be improved. The foreoptics looks out of the aircraft through a window of fused silica, which improves the thermal environment for the instrument. The fused silica is water free, to avoid the absorption bands present in the infrared region.

2.2 Fiber optics

The use of fiber optics provides a number of advantages: The spectrometers can be positioned independently from the foreoptics, allowing efficient use of the available

aircraft volume. The spectrometers are isolated from the vibration inherently present in the scan drive. The spectrometers are also thermally isolated from the foreoptics and are in temperature controlled enclosures, greatly simplifying their design. Using the fibers to split the light into the spectrometers at a field plane avoids the use of a series of dichroic beamsplitters, which would decrease the transmittance.

The fiber optics are required to transport the light efficiently from the foreoptics to the spectrometers. A single fiber is used for each spectrometer, and the core size (200-micron diameter) forms the field stop in the foreoptics and the entrance slit for the spectrometer. The .45 numerical aperture (N.A.) of the foreoptics determines the fiber N.A. requirement, and the wavelength range for each spectrometer is given in Figure 1. The fibers had to be thinly clad (clad diameter <250 microns), so that they could be packed closely together in the foreoptics focal plane to coincide with the usable image field.

2.3 On-board calibrator

The purpose of the on-board calibrator is to check the spectral and radiometric alignment of the spectrometers during the operation of the instrument to ensure the accuracy of the spectral data. To do this the calibrator's output must be invariant over the small temperature excursions around the operating temperature (-23°C) and stable during the time period of the instrument operation.

The arrangement of the on-board calibrator is shown schematically in Figure 3. Light from a filament lamp is imaged by a concave metal mirror through a filter wheel onto the fiber optics leading to the spectrometers. The fibers are at the meridional focus so the astigmatism of the mirror blurs the filament image, reducing the sensitivity of the system to movement. The mirror and structure are monometallic so thermal effects are minimized. The rotating shutter in the foreoptics enables the light from the foreoptics to be shut off during calibration. The filter wheel in the calibrator has four positions, one of which cuts the light off. Two of the positions are used for neutral density filters to provide two radiometric levels, and the other position is used for a didymium rare earth filter to provide a reference spectrum, shown in Figure 4. This spectrum is relatively independent of the operating temperature, unlike a dichroic.

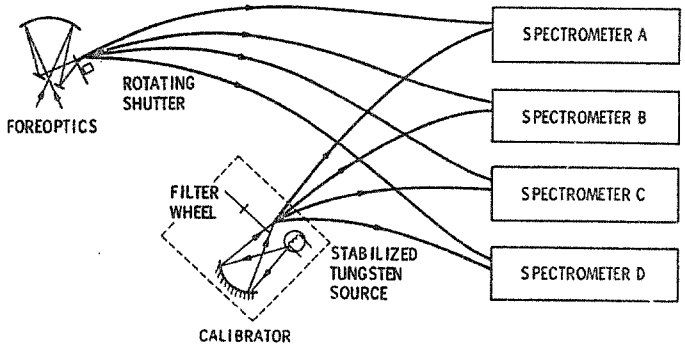

Figure 3. On-board calibrator

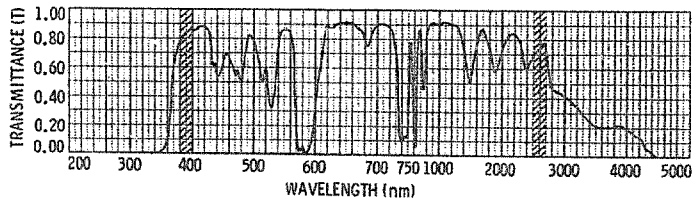

Figure 4. Didymium rare earth filter transmittance

3. DESIGN IMPLEMENTATION

3.1 Foreoptics

The basic modifications to the Kennedy scanner consisted of replacing the rotating mirror with a two sided oscillating mirror and magnifying the image by an additional ellipsoid. The two sided triangular mirror was diamond turned and hardmounted at three points to a new shaft design. Interferograms taken of the assembly show that it is repeatable within the surface flatness tolerance of 1.5 waves (~600 nm) over the 7.5 inch length. The ellipsoid mirror is aluminum and was polished by conventional metal mirror techniques. The mirrors in the foreoptics (except for the ellipsoid mirror) were coated with protected silver to avoid the aluminum absorption dip at 0.8 microns.

The depth of focus of the foreoptics is $\pm$0.04 mm (for a 5% drop in the modulation transfer function (MTF) in the track direction at 3.15 cycles/millimeter [c/mm]). Since the focus changes by .58 mm in going from room temperature to the -23°C operating temperature, active focus control is necessary. This was implemented by moving the fiber optics focal plane (Figure 5) by a stepper motor according to a temperature sensor in the foreoptics. The best focus positions were found experimentally by placing the foreoptics in a temperature controlled chamber. These were then used to generate a look-up table for the stepper motor position with temperature. The system works successfully and no problems have been encountered.

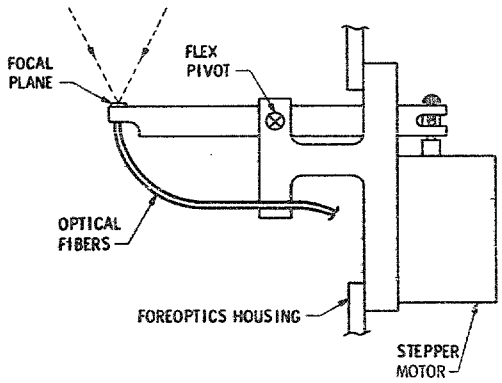

Figure 5. Active focus mechanism in foreoptics

3.2 Fiber optics

Spectrometers A and B are joined to the foreoptics by 1.9 m lengths of fiber, and C and D by 1.2 m lengths. For spectrometers A and B (0.41 to 1.27 microns) Nippon Sheet Glass (NSG) fiber SI 200H was used. This is a doped glass fiber, and measurements of its transmittance at an N.A. of .45 are shown in Figure 6.

For spectrometers C and D (1.25 to 2.45 microns), finding a suitable fiber with a transmittance/meter >0.9 (attenuation < 458 dB/km) at an N.A. of 0.45 proved to be quite challenging. The problems with silica fibers in this region are the strong absorption bands around 2.2 microns. Even low water content fibers proved to have too strong absorption bands.

The first solution proposed was to use a teflon coated fluoride glass fiber. Initial transmittance measurements of this at an N.A. of .17 showed that it had sufficient transmittance, but when these measurements were repeated at a .45 N.A., the transmittance was too low. This was identified as probably being due to scattering at the rough interface between the teflon and the glass. A different approach was therefore needed.

Most of the work on fibers in the near I.R. region has concentrated on communications problems, so the fibers developed typically have an N.A. of 0.17. Since the fiber throughput goes as the square of the N.A., much of the light would have been lost if one of these fibers had been used. The problem was discussed with the following major establishments concerned with I.R. fiber development:

Bell Labs	Naval Research Laboratory
Hughes	British Telecom
Spectran	Furakawa (Japan)
Verre Fluore	General Dynamics

Only Verre Fluore (France) thought that it would be possible to meet our requirements of N.A. and transmittance by the development of a special fluoride glass fiber, consisting of a core glass of zirconium fluoride and a cladding glass of beryllium fluoride. A contract was placed with the company, and a fiber which met our requirements was successfully developed on schedule. Its transmittance is given in Figure 6.

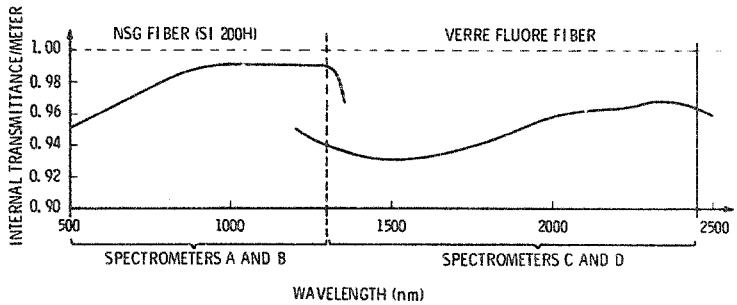

Figure 6. Fiber transmittance (measured at 0.45 N. A.)

The development of the fiber cable harness proved to be a process of iteration. The main problem was that in order to place the fibers close together in the foreoptics focal plane, their protective polymer claddings had to be stripped off. This considerably weakened the fiber and careful stress relief was necessary in going from the rigid mounting block to the flexible tubes. For the spectrometer the tight bend radius (~2 inches) and minimal space also created difficulties. No joins were allowed in the cable because

of the associated transmittance losses. After a few iterations a successful cable harness was developed, with the fibers set in an epoxy block in the foreoptics and then connected by thermoplastic tubing to capillary metal tubing which feeds them into the spectrometers. This harness is removable, facilitating changing of the fibers if one should break.

3.3 Calibration source

Measurements of the calibration source show a 0.5% change in the light output per 10°C. Tests of the instrument show that there is a 2.2% variation of the light output over a period of 30 minutes due to fluctuations in the power supply. This will be improved by the installation of a stabilized power supply, which was proposed in the initial stages but later removed because of weight constraints which have since been relaxed.

4. SPATIAL PERFORMANCE

The MTF of the foreoptics is determined by the aberrations, image smear (due to aircraft motion and scan motion) and the fiber size. The system MTF is given by

$$\text{MTF}_{\text{system}} = \text{MTF}_{\text{aberrations}} \times \text{MTF}_{\text{detector}} \times \text{MTF}_{\text{smear}}$$

The system MTF in the scan and track directions is shown in Figure 7. The MTF is lower in the scan direction due to the image smear resulting from the integration time. In the track direction there is negligible image smear due to the aircraft motion. (The details of this type of calculation are given in Appendix 1 of Ref. 5.)

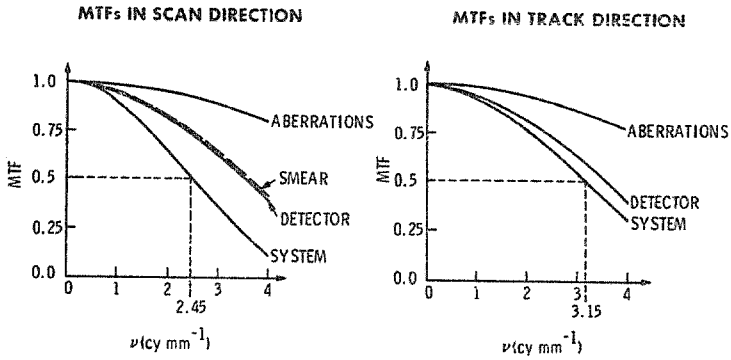

Figure 7. MTFs of AVIRIS system

The effective instantaneous field of view (EIFOV) is the spatial half wavelength for which the MTF is one half. From the graphs it can be seen that this results in:

EIFOV in scan direction = 20.5 m
EIFOV in track direction = 15.9 m

Measurements of the aberrations of the assembled foreoptics show that the spot sizes are in agreement with the aberration values used for the MTF curves.

5. STRAY LICHT AND POLARIZATION

The stray light of the foreoptics was measured by mounting the system on a rotary table in front of a highly collimated source (1 mrad divergence). Measurements were taken as the table was rotated, giving the intensity of light in the image plane with angle. The primary aim of the stray light measurements was to check for unidentified stray reflections. The results showed that the stray light intensity within 0.1 degrees of the image is from 0.3% to 2%, and beyond 2 degrees from the image is less than 0.1%. The major portion of the stray light originates with the diamond-turned scan mirror, which was not post-polished. This diamond fly-cut mirror has been shown by measurements to have a much greater surface roughness than the grating blanks in the instrument, which were diamond-turned.

The polarization was measured in the visible by rotating a linear polarizer in front of the foreoptics. This gave a variation in transmittance of the system for the linear polarization of 5.5%. One of the useful features of the fiber optics is that they scramble the polarization, so the diffraction grating polarization efficiencies do not affect the system sensitivity to polarization.

6. CONCLUSION

The foreoptics provides the required spatial resolution and the thermal focus compensation adjustment works successfully within the required tolerance.

The fiber optics system has the required transmittance and optical throughput, and a practical cable harness has been developed. The fiber optics system has greatly simplified the instrument design and has been very successful. The on-board calibrator has sufficient temperature stability and will meet the long term stability requirements with an improved power supply.

The AVIRIS instrument has been flying since the beginning of 1987 and the spatial resolution of the operating instrument has been verified in a number of flights over test sites. This data is presented in one of the accompanying papers in this session.[3]

7. ACKNOWLEDGEMENTS

Thanks are due to Eric Fuller for his excellent work on the optomechanical assembly and Roscoe Donnel for his help with the fiber transmittance measurements.

The writing and publication of this paper were supported at the Jet Propulsion Laboratory, California Institute of Technology, by the National Aeronautics and Space Administration.

8. REFERENCES

1. Vane, G., "High Spectral Resolution Remote Sensing of the Earth," Sensors 2, 11 (1985)
2. Vane, G., and Goetz, A.F.H., "Terrestrial Imaging Spectroscopy," Remote Sensing of the Environment (in press) 24 (1988)
3. Vane, G., "First Results from AVIRIS," Int. Soc. Opt. Eng. 834 (1987)
4. Macenka, S.A., and Chrisp, M.P., "AVIRIS Spectrometer Design and Performance," Int. Soc. Opt. Eng. 834 (1987)
5. Slater, P.N., "Remote Sensing," Addison-Wesley (1980)

Visible and infrared linear detector arrays for the Airborne Visible/Infrared Imaging Spectrometer (AVIRIS)

Gary C. Bailey

Jet Propulsion Laboratory, California Institute of Technology
4800 Oak Grove Drive, Pasadena, California 91109

ABSTRACT

The Airborne Visible/Infrared Imaging Spectrometer (AVIRIS) instrument uses four separate focal plane assemblies consisting of line array detectors that are multiplexed to a common J-FET preamp using a FET switch multiplexing (MUX) technique. A 32-element silicon line array covers the spectral range from 0.41 to 0.70 μm. Three additional 64-element indium antimonide (InSb) line arrays cover the spectral range from 0.68 to 2.45 μm. The spectral sampling interval per detector element is nominally 9.8 nm, giving a total of 224 spectral channels. All focal planes operate at liquid nitrogen temperature and are housed in separate dewars. Electrical performance characteristics include a read noise of < 1000 e^- in all channels, response and dark nonuniformity of 5% peak to peak, and quantum efficiency of > 60%.

1. INTRODUCTION

The Airborne Visible/Infrared Imaging Spectrometer (AVIRIS) instrument is the first flight instrument (flown in a U2 aircraft) to utilize FET switch multiplexing (MUX) techniques developed at JPL for readout of indium antimonide (InSb) detector material that covers the 0.7- to 5.2-μm spectral range. The technology described in the following sections has undergone significant developmental refinement to the point where high reliability and performance characteristics can be obtained at reasonable cost.

2. DESIGN

The AVIRIS focal plane design uses a new Reticon MUX that features lower video line capacitance along with an integral reset switch. These two improvements lower noise and simplify the hybrid design as described in previous papers.[1,2,3] The new MUX design is the result of considerable prototype hybrid experience and reflects all the improvements found to be desirable from early work.

The integral reset switch and tighter design rules reduce video line capacitance, which gives a reduction in KTC noise. A dummy pixel has been added at the beginning and end of the MUX to minimize first and last pixel offsets induced from the geometry discontinuity at the start and finish of the structure. Other improvements include mirror image MUXs of 32, 64, 128, and 256 inputs, along with wider scribe clearance adjacent to the detector input pads to improve wire-bonding yield.

The focal plane hybrid design consists of three subassemblies: 1) a detector line array with a fan-in interconnect to match the MUX input bonding pad pitch, 2) a MUX and thick-film circuit pattern, and 3) a J-FET follower preamp with thermal isolation and bias load resister. Each subassembly can therefore be tested prior to final assembly into the Kovar package. The result is a high-reliability hybrid that is 100% functional at initial test and requires no rework! This is a prime requirement for any high-reliability hybrid: It must operate properly at initial test.

Figure 1 shows a block diagram of the Reticon MUX, in which the detector materials (silicon and InSb line arrays) are connected to the input bonding pads. The detectors are operated in the charge storage mode, in which each detector is supplied with a small reverse bias (~0.25 V), which charges the junction capacitance. After the signal integration interval (86 μsec in the case for AVIRIS), each pixel is sequentially reset by the shift register, and the resulting voltage excursion is applied to the gate of the J-FET preamp for impedance conversion. Signal amplification is accomplished off the focal plane. In Figure 2, a completed focal plane is shown with its blocking filter and field-of-view mask removed for clarity. The filter cuts off all input flux beyond 2.5 μm and is cooled along with the mask to the focal plane temperature.

3. FABRICATION

Cincinnati Electronics manufactured the mesa InSb photodiodes, while United Detector Technology provided the silicon photodiodes with its standard DP-125 process. The detector line arrays are probed for proper I-V characteristics at the wafer level and bonded to the

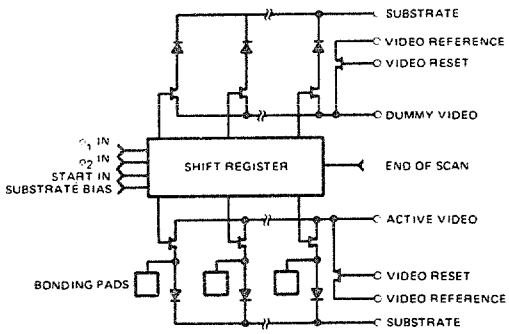

Figure 1. Simplified block diagram of the Reticon multiplexer.

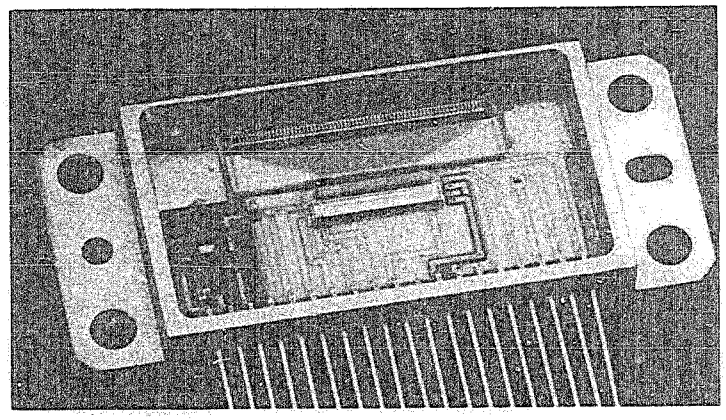

Figure 2. 64-element InSb AVIRIS focal plane.

fan-in thin-film ceramic carrier. The subassembly is then retested at liquid nitrogen (LN_2) temperature for proper detector leakage performance and set aside for final assembly into the focal plane. Spectral response measurements are performed on a sample of 5 to 10 random elements from the wafer to qualify that parameter. This test is not performed on the actual detectors that are bonded to the fan-in because of the high uniformity of this material (±2.5%); thus the risk of ESD damage to the detectors is minimized by one less handling step.

Reticon supplies the MUX die 100% probed for functionality. This allows the die to be visually inspected and directly mounted to the thick-film ceramic circuit carrier for test. Since each input node has a 10 μ x 10 μ photodiode built in, a complete functional test can be carried out at room temperature before final assembly into the hybrid. Again, the handling and testing are held to a minimum, thus improving the reliability of the final hybrid assembly.

Intersil supplies the 2N6483 J-FET 100% tested for D.C. parameters. A.C. parameters (E_n and I_n noise) cannot be accurately measured in die form; however, experience has shown that uniform D.C. parameters lead to good A.C. performance, and no J-FET has ever been removed from a hybrid because of poor noise or D.C. characteristics. The J-FET die is mounted on a hollow fiberglass post to provide thermal isolation, which causes the J-FET to operate at approximately 30K above the focal plane temperature due to the ~15 mW dissipation in the 2N6483. A ceramic cover is placed over the J-FET so the InSb detectors cannot "see" this heat source in low-background applications. This subassembly is set aside for final hybrid fabrication after a D.C. probe test.

All subassemblies are now bonded into the Kovar package and wire-bonded together along with the connection to the package pin-outs. The completed assembly is mounted in a test dewar and cooled to LN_2 temperature for a functional test. If the focal plane passes this test (all six units did the first time), it is removed from the test fixture and installed in the flight dewar. The blocking filter and mask are installed, and final acceptance tests are performed.

4. PERFORMANCE

The AVIRIS flight focal plane assemblies exceeded all performance specifications. The read noise specification of 1,200 e^- was the main beneficiary of the improved MUX design, in which reduced capacitance resulted in lower noise. The flight units had a noise variation from 890 e^- to 980 e^-. Response nonuniformity and dark current nonuniformity were within specification at 5% peak to peak. Typical spectral response curves for InSb and the silicon detectors are shown in Figures 3 and 4, respectively. As a point of interest, the 2.5-μm blocking filters were found to have small area (on the order of a few pixel dimensions) transmission variations as large as the detector response variation.

Table 1 gives a summary of the flight focal plane performance variation with regard to important electrical parameters.

Table 2 gives the important electrical and mechanical characteristics of the AVIRIS focal plane assemblies.

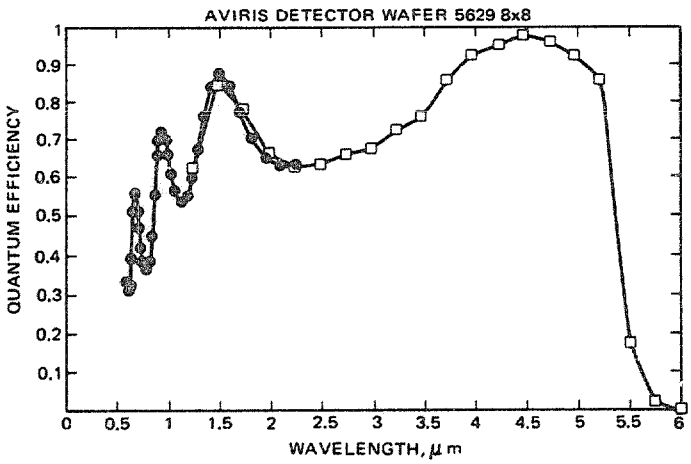

Figure 3. Typical InSb spectral response.

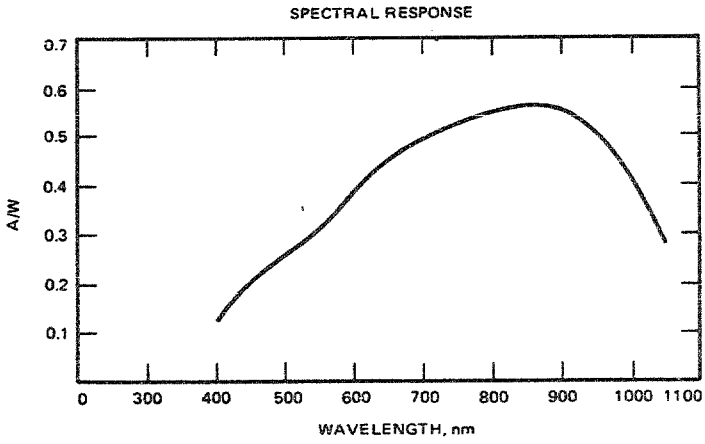

Figure 4. Typical silicon spectral response.

Table 1. Flight Focal-Plane Performance

Flight S/N	Follower Gain	Capactive Division	Read Noise	Response Nonuniformity (Standard Deviation)	Output Transfer Function	Detector Material
1	0.915	0.572	918 e^-	0.7%	8.73×10^4 e^-/mV	InSb
2	0.900	0.526	948 e^-	0.7%	9.48×10^4 e^-/mV	InSb
3	0.909	0.587	887 e^-	0.56%	8.52×10^4 e^-/mV	InSb
4	0.920	0.467	722 e^-	<0.7%	4.89×10^4 e^-/mV	Si
5	0.910	0.468	750 e^-	<0.7%	4.84×10^4 e^-/mV	Si
6	0.878	0.579	972 e^-	0.85%	8.64×10^4 e^-/mV	InSb

Table 2. AVIRIS Focal-Plane Electrical and Mechanical Characteristics

Package Size	1.48 in. x 0.66 in. x 0.225 in.
Material	Kovar
Electrical Connections	13
Pixel Size	200 x 200 μm
Pixel Pitch	230 μm
Clocks	3 (12-V swing)
Detector Material	32-Element Silicon 64-Element InSb
Response Nonuniformity	5% Peak to Peak
Dark Current Nonuniformity	5% Peak to Peak
Quantum Efficiency	>60% (see curve)
Operating Temperature	80K
Power Dissipation	15 mW

Figure 5 shows the typical high image quality obtained from the AVIRIS system. These frames are from the second engineering flight and are representative of both the silicon and InSb signal channel performance.

SAN FRANCISCO
BAY AREA

BAND 30 (0.686 μm)

BAND 125 (1.516 μm)

BAND 68 (1.017 μm)

BAND 188 (2.097 μm)

Figure 5. Typical AVIRIS flight imagery, Rogers Dry Lake.

5. CONCLUSIONS

The AVIRIS instrument is the first operational system to provide a large, 614-pixel spatial cross-track format combined with 224 10-nm-wide spectral channels over the 0.4- to 2.45-μm region. A typical flight path will extend to several thousand pixels. The sheer quantity of data created can tax the largest image processing facilities available.

Without multiplexed line array focal planes, an instrument such as AVIRIS is not practical to construct. The high-quality image produced is testimony to how good the detector technology works. From a performance/cost point of view, this detector technology development can only be pronounced a success.

6. ACKNOWLEDGMENTS

The authors wish to express thanks to the many people who contributed to this successful technology development and for the continuing sponsor enthusiasm at NASA Headquarters.

The research described in this paper was performed at the Jet Propulsion Laboratory, California Institute of Technology, and Cincinnati Electronics, under contract with the National Aeronautics and Space Administration. The funding for this research was provided by the Office of Space Science and Application.

7. REFERENCES

1. G.C. Bailey, "An Integrating 128 Element Linear Imager for the 1 to 5 μm Region," Proc. SPIE, Vol. 311, proceedings of the SPIE meeting held in San Diego, California, Aug. 27-28, 1981, pp. 32-37, 1982.

2. G.C. Bailey, "An Integrating 128 Element InSb Array: Recent Results," Proc. SPIE, Vol. 345, proceedings of the SPIE meeting held in Arlington, Virginia, May 6-7, 1982, pp. 185-191, 1982.

3. G.C. Bailey, K. Matthews, and C.A. Niblack, "Operating of Integrating Indium Antimonide Linear Arrays at 65 K and Below," Proc. SPIE, vol. 430, proceedings of the SPIE meeting held in San Diego, California, Aug. 23-25, 1983.

AVIRIS scan drive design and performance

D.C. Miller

Jet Propulsion Laboratory, California Institute of Technology
4800 Oak Grove Drive, Pasadena, California 91109

ABSTRACT

The Airborne Visible/Infrared Imaging Spectrometer (AVIRIS) images the ground with an instantaneous field of view (IFOV) of 1 mrad. The IFOV is scanned 30 deg from left to right to provide the cross-track dimension of the image, while the aircraft's motion provides the along-track dimension. The scanning frequency is 12 Hz, with a scan efficiency of 70%. The scan mirror has an effective diameter of 5.7 in., and its positional accuracy is a small fraction of a milliradian of the nominal position-time profile.

This paper describes the design and performance of the scan drive mechanism. Trade-offs among various approaches are discussed, and the reasons given for the selection of the cam drive. The salient features of the design are presented. The method of measuring performance is described, and the performance results are given.

1. INTRODUCTION

The Airborne Visible/Infrared Imaging Spectrometer (AVIRIS) is an instrument which flies on NASA's U-2 and ER-2 aircraft and records the spectrum of sunlight reflected from the ground in the 0.4- to 2.5-μm region. This information has many potential uses, such as the identification of surface materials.

AVIRIS employs a mechanical scanner to view the ground. The overall instrument configuration is shown in Figure 1. The scanner provides a field of view (FOV) of 30

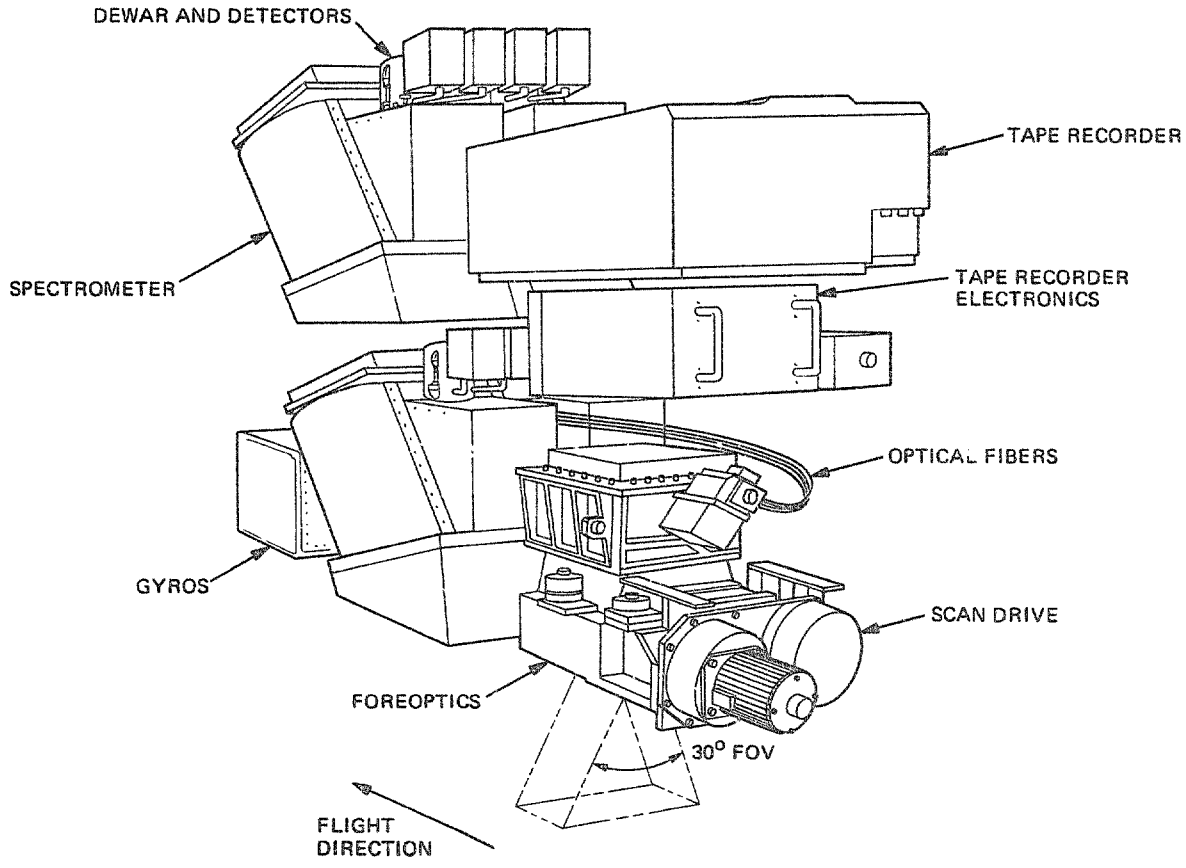

Figure 1. AVIRIS configuration.

deg. To achieve this, it must move only 15 deg, as the scan motion is effectively doubled by the mirror. A few degrees of overscan are provided to enable a compensation for roll motion of the aircraft. In Figure 2, a partial cross-section of the foreoptics, the scan mirror rotates ± 8.4 deg to move the instantaneous field of view (IFOV) ± 16.8 deg. This provides an instrument FOV of 33.6 deg. The scan profile, i.e., the motion of the scan mirror, is specified in Figure 3. It is the task of the scan drive to provide this motion.

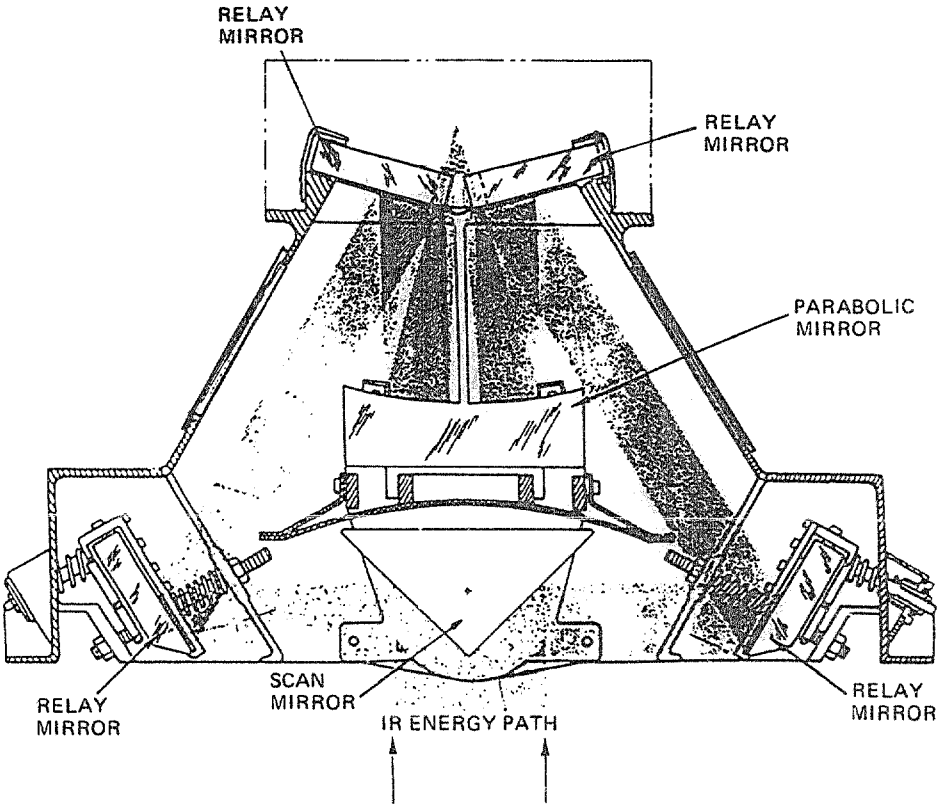

Figure 2. Foreoptics cross section.

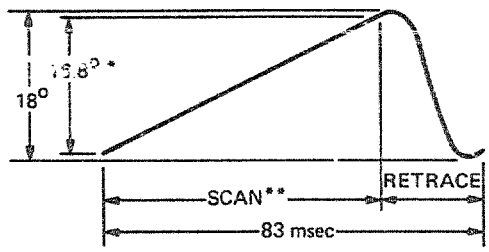

* SCAN LINEARITY: 0.1 pixel
** SCAN EFFICIENCY: 70% min

Figure 3. Scan profile.

The scan drive must also meet the following requirements: It must be "smooth," that is, it must not produce vibrations that excite resonances in the foreoptics or otherwise degrade its optical performance. It must have a lifetime of at least 300 hours of operation. It must be isolated from or be able to tolerate the aircraft environment, predominantly a 100-Hz vibration of 0.001-in. amplitude. Lastly, the scan drive has to be compatible with the aircraft and with the foreoptics.

2. IMPLEMENTATIONS CONSIDERED

Several implementations of the scan drive were considered. The straightforward approach was to rotate a prism-shaped mirror whose cross-section is a regular polygon. Another approach was to attach a torque motor to the mirror shaft and direct-drive the mirror to produce the desired scan profile. A third implementation that was considered was to bump the mirror to reverse its direction and let it coast between impacts. The last approach considered was to drive a cam at a constant speed, with the scan mirror attached to the cam follower.

The rotating, multi-faceted mirror approach was discarded early. The combination of the small FOV and required 70% scan efficiency would have resulted in a mirror 42 in. in diameter. Such a mirror would have been a significant task in itself and could not be accommodated in the U-2 aircraft because of its size.

The use of a direct-drive torque motor was investigated at length. The early estimated torque requirements for the drive called for the motor to deliver 320 lb-in. of torque to the mirror and to accelerate the mirror (and motor rotor) at 14,000 rad/sec^2.*

*It would be interesting to reassess this approach in the light of the final drive requirements, which are 55 lb-in. of torque and 4,200 rad/sec^2 acceleration. The scan rate, scan mirror travel, and scan mirror size were all reduced as the design proceeded, resulting in the relaxed performance requirements.

Commercially available motors fell short of this performance. In addition, the motor power supply requirements were formidable. The development of such a motor and power supply were judged to be undesirable, and this approach was abandoned.

The next implementation considered was a "bump and coast" scan mirror like that used in the LANDSAT Thematic Mapper described in Reference 1. That design is a remarkable achievement that will surely find many applications. However, it is not suitable for this application because the scan time is necessarily equal to the retrace time. This would limit scan efficiency to less than 50%, which is too low for AVIRIS. The Thematic Mapper gathers data during both directions of scan mirror motion, and this bidirectional scanning results in a scan efficiency of over 90%. This approach was not considered for AVIRIS as it would have put a heavy burden on the computer facility used to process AVIRIS data.

The cam approach was adopted after eliminating these other implementations. It was always clear that a cam drive could generate the desired scan profile. However, this approach carried with it concerns about accuracy, vibrations, wear, and contamination from lubricants. For these reasons, it was initially considered to be the least attractive of the four approaches. However, as discussed below, the implementation of the cam approach to AVIRIS has been successful.

3. EVOLUTION OF SCAN DRIVE DESIGN

The basic concept is shown in Figure 4. If the cam is the proper shape, and if the follower is held in contact with the cam, the mirror will have the proper motion. The implementation of this simple concept is shown in Figures 5 and 6, and is obviously not so simple. One set of complications is the usual provisions for practical details: attachment points, bearing journals and housings, couplings, assembly/disassembly features, access ports, etc. However, there is another set of complications, which arises from the scan drive requirements. These are described below.

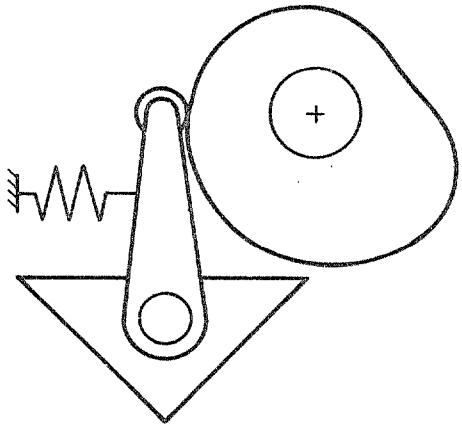

Figure 4. Basic cam concept.

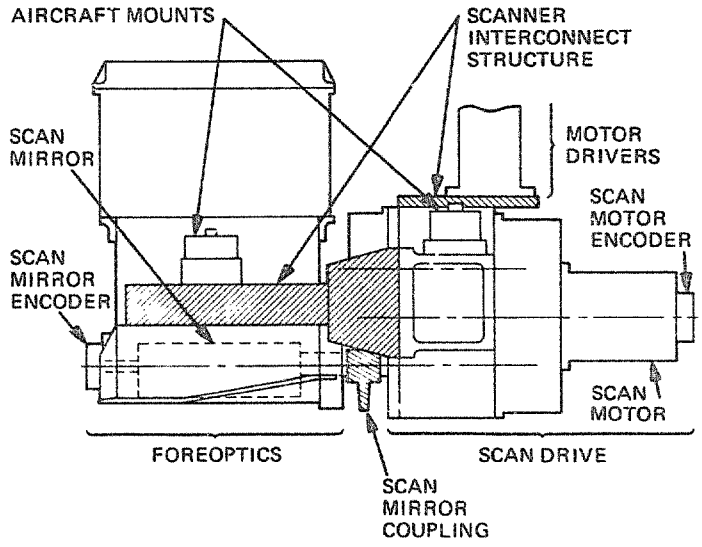

Figure 5. AVIRIS scanner.

The spring that holds the follower arm against the cam must be quite strong because of the high accelerations during retrace. This spring has to be compressed once each scan, and a considerable torque on the camshaft is required to do this. It turns out that this torque is the driver in sizing the motor. This is not a problem during operation, since the torque can easily be supplied by the momentum of a flywheel on the camshaft. Rather, it is during start-up that the motor must supply the torque. But start-up is a firm requirement and so the spring had to be eliminated to avoid the high torque requirement for the motor. The solution is the conjugate cam, which is the first addition to the simple basic concept. Conjugate cams provide the same follower motion, one from the "clockwise" side of the follower and the other from the "counterclockwise" side. This is shown in Figure 7. One cam provides the force to rotate the follower in one direction and its conjugate provides the force to rotate it in the other direction. This is the same idea as the "Desmodromic Drive" used to operate the valves of an internal combustion engine. Now the motor torque requirement is reduced to overcoming bearing drag and windage losses, plus a little for accelerating the whole machine up to speed in a reasonable time (a few seconds). Except for the bearing and windage losses, which are small, the system conserves mechanical energy. This makes analysis of the machine relatively easy.

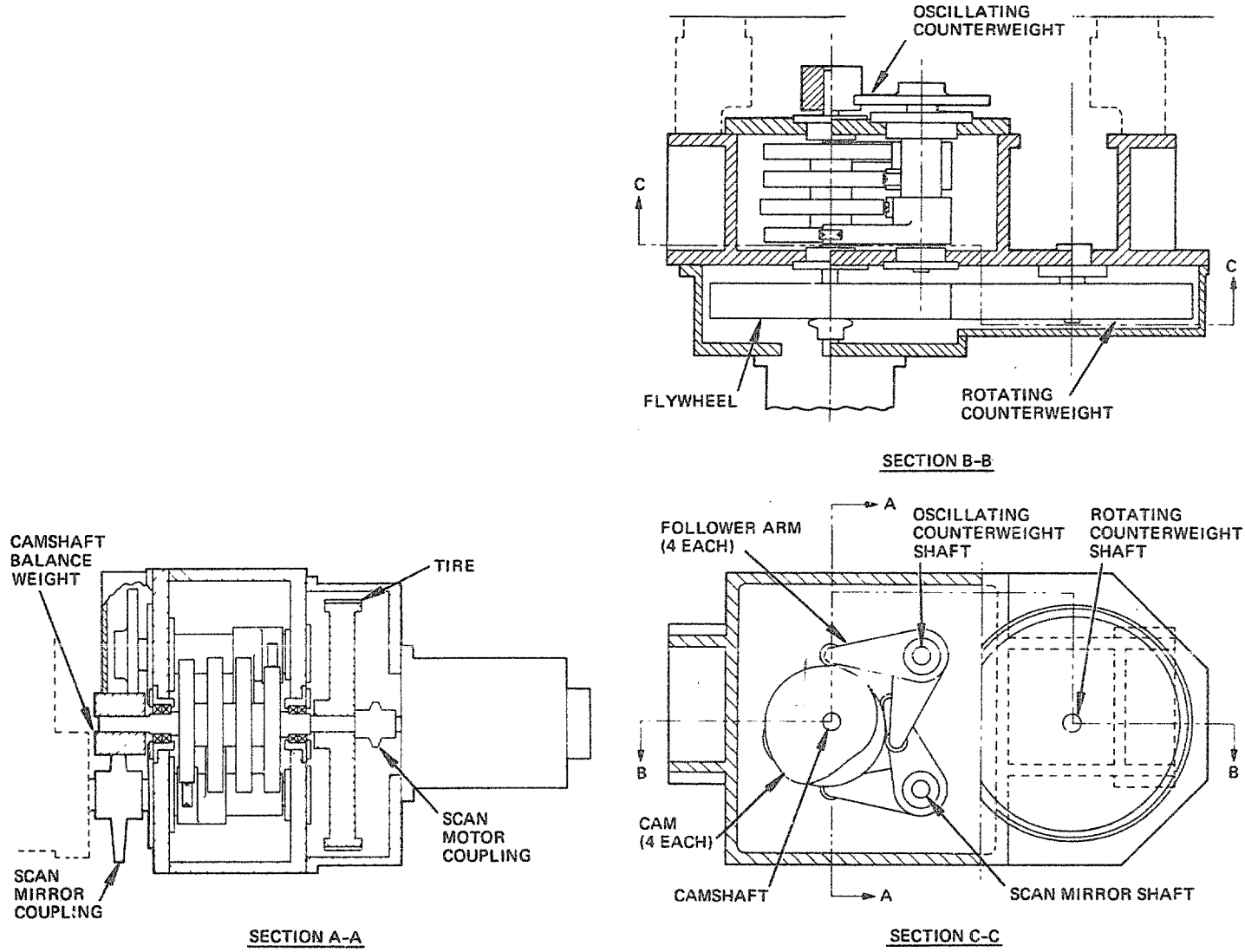

Figure 6. Scan drive details.

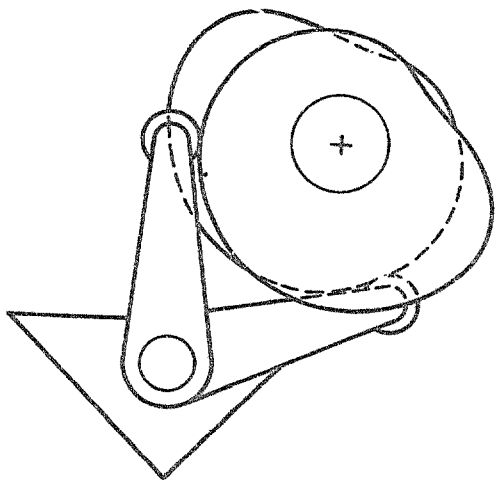

Figure 7. Conjugate cams.

Since the mirror velocity is constant during the scan, there is no requirement for acceleration--the mirror and scan drive are simply coasting. During scan the mirror is moved slowly forward; during retrace it is moved rapidly backward. The faster speed means it has more rotational energy. This energy comes from the cam, which must slow down in giving up its energy. As the mirror again changes direction and moves slowly forward for the next scan, it returns this energy to the cam, returning it to its original speed, which is the proper speed for scanning. The rotational energy of

it would occupy if the scan were perfectly linear. Since a pixel is a milliradian, a tenth of a pixel is a tenth of a milliradian. Accounting for the optical doubling produced by the scan mirror, this converts to 0.05 mrad on mirror position. Since the range of mirror positions is 16.8 deg, this is about one part in 6,000. Again, if the follower arm is 3 in. long, $\pm$ 0.05 mrad converts to $\pm$ 0.00015-in. tolerance on the position of the follower. This $\pm$ 0.00015 in. is the total error budget, and includes follower and camshaft bearing runout, two cam profiles (the cam and conjugant cam), and dynamics due to flexing during operation. It is clear from these numbers that the 0.1-pixel tolerance was a formidable challenge; for the cumulative error, it was considered a goal rather than a firm specification.

A precision encoder was used to measure the performance of the scan drive. The precision encoder was not attached to the end of the scan mirror because the shaft connecting the mirror to the encoder and the encoder disk are a spring-mass system whose motion would be different from the mirror's. Rather, the scan mirror was removed and the encoder was attached to the scan drive with a test inertia and shaft. Care was taken to match the shaft stiffness and test inertia to the scan mirror shaft stiffness and scan mirror inertia. This assured that the motion of the encoder disk in the test setup matched the motion of the mirror in the flight configuration.

The encoder generates 11,250 pulses in one revolution. The time between pulses is recorded by the GSE computer. The error in scanner look direction is obtained by the following analysis. The number of pulses in the linear scan is

$$16.8 \text{ deg} \times \frac{11{,}250 \text{ pulses}}{360 \text{ deg}} = 525 \text{ pulses}$$

$$1 \text{ pulse} = \frac{2{,}000\pi \text{ mrad}}{11{,}250 \text{ pulses}} = 0.5585 \text{ mrad}$$

Let t_i be the time between pulse i and pulse i-1. Then the mirror position error at the time of pulse k is

$$e_k = \begin{pmatrix}\text{actual position of pulse k} \\ \text{at the time pulse k occurs}\end{pmatrix} - \begin{pmatrix}\text{ideal position of pulse k} \\ \text{at the time pulse k occurs}\end{pmatrix}$$

$$= (k - \bar{\omega}\sum_{1}^{k} t_i) \times 0.5585$$

$$= \left(k - \frac{525}{\sum_{1}^{525} t_i} \times \sum_{1}^{k} t_i\right) \times 0.5585 \text{ mrad} \qquad (1)$$

Equation (1) gives the mirror position referenced to the beginning of the scan, in milliradians. The pixel-to-pixel error within a scan line is determined by

$$e'_k = e_k - e_{k-1} \qquad (2)$$

The optical look direction errors are double the mirror position errors calculated by Equations (1) and (2). They are given in Table 1 for a variety of operating conditions. In the table, column headings Q1, Q2, Q3, and Q4 refer to the 1st, 2nd, 3rd, and 4th quarters of the scan line, respectively. The values in the table are the maximum errors observed in each quarter of the scan profile.

Several observations can be made from Table 1. Over the expected temperature range of 0 deg C to 10 deg C, the maximum error from the start of the scan is about 0.26 mrad, or 0.26 pixel. (The start of the scan is controlled to within 0.05 pixel of nominal by a signal from an onboard gyro. The nominal condition is defined as having the center pixel of the scan at nadir.) The error can be positive or negative, resulting in a mismatch of up to 0.52 pixel from one scan line to the next, but within a scan line, no pixel deviates by more than 0.26 pixel from the position it would have if the scan profile were perfectly linear. This is well within the required performance envelope. The 0.52-pixel mismatch is along the start of scan edge (left-hand edge) of the picture only. The mismatch decreases to a maximum of about 0.28 pixel at the right-hand edge of the picture. This improvement in performance as the scan line proceeds is due to damping out of disturbances produced by the torques on the mirror (and follower) during retrace. These torques may be thought of as a one-two punch, one clockwise and one counterclockwise.

The next observation is that the pixel-to-pixel error is, at worst, 0.06 pixel, which is also within the required performance envelope. There were approximately 50 hours of operation on the scan drive at the last scan profile measured. It has been observed, however, that there is a gradual degradation in performance with time. The reasons for the degradation appear to be settling of joints and/or deformation of inadequately hard materials. These measurements will be repeated after the first season of operation and compared with the results shown in Table 1. Table 2 summarizes the results of Table 1 and compares them with the scan dynamics requirements as they were finally defined.

5. CONCLUSION

Both performance requirements for the AVIRIS scanner have been met. The pixel-to-pixel linearity within a scan line was measured to be 0.06 mrad or better; the goal was 0.1 mrad. The second goal was that the position of any given pixel within a scan line not deviate by more than 0.5 mrad from the position it would have if the scan were perfectly linear; the measured performance was 0.26 mrad or better. The result of this performance is excellent image geometry in the raw flight data. Figure 8 is an AVIRIS image of Rogers Dry Lake at Edwards Air Force Base, California. The only computer processing that was done was a simple stretch to enhance the contrast. Note the map-like quality of the image and the lack of obvious distortions. This image is in the 1.026-μm spectral band.

Table 1. Scan Profile Error

		Cumulative Error From Scan Start (mrad)				Pixel-to-Pixel Error (mrad)			
Date	Temp	Q1	Q2	Q3	Q4	Q1	Q2	Q3	Q4
9/08/86	RT[1]	0.329	0.183	0.105	0.102	0.045	0.029	0.014	0.019
9/08/86	RT	0.217	0.135	0.116	0.091	0.039	0.031	0.019	0.021
9/10/86	RT	0.161	0.063	0.063	0.079	0.033	0.023	0.021	0.016
9/10/86	0 deg C	0.202	0.159	0.155	0.141	0.063	0.049	0.035	0.019
9/10/86	0 deg C	0.115	0.094	0.128	0.115	0.039	0.025	0.025	0.014
9/11/86	30 deg C	0.181	0.120	0.090	0.097	0.040	0.039	0.024	0.016
9/11/86	0 deg C	0.258	0.257	0.197	0.132	0.063	0.058	0.034	0.021
9/11/86	30 deg C	0.109	0.064	0.087	0.091	0.029	0.016	0.021	0.011
9/11/86	30 deg C	0.165	0.075	0.069	0.072	0.036	0.031	0.016	0.016
9/17/86	RT	0.316	0.192	0.090	0.082	0.047	0.026	0.024	0.021
9/17/86	10 deg C	0.130	0.111	0.075	0.095	0.043	0.028	0.018	0.018
9/17/86	10 deg C	0.154	0.109	0.110	0.102	0.038	0.022	0.018	0.013
9/17/86	10 deg C	0.161	0.094	0.073	0.091	0.038	0.032	0.018	0.017
9/18/86	5 deg C	0.180	0.146	0.126	0.142	0.035	0.020	0.020	0.020
9/18/86	5 deg C	0.146	0.140	0.096	0.106	0.030	0.020	0.015	0.015
9/18/86	5 deg C	0.174	0.137	0.085	0.073	0.035	0.025	0.020	0.015
9/18/86	15 deg C	0.173	0.134	0.103	0.098	0.045	0.030	0.020	0.015
9/18/86	15 deg C	0.202	0.173	0.114	0.102	0.040	0.035	0.015	0.015
9/18/86	15 deg C	0.227	0.139	0.119	0.119	0.045	0.025	0.015	0.015
9/19/86	RT	0.459	0.260	0.139	0.115	0.056	0.041	0.021	0.016
9/19/86	RT[2]	0.600	0.436	0.252	0.191	0.072	0.048	0.018	0.018
9/19/86	RT[2]	0.556	0.399	0.271	0.154	0.058	0.052	0.033	0.027
9/19/86	RT[2]	0.565	0.399	0.246	0.232	0.064	0.054	0.021	0.024

[1]Room temperature.
[2]Without rotating counterweight.

everything on the camshaft during scan must be much greater than the rotational energy of everything on the mirror shaft (mirror and cam follower) or else the camshaft will slow down significantly during retrace, thereby reducing scan efficiency. The cam design assumes a constant-speed cam in order to avoid the challenge of predicting exactly how much slowdown occurs during retrace. Hence, the next addition to the simple concept is a flywheel on the camshaft.

The requirement for vibration-free operation has not yet been addressed. If the angular momentum of the system, which includes everything on the camshaft plus everything on the mirror shaft, is plotted over the scan-retrace cycle, it is not constant. This can be understood by considering the following. Since the system is conservative (nearly), $\frac{1}{2}I_1\omega_1^2 + \frac{1}{2}I_2\omega_2^2$ is constant. Here I_1 and I_2 are the inertias of everything on the mirror shaft and camshaft, respectively; ω_1 and ω_2 are the rotational speeds of the mirror shaft and camshaft, respectively. For the angular momentum to be constant, $I_1\omega_1 + I_2\omega_2$ must be constant. The only ways to satisfy both of these equations are for $I_1 = I_2 = 0$, or for $\omega_1 = \omega_2 = 0$, or for $I_1 = I_2$ and $\omega_1 = -\omega_2$. None of these is the case for the scan drive, and hence the angular momentum varies during the cycle. The rate of change of momentum requires a torque to produce it; the housing must exert a torque on the system consisting of the two shafts. In turn, the housing exerts a reaction torque on the structure that holds it: the foreoptics. This is just what needs to be avoided. The solution is to add two more elements. One is an oscillating counterweight with a follower arm and the same inertia as the scan mirror. The oscillating counterweight is driven by two more cams on the camshaft so that its motion is equal and opposite to the motion of the scan mirror and its follower. The other is a rotating counterweight. Its inertia matches the inertia of everything on the camshaft, and its motion is equal and opposite to the camshaft motion. This is a brute-force approach that satisfies one of the conditions for constant angular momentum, namely, for each I and ω, there is an equal I and an equal and opposite ω.

The requirement for scan linearity calls for a constant camshaft speed during the scan. Two ways of achieving this were considered: to measure the mirror position during scan and apply more or less torque to the camshaft as required, or to put a large inertia on the camshaft and rely on it to maintain constant speed. Both options appeared suitable, but the latter was chosen primarily because the early design work and breadboard hardware were made that way and functioned well. The selected approach requires only a low-resolution mirror encoder and a slow servo. In fact, the servo purposely ignores speed variations within one revolution--its only task is to maintain the correct number of revolutions per second. It is the task of the flywheel to maintain constant speed within one revolution.

This completes the description of the unusual features of the scan drive. A synopsis of the scan drive design follows.

The mirror shaft has a pair of follower arms which are driven by conjugate cams. The camshaft has a second pair of conjugate cams, which drive an oscillating counterweight with a motion equal and opposite to the scan mirror motion. The camshaft is motor-driven at constant speed and includes a flywheel. A rotating counterweight is driven with a motion equal and opposite to the camshaft motion. The rotating counterweight is a wheel equal in diameter to the flywheel on the camshaft. The flywheel drives the rotating counterweight by a friction drive: the outside diameter of each wheel is a 1/8-in.-thick rubber (polyurethane) tire. The camshaft is driven by a three-phase induction motor. All four shafts of the scan drive (camshaft, mirror follower shaft, oscillating counterweight shaft, and rotating counterweight shaft) are mounted in Barden Precision Ball Bearings (duplex pairs). The lubrication is Braycote 600 grease. The couplings attaching the motor to the camshaft and the output shaft (scan drive) to the scan mirror shaft (foreoptics) are metal bellows couplings with zero backlash. The motor and the scan mirror have optical encoders to permit control of the instrument by the electronics. The scan drive is attached (bolted and pinned) to the foreoptics and supports the scan drive electronics. This entire assembly is the scanner. The scanner attaches to the aircraft via four elastomeric mounts to isolate the scanner from the aircraft vibrations.

4. PERFORMANCE MEASUREMENT

The most critical scan profile performance specification was 0.1-pixel linearity over the full scan (see Figure 3). This means that the center-to-center spacing between adjacent pixels should not vary by more than 0.1 pixel. A tenth of a pixel is a very desirable tolerance. If it could be met, the instrument would provide an excellent image in the geometric sense, and computer data processing requirements would be minimized. The second specification was that the cumulative error in pixel position over an entire scan not exceed 0.5 pixel, i.e., no pixel should be more than 0.5 pixel from the position

Table 2. Scan Dynamics Requirements

Description	Required Performance	Measured Performance
Scan rate	12 scans/sec	12 scans/sec
Cumulative pixel position error over scan (pixel size = 1.0 mrad)	0.5 mrad	0.26 mrad
Maximum pixel-to-pixel position error	0.1 mrad	0.06 mrad
Angular motion of scan drive housing due to vibration	0.1 mrad	0.01 mrad

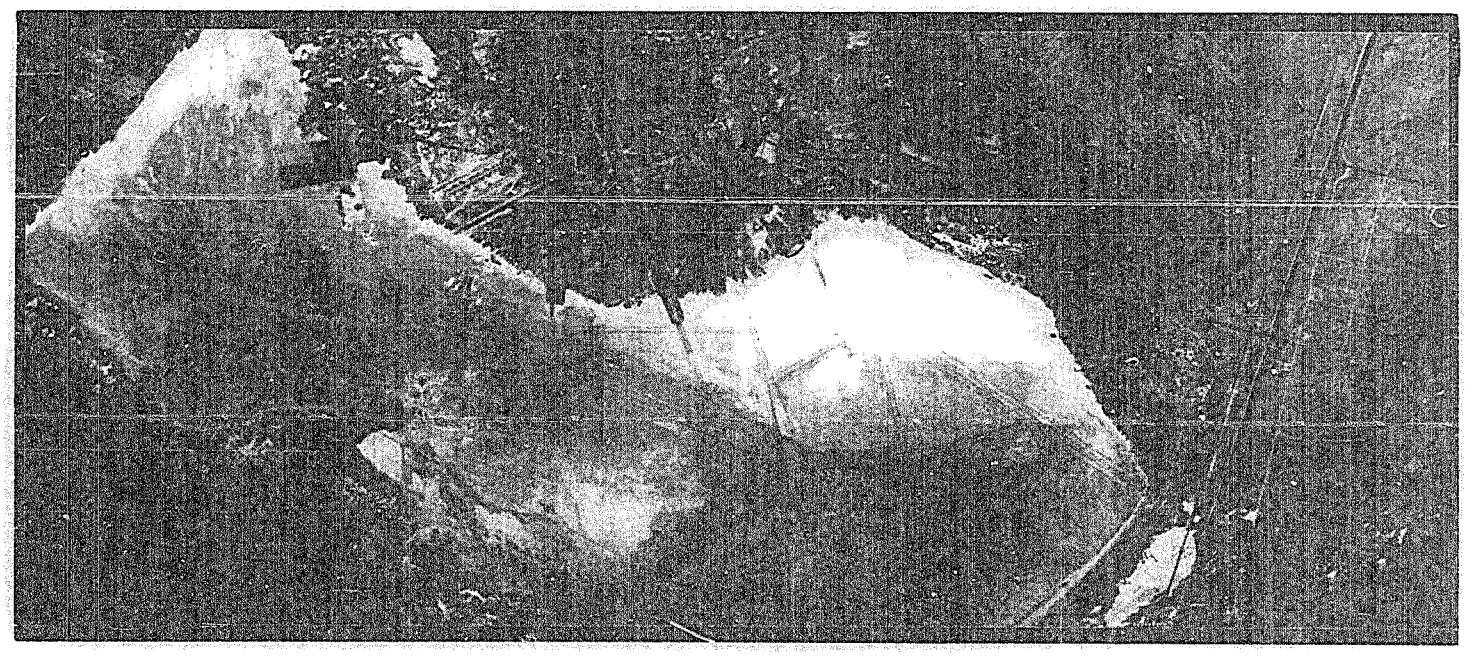

Figure 8. AVIRIS image of Rogers Dry Lake.

Additional improvements might yet be made in a scanner of this type by the use of materials with a higher stiffness-to-weight ratio, such as beryllium or metal matrix composites. With these materials and careful attention to detail, it is estimated that the scan profile errors achieved with this design could be reduced by nearly half or the scan efficiency increased to as much as 80% or 85%.

6. REFERENCE

1. John Charles Starkus, "Large Mirror Assembly of the New Thematic Mapper Developed for LANDSAT 4 Earth Resources Satellite," in Infrared Technology IX, Irving J. Spiro and Richard A. Mollicone, editors, Proc. SPIE 430, 85-91 (1983).

7. ACKNOWLEDGMENT

The research described in this paper was carried out by the Jet Propulsion Laboratory, California Institute of Technology, under a contract with the National Aeronautics and Space Administration.

SIGNAL CHAIN for the Airborne Visible/Infrared Imaging Spectrometer (AVIRIS)

James S. Bunn, Jr.

Jet Propulsion Laboratory
California Institute of Technology
4800 Oak Grove Drive, Pasadena, California 91109

ABSTRACT

The AVIRIS instrument has a separate dedicated analog signal processing chain for each of its four spectrometers. The signal chains amplify low-level focal-plane line array signals (5-10 mV full-scale span) in the presence of larger multiplexing signals (~ 150 mV) providing the data handling system a ten-bit digital word (for each spectrometer) each 1.3 μs. This signal chain provides automatic correction for the line array dark signal nonuniformity (which can approach the full-scale signal span).

1. INTRODUCTION

The Airborne Visible/Infrared Imaging Spectrometer (AVIRIS) is a collection of four spectrometers monitoring the spectrum over the range from 0.4 to 2.45 μm. In each spectrometer the input optical signals are converted into electrical signals by a line array focal-plane assembly (FPA) shown schematically in Fig. 1. Details of the FPAs are discussed in a companion paper.[1]

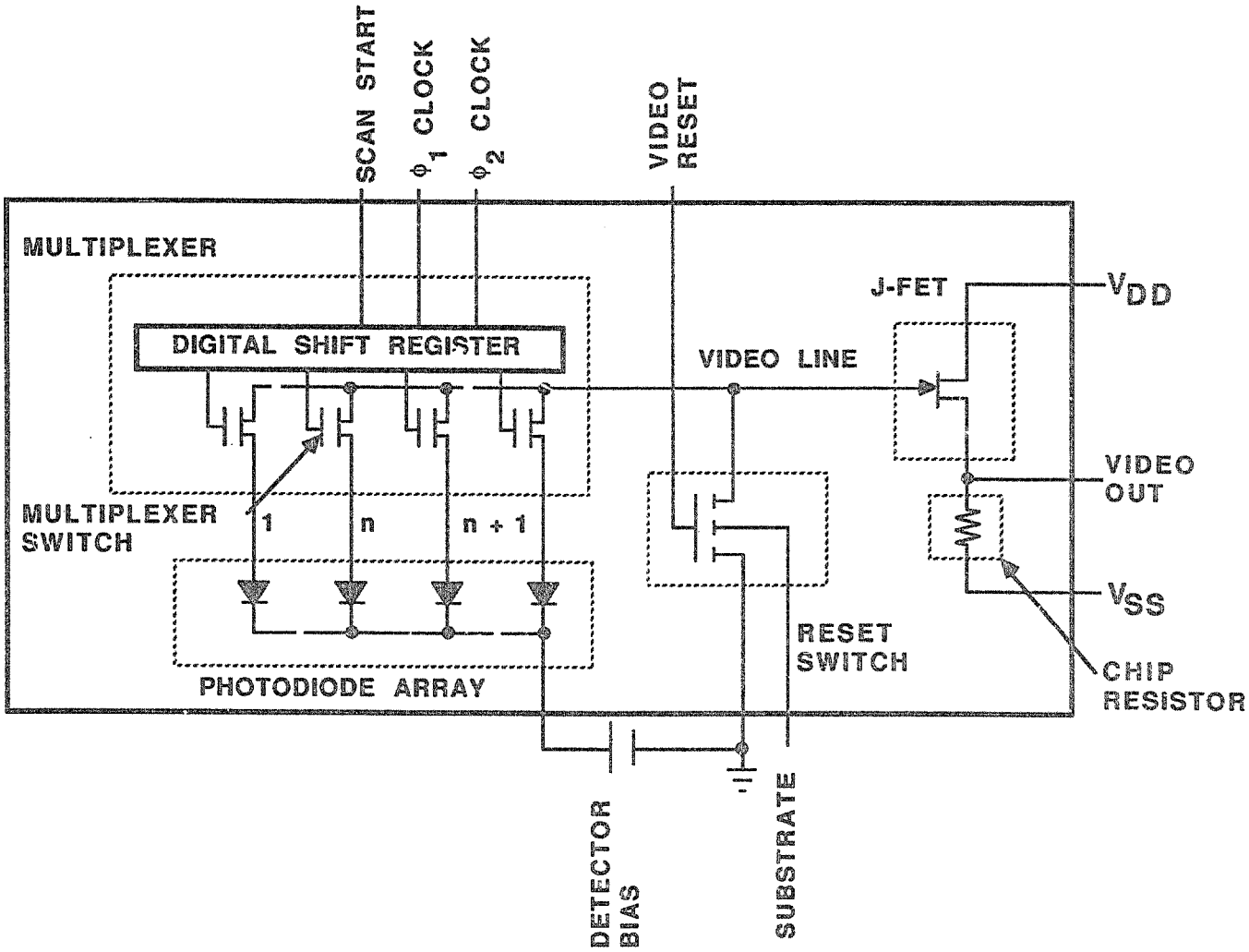

Figure 1. Focal-plane schematic.

The FPA consists of a line array of detectors (32 detector elements for the silicon visible array and 64 detector elements for each of the indium antimonide infrared arrays), a shift register/multiplexer (used to access each detector in sequence), a biasing/reset MOSFET switch and a video output junction FET (JFET) buffer amplifier. When a detector is selected, its output is switched onto the gate of the JFET follower. The follower output provides the low-impedance FPA output signal (VIDEO OUT).

The video signal is shown in Fig. 2. As each detector is selected, the signal (positive-going from the dark level) is available for about 800 ns. The detector is then reset (biased) by turning on the MOSFET reset switch for about 331 ns. The reset switch is opened, and 166 ns later the multiplexer switches the next detector onto the VIDEO LINE.

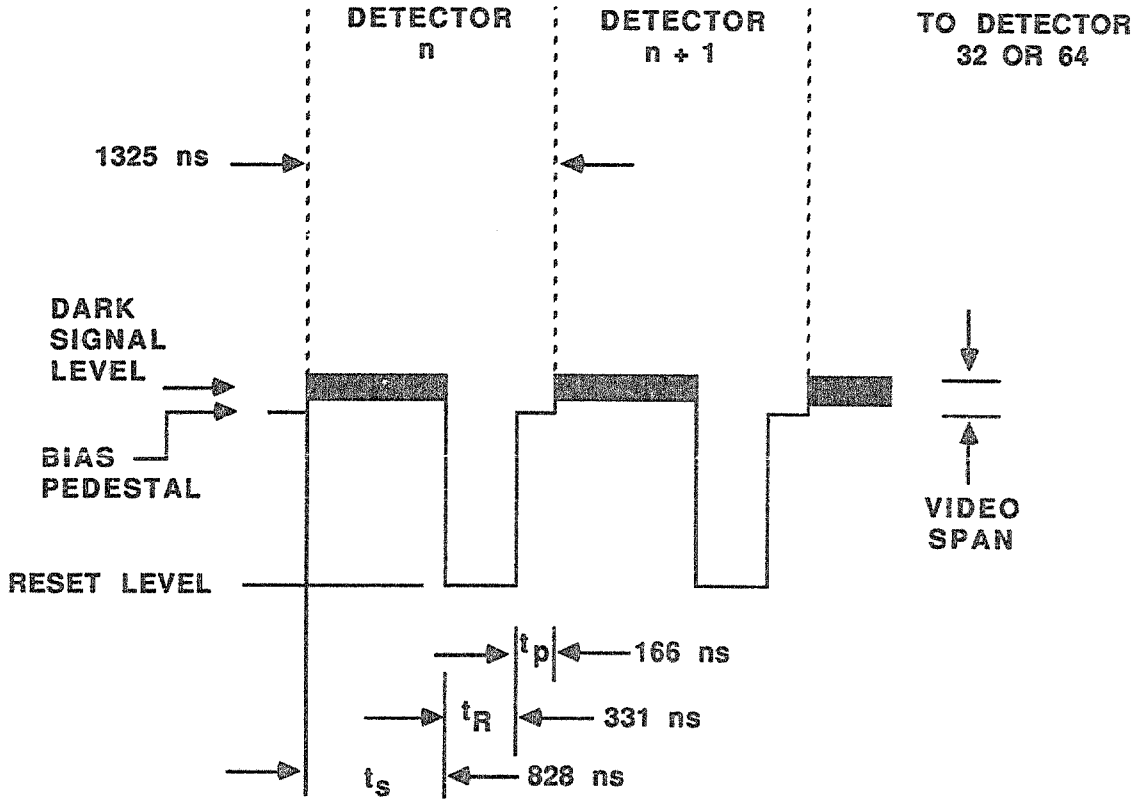

Figure 2. FPA VIDEO OUT.

Each detector requires 1325 ns to read out, reset, and switch to the next detector. For all arrays the readout timing is set up for 64 detectors and two dummy timing intervals to provide an array cycle time of about 87 µs. The array readout is synchronized by a roll-corrected signal scan-mirror position readout at the start of scan.

Quantitative values for the VIDEO OUT signal are listed in Table 1. The FPA JFET buffer provides the low output resistance. The signal span is small so that the signal chain gain must be several hundred V/V to raise the signal level high enough for analog-to-digital conversion (ADC).

Table 1. FPA Video Signal Characteristics

Parameter	Value	Units
Source resistance	300	Ω
Signal span	5 to 10	mV
Noise (~1 MHz NBW)	10 to 15	µVrms
Dark signal nonuniformity	~4	mVpp
Max Bias Pedestal (from reset level)	150	mV
Signal dc offset	~+0.2	Vdc

Because the dark signal nonuniformity is comparable to the full-scale signal span, the nonuniformity will occupy a significant portion of the ADC span unless corrected.

The bias pedestal refers to the voltage difference between the reset level and the signal level after the reset switch turns off (Fig. 2). For the small signal spans seen in

the AVIRIS instrument, the pedestal is 15 to 30 times the full scale span. The signal chain must recover from the overload within approximately 0.25 μs following the signal return to bias level.

The foregoing discussion describes the input interface for the signal chain. At the other end of the signal chain is the interface with the data handling system. The basic requirement is to encode the signal span into ten binary bits while preserving the signal-to-noise ratio found at the input to the signal chain.

2. THE SIGNAL CHAIN

The analog signal processing for the four spectrometers is divided into five physical locations as shown in the overall block diagram (Fig. 3). Each spectrometer has a dedicated analog signal chain which processes the FPA output (VIDEO OUT in Fig. 1).

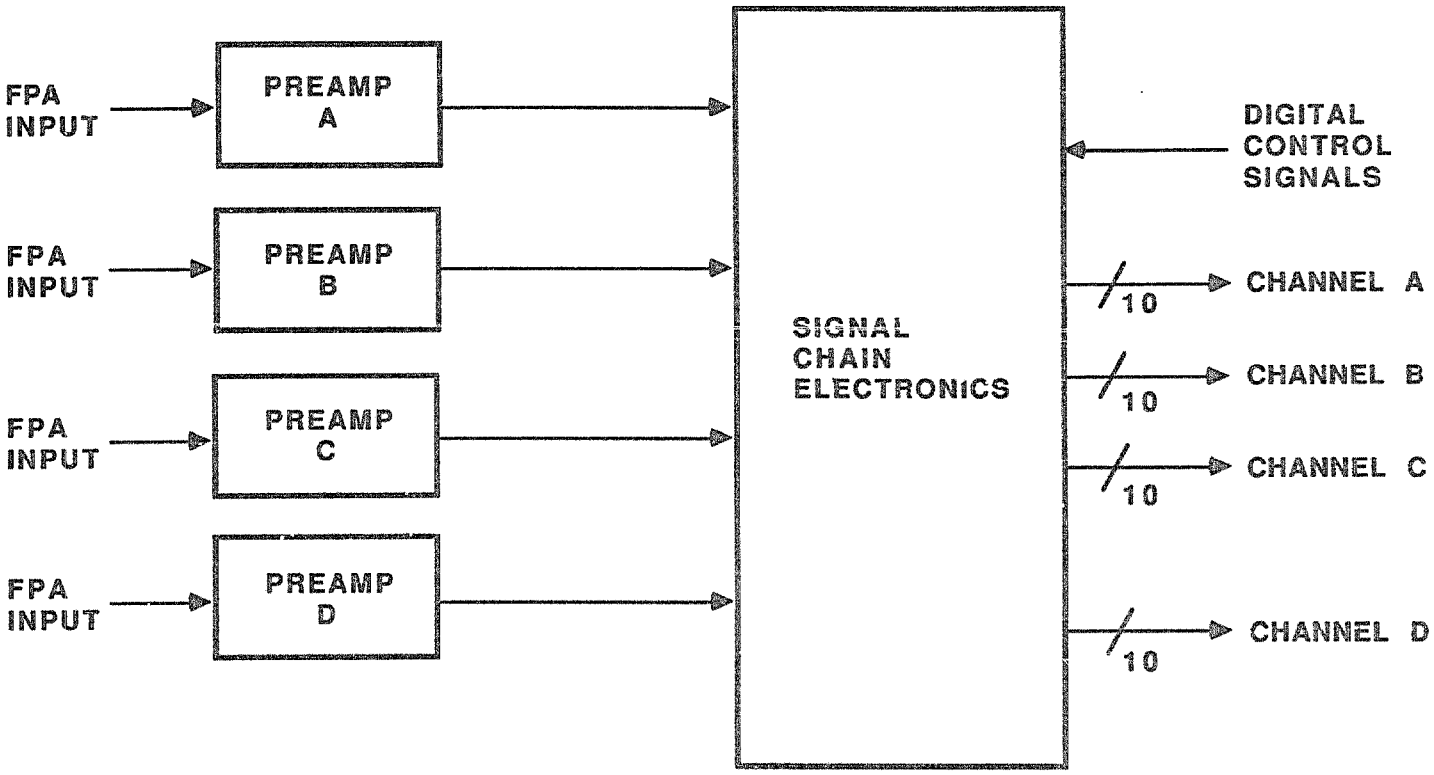

Figure 3. Analog signal processing overall block diagram.

Functionally, the signal chains do more than just amplify the detector signals. They clip the portion of the detector output not carrying signal information to prevent saturation of the signal chains. They also limit the noise bandwidth with an integrator stage and provide correction for detector nonuniformities.

The nonuniformity correction is updated at the start of the data collection run. It works by measuring the output of each of the 224 detector elements with the instrument shutter closed. These measurements are digitized to eight bits and stored in memory. As each detector element is read out during data collection, the corresponding correction measurement is recalled from memory, converted to analog form in a DAC, and subtracted from the data in analog form in the signal chain. The corrected data value is then digitized to ten bits for recording.

A preamplifier subassembly is mounted on each dewar. Each dewar houses an FPA at the optical output of each spectrometer. The preamplifier provides gain close to the FPA so that the low level VIDEO OUT signal is not exposed to interference in the instrument cable harness.

The four amplified signals are cabled to the signal chain electronics where amplification, nonuniformity correction, and integration occur. The integrated signals are digitized by four ADCs in the signal chain electronics box to provide ten-bit output words corresponding to each sampled detector measurement.

2.1. Signal processing

The preamplifier provides wideband gain (50 V/V) close to the FPA. It also limits the reset signal peaks to avoid saturation in the second amplifier stage.

Figure 4 is a block diagram for the analog electronics for one spectrometer.

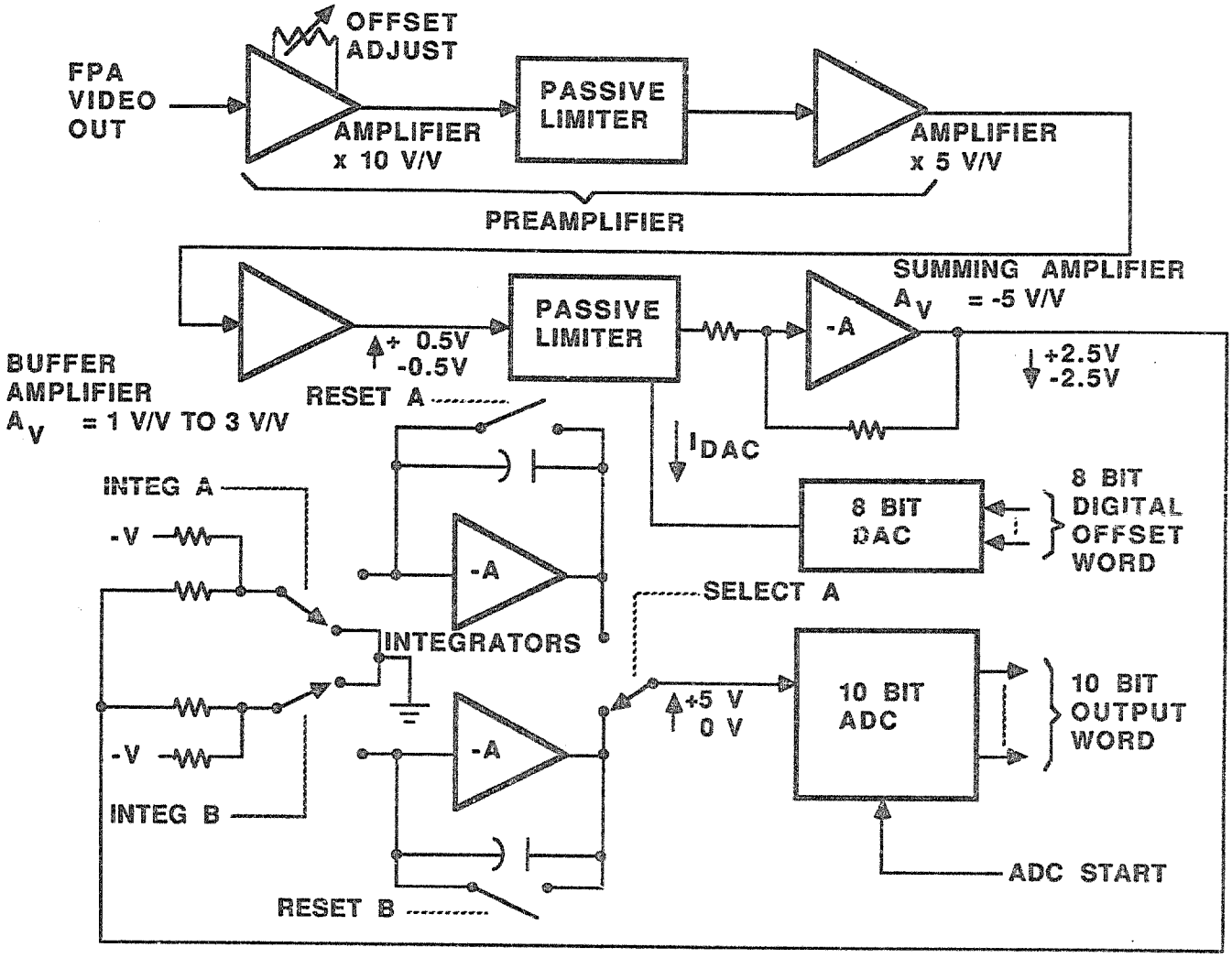

Figure 4. Analog electronics block diagram.

Each preamplifier output is cabled to the signal chain. Four sets of analog signal processing electronics are located in the signal chain electronics section, one for each spectrometer. The sets are identical except for gain tailoring to match the ADC input range with the signal available from each spectrometer.

The preamplifier output signal is received by a buffer that terminates the cable from the preamplifier and provides means for adjusting the gain in each spectrometer channel. The output of the buffer amplifier is then clipped in a fast passive limiter to remove peaks that would drive later stages into saturation. In the limiter the signal is summed with the output of an offset-correcting digital-to-analog converter (DAC) to remove detector-to-detector dark signal nonuniformity. The resulting signal is amplified to provide an analog signal to the dual integrators.

At the integrator input, the initial 5- to 10-mV signal span (from the FPA VIDEO OUT signal) has been amplified to a span of about 4 V. Guard bands (0.5 V) at the low and high ends of the signal span add 1 V to the measurement span for a total of 5 V.

The integrators set the effective noise bandwidth of the signal chain at about 600 kHz to reduce the noise contribution from the otherwise wideband signal chain. The approach employed is to operate the parallel integrators in an alternating fashion to increase the time available for analog-to-digital conversion and integrator resetting.

Figure 5 shows the integrator timing. The total time required by each detector is 1325 ns. The detector video signal is available for 828 ns. In the first 414 ns, the signal chain settles to the new analog output voltage. For illustration the signal amplitude is exaggerated and shown increasing with each successive detector. During the next 414 ns, the input of one integrator (for example, A) is connected to the video signal.

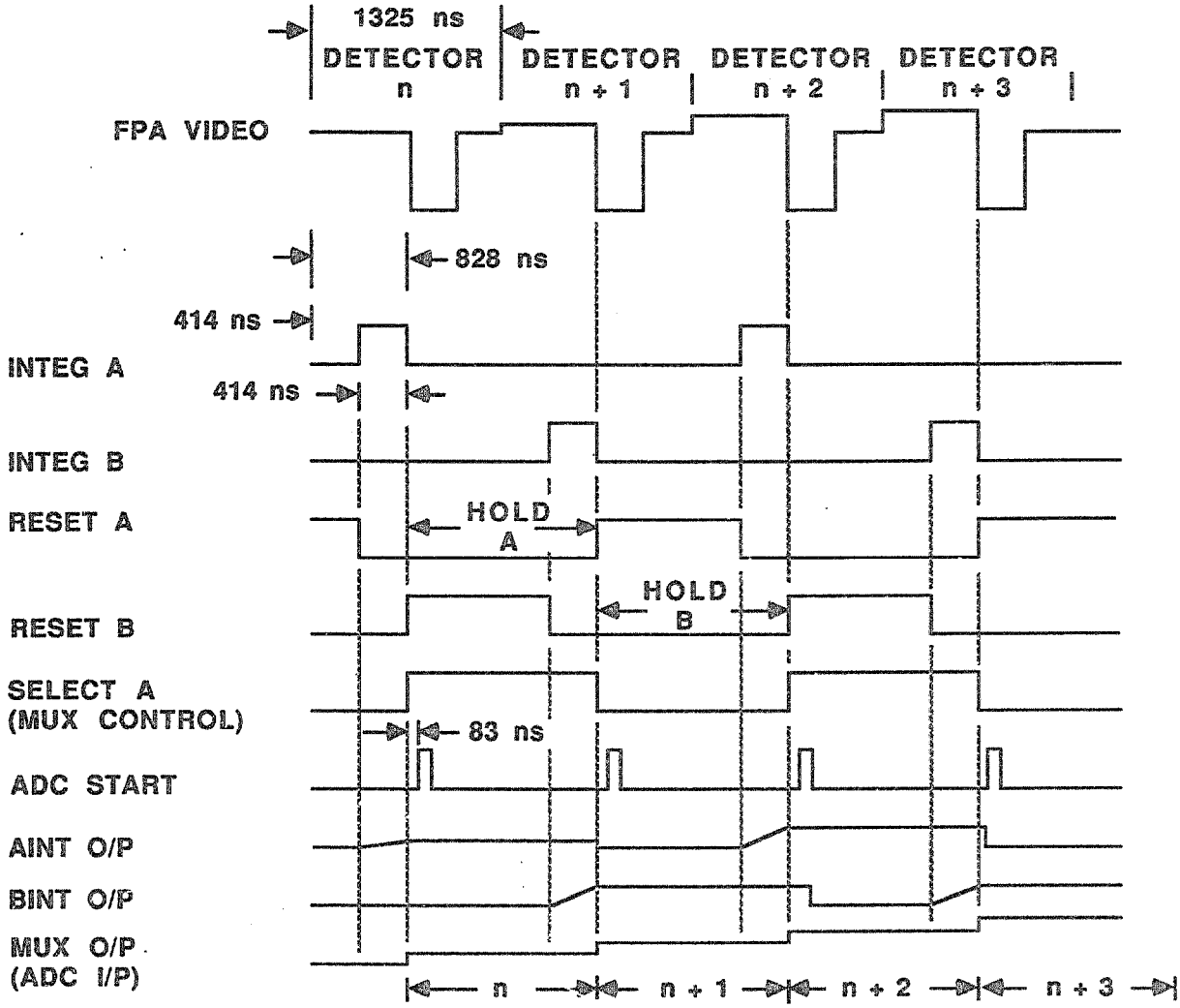

Figure 5. Integrator timing.

When the integration is completed, the ADC input switch connects the integrator A output to the ADC input. During the interval between the falling edge of INTGA and the rising edge of RESET A, the A integrator is used as a "hold" amplifier for the ADC input. The falling edge of the ADC START pulse initiates analog-to-digital conversion 166 ns later. The conversion process is completed in 900 ns maximum while the A integrator remains in the "hold" mode. The conversion is therefore complete 1166 ns after the end of integration and the ADC is ready to convert the B integrator signal. The ten-bit word resulting from the conversion is fed to the data handling system.

We noted earlier that the signal is summed with the output of an offset-correcting eight-bit DAC (Fig. 4) at the input of the summing amplifier. The purpose of this summation is to correct for the array dark signal nonuniformity and to place the dark signals near the bottom of the signal span.

The dark signal correction technique consists of storing the most significant eight bits of the ADC outputs during a special dark calibration each time the recorder is started. The stored values are used to correct the dark signal offset on a detector-element-by-detector-element basis. In addition a fixed offset is added to the signal to keep the corrected dark signal on scale.

Following each mirror scan line, the value of the corrected dark signal is measured so that drifts in the dark signal can be removed during later processing on the ground.

3. PERFORMANCE

The signal chain gains have been adjusted to values between 235 V/V and 750 V/V as required by the individual spectrometer signals. This compensates, over the instrument spectral range, for variations in the brightness of the sunlight illuminating the scene. The values used ensure that the brightest scenes viewed will not saturate the signal chains. The dark signal nonuniformity correction circuits reduce the detector-to-detector dark level variations from about 75 percent of full-scale span at worst to about 2 percent.

The measured signal chain noise performance is close to the predicted values. Combining the preamplifier equivalent input noise measurements (~ 8μVrms) and detector noise measurements (10-15 μVrms) leads us to expect an equivalent input noise range of 13 to 17 μVrms. We have obtained measurements at roughly 17 μVrms for the four spectrometer signal chains in the laboratory. However in operating situations additional noise sources were encountered so that the instrument signal-to-noise performance degraded.

The signal-to-noise (S/N) figures shown in Table 2 are for overall instrument performance. The figures account for not only the noise performance of the detectors and signal chains but all factors affecting signal level, including atmospheric transmission losses within the AVIRIS instrument and detector efficiency at each wavelength. We feel that we have identified the additional sources of excess noise measured. These problems will be addressed during the instrument upgrade this fall. The major noise source appears to be a microphonic problem with the mounting of the dewars. An additional noise contribution may be due to timing instabilities in the clocking wave forms supplied to the detectors.

Table 2. Signal-to-Noise Performance

Band	Wavelength, μm	Required S/N	Measured* S/N
A	0.7	100:1	150:1
B	1.0	---	140:1
C	1.6	---	70:1
D	2.2	50:1	30:1

*Measured performance is for integrating sphere data corrected for viewing a scene with 50 percent albedo through a standard mid-latitude midsummer atmosphere with 23-km visibility.

4. CONCLUSIONS

The AVIRIS signal chain performs well under ideal conditions, giving close to theoretical performance. It is able to extract signals within ten-bit accuracy in the face of switching transients orders of magnitude larger than a full scale signal. Compensation for dark-signal variations in individual detector elements provides correction for nonuniformities approaching the full-scale signal span.

Although noise performance for the instrument is currently below expectations (due largely to microphonics in the dewars), the signal chain is producing usable science data. The S/N specification at long wavelengths is set by the requirement to detect the kaolinite doublet. The doublet has been clearly identified in data taken to date.

5. ACKNOWLEDGMENTS

The development described in this paper was carried out by the Jet Propulsion Laboratory, California Institute of Technology, under a contract with the National Aeronautics and Space Administration.

6. REFERENCE

1. G. C. Bailey, "Visible and infrared linear detector arrays for the Airborne Visible/Infrared Imaging Spectrometer," Proceedings of the SPIE meeting held in San Diego, California, August 16-21, 1987.

AVIRIS onboard data handling and control

Ronald E. Steinkraus and Roger W. Hickok

Observational Systems Division
Jet Propulsion Laboratory, California Institute of Technology
4800 Oak Grove Drive, Pasadena, California 91109

ABSTRACT

The timing and flow of detector and ancillary data for the Airborne Visible/Infrared Imaging Spectrometer (AVIRIS) are controlled within the instrument by its digital electronics assembly. In addition to providing detector and signal chain timing, the digital electronics receives, formats, and rate-buffers digitized science data; collects and formats ancillary (calibration and engineering) data; and merges both into a single tape record. Overall AVIRIS data handling is effected by a combination of dedicated digital electronics to control instrument timing, image data flow, and data rate buffering and a microcomputer programmed to handle real-time control of instrument mechanisms and the coordinated preparation of ancillary data.

1. INTRODUCTION

The Airborne Visible/Infrared Imaging Spectrometer (AVIRIS) instrument produces solar reflectance measurements in 224 spectral bands from 0.4 to 2.4 μm for each of 614 spatial footprints in a cross-track scan encompassing a 30-deg field of view. As the airborne instrument moves along its flight path, successive scan lines are recorded, forming a data base of 224 separate flight line images.

The cross-track scan mirror operates in a scan and flyback mode at a rate of 12 scans per second with a scan efficiency of 70%. Using the instrument's roll gyro, each scan line is corrected for changes in the aircraft's roll attitude within the range of ±1.5 deg. During each flyback period, a foreoptics shutter is cycled to provide detector background data for further ground processing. At the start and end of each flight line, an in-flight calibrator with a four-position filter wheel is activated to provide data on the radiometric and spectral stability of the instrument. Throughout the flight the foreoptics focus is continuously compensated for temperature.

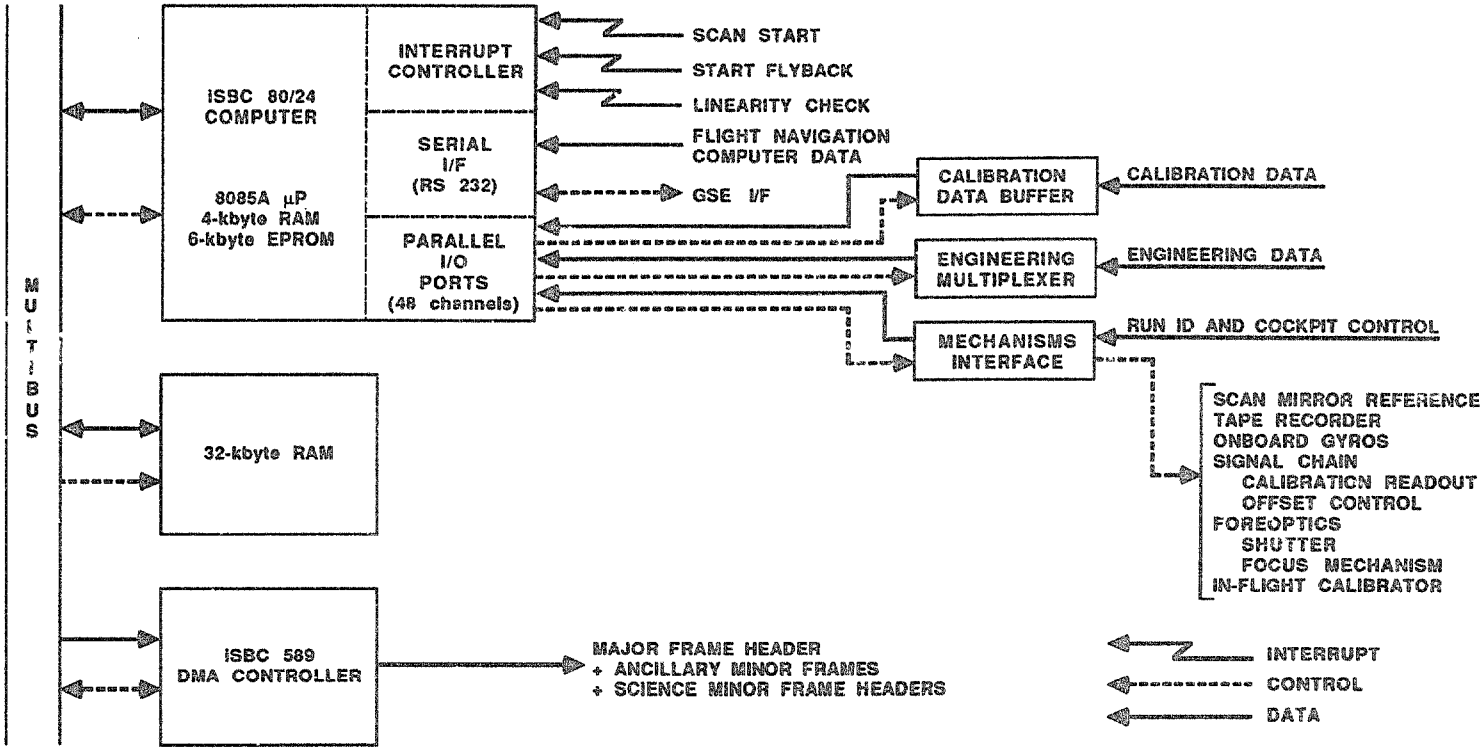

Figure 1. AVIRIS computer functionality block diagram.

The instrument's digital electronics assembly orchestrates these mechanisms to gather the data, provides timing to process the data, and formats and buffers the data to the flight tape recorder.

2. INSTRUMENT CONTROL

AVIRIS instrument operation is designed for minimum human control. Pilot interfaces consist of instrument power on/off and tape recorder start/stop. Orchestration of all instrument functions to be described here is directed from the instrument's microcomputer (Figure 1).

Housed in a multibus chassis, the microcomputer consists of an Intel SBC 80/24 single-board computer, an Intel SBC 589 direct memory access (DMA) controller board, a 32-kbyte RAM board, a custom-built engineering data multiplexer, and a custom-built mechanism control interface. The SBC 80/24 board provides an 8085A-2 microprocessor, 12 kbytes of PROM, 4 kbytes of RAM, a multi-counter programmable interval timer, an 8-level interrupt controller, one serial RS-232 interface, and six 8-bit parallel I/O ports. The DMA controller board provides direct multibus memory access for high-rate 16-bit parallel data transfers. The two custom interface boards provide for direct mechanism control and engineering data retrieval via the computer's parallel I/O ports. The computer's serial port facilitates the collection of aircraft navigation data in flight or provides full-duplex communications with the AVIRIS ground support equipment (GSE) during laboratory testing.

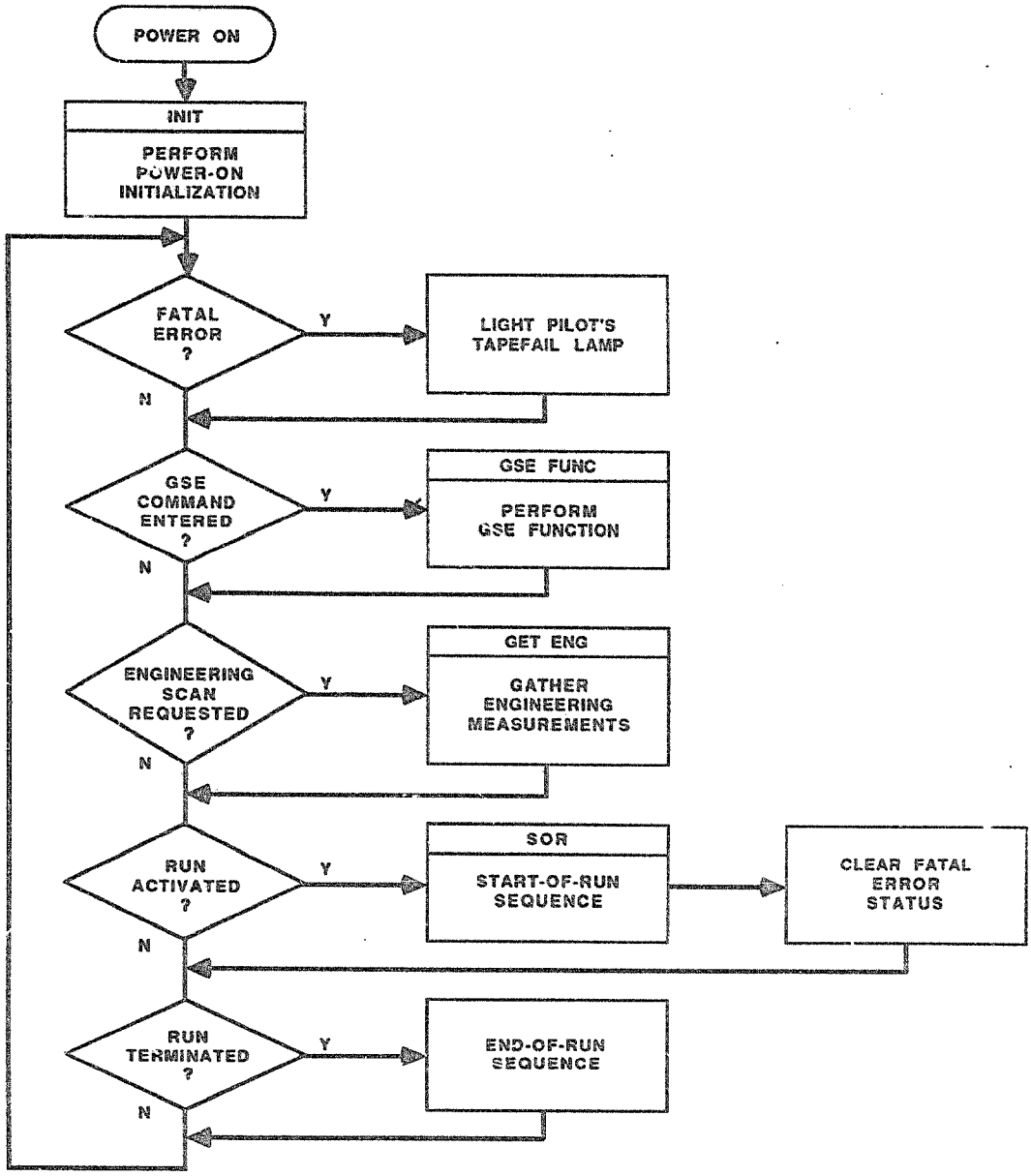

Figure 2. AVIRIS main program flowchart.

The AVIRIS firmware (Figure 2), programmed in three 2716 EPROMs, contains the instructions required to direct the instrument's operation. The main program becomes active at instrument power-on, executing an initialization routine that clears the onboard RAM (including the Run ID), initializes the onboard support chips, programs one interval timer to produce a continuous 23.4-Hz square-wave timing reference to the foreoptics scan motor, rotates the calibration filter wheel to its dark position, withdraws the focus mechanism to its reference position, powers up the tape recorder, and initializes the instrument gyros. Thereafter, the mainline firmware enters its normal top-level idle loop, where it checks for and handles occurrences of fatal mechanism errors (lighting the failure indicator on the cockpit control panel for any error), engineering minor frame requests (causing all engineering data to be read once per mirror scan), GSE commands (performing GSE functions as requested), and record start/stop commands from the cockpit control panel (performing start-of-run/end-of-run sequences as requested).

At the start-of-run, the tape recorder is started and allowed to come up to speed. The signal chain offset correction feature is updated by closing the foreoptics shutter, temporarily disabling the offset correction, and writing dark current calibration data to the offset correction buffer. The foreoptics shutter is then reopened and the offset correction reenabled. The instrument gyros are reset, the Run ID incremented, and the Major Frame Count is reset. A standard calibration sequence is activated which collects detector data for each of four in-flight calibrator filters. This is accomplished by closing the foreoptics shutter and rotating the calibration source filter wheel through its four positions (low-level broadband, spectral-line, high-level broadband, and dark), capturing a full scan line of data at each position. When the filter wheel has returned to the dark position, the shutter is then reopened and image data collection commences with the next mirror scan.

Thereafter, by means of scan-driven interrupt handling, the firmware closes the foreoptics shutter at the beginning of the scan mirror flyback period, collects a minor frame of offset corrected dark current data, and reopens the shutter prior to the start of the next scan. During the flyback period, the foreoptics focus temperature compensation algorithm may move the focus mechanism one step if the foreoptics temperature change since the last correction exceeds 0.3 deg Celsius. Initial flight data indicate that this temperature may vary as much as 5 deg Celsius during a three-hour flight, but only 0.3 deg Celsius during a flight line lasting five minutes. During each active scan interval, 11 scan mirror linearity-check and gyro engineering readings are made based on evenly spaced scan "linearity check" interrupts, and all other engineering data are gathered once per scan as a main program background activity. An additional ongoing interrupt-level firmware function (but asynchronous to the scan timing) is the processing of flight navigation data received serially from the aircraft's navigation computer at 9600 baud in bursts of 28 characters every five seconds.

At the end-of-run, the standard calibration sequence involving the in-flight calibrator is repeated and the tape recorder is stopped. The main program resumes its normal top-level idle loop until the next tape recorder start command is received from the cockpit or until the instrument's power is turned off.

Table 1. Firmware Mechanism Control Summary

Activity	Timing
Scan motor reference signal generation	Continuous
Instrument gyro initialization	Once per flight
Tape recorder power up	Once per flight
Tape recorder start/stop	Once per run
Signal chain offset correction update	Once per run
Instrument gyro reset	Once per run
In-flight calibration filter wheel rotation	Twice per run
Foreoptics shuttering	Once per scan
Foreoptics focus correction	Maximum of one step per scan

Table 2. Firmware Data Acquisition Summary

Activity	Timing
Aircraft navigation data received	Every 5 seconds
Calibration offset data read	Once per run
Four in-flight calibration data frames read	Twice per run
Calibration dark current data read	Once per scan
All engineering data sampled	Once per scan

A summary of firmware mechanism control and data acquisition responsibilities may be found in Tables 1 and 2.

To facilitate laboratory test and calibration activities, the AVIRIS GSE may utilize the flight navigation computer serial interface, enabling GSE mode commanding of the instrument. In the GSE mode, the instrument's firmware allows scan operations to continue, but disables automatic scan-driven mechanism control (i.e., shutter, focus, and in-flight calibrator mechanisms). Instead, each mechanism may be individually controlled by GSE operator command. In addition, the firmware will perform simple EPROM, RAM, and DMA controller confidence tests upon command. When exiting the GSE mode of operation, the firmware will resume normal flight operation, having first returned all GSE-moved mechanisms to their appropriate positions.

3. ANCILLARY DATA FORMATION

Ancillary data, composed of aircraft navigation data, instrument engineering data, offset data, and calibration data, are acquired as previously described via the microprocessor's parallel and serial ports. These data are buffered and formatted by the firmware according to the format described in Figure 3 in preparation for DMA output to the

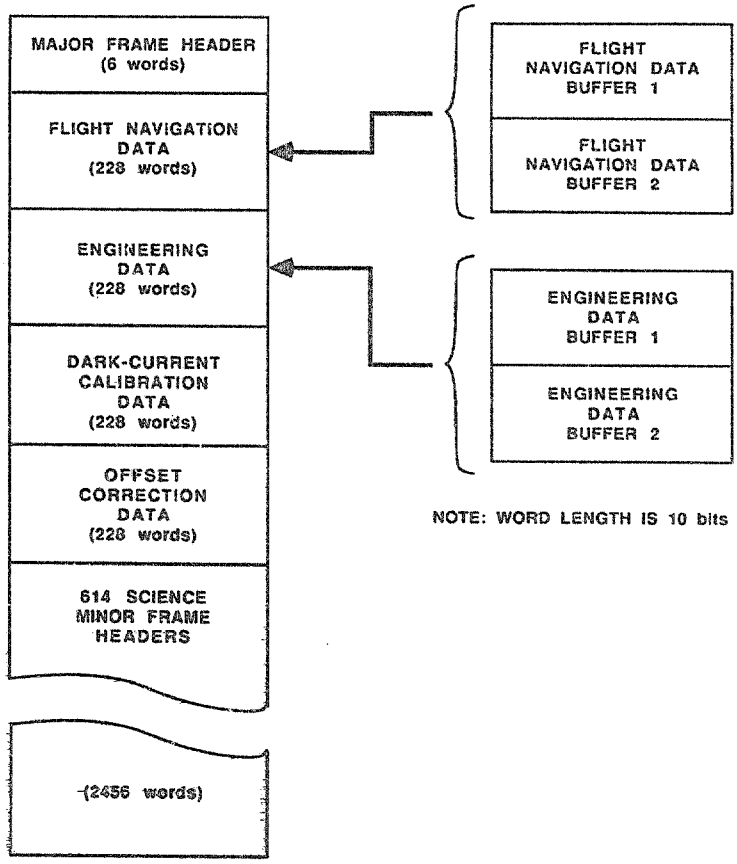

Figure 3. AVIRIS ancillary data buffer organization.

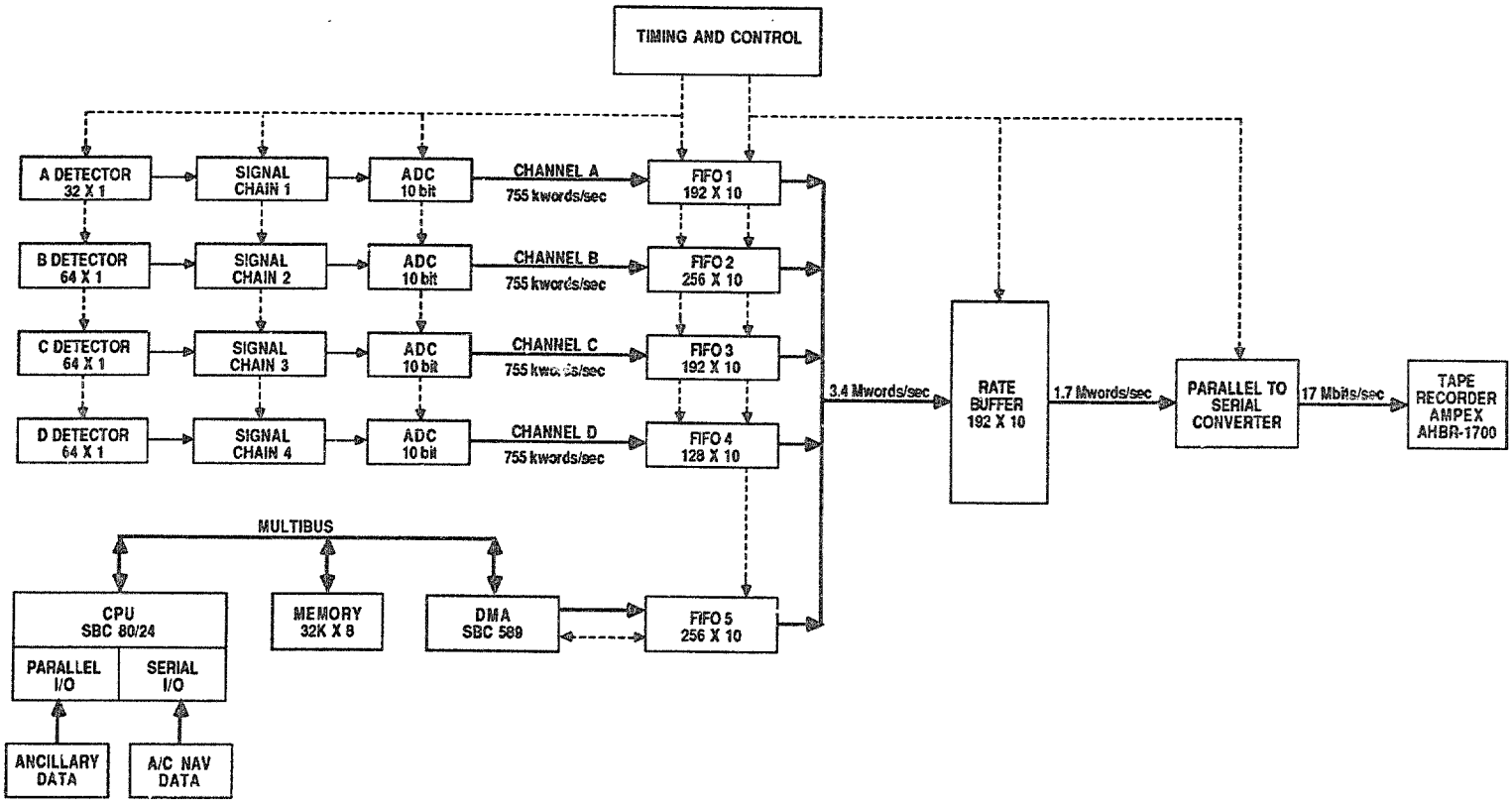

Figure 4. AVIRIS data flow block diagram.

instrument's data buffers (Figure 4) and subsequent tape recording. Included with these data are all major and minor frame headers generated directly by the firmware.

At the start of the scan mirror flyback period, a DMA operation is initiated to transfer the 3,374 (10-bit) words of ancillary data and frame header information from the ancillary data buffer to the first-in-first-out (FIFO) buffer. Transfer of 256 words is accomplished prior to the start of the next mirror scan, with subsequent transfers occurring throughout the scan line on an as-needed basis to refill the FIFO buffer. The process remains active until all words have been transferred and is reinitiated during each scan mirror flyback period.

Since new engineering and flight navigation data may be received during the DMA transfer operation, a double buffering scheme is employed for these two data types. At the start-of-flyback, the latest complete buffers of engineering and flight navigation data are copied to their places in the ancillary data buffer by the DMA controller itself, as a prelude to the output DMA transfer operation.

Because mechanism positioning and tape recorder warm-up/stop periods are required at the start and end-of-run, the synchronous nature of the tape recorder causes a number of "throwaway" frames to be recorded with the run's calibration frames on the tape. These occur prior to and immediately following the run's full sequence of image frames. Such frames are marked as "throwaway" by the firmware, and the data they contain are not normally subject to any later processing. Data frames recorded while in the GSE mode are also marked as having been produced while in the GSE mode and may be later interpreted for test or calibration purposes.

4. DATA PROCESSING

The image data flow originates with readouts from four linear focal plane arrays (Figure 4). Each is housed in its own spectrometer and measures a separate part of the 0.4- to 2.4-μm spectrum. Although three of these arrays contain 64 detector elements and the fourth 32, the readout process for each is identical. A start pulse, in conjunction with a two-phase clock supplied to the array multiplexer (Figure 5), initiates the process. As this pulse shifts through the multiplexer, FET switches successively connect each detector to a common video bus. The resultant signal is amplified by an external preamplifier and passed along to the signal chain for further processing and digitization.

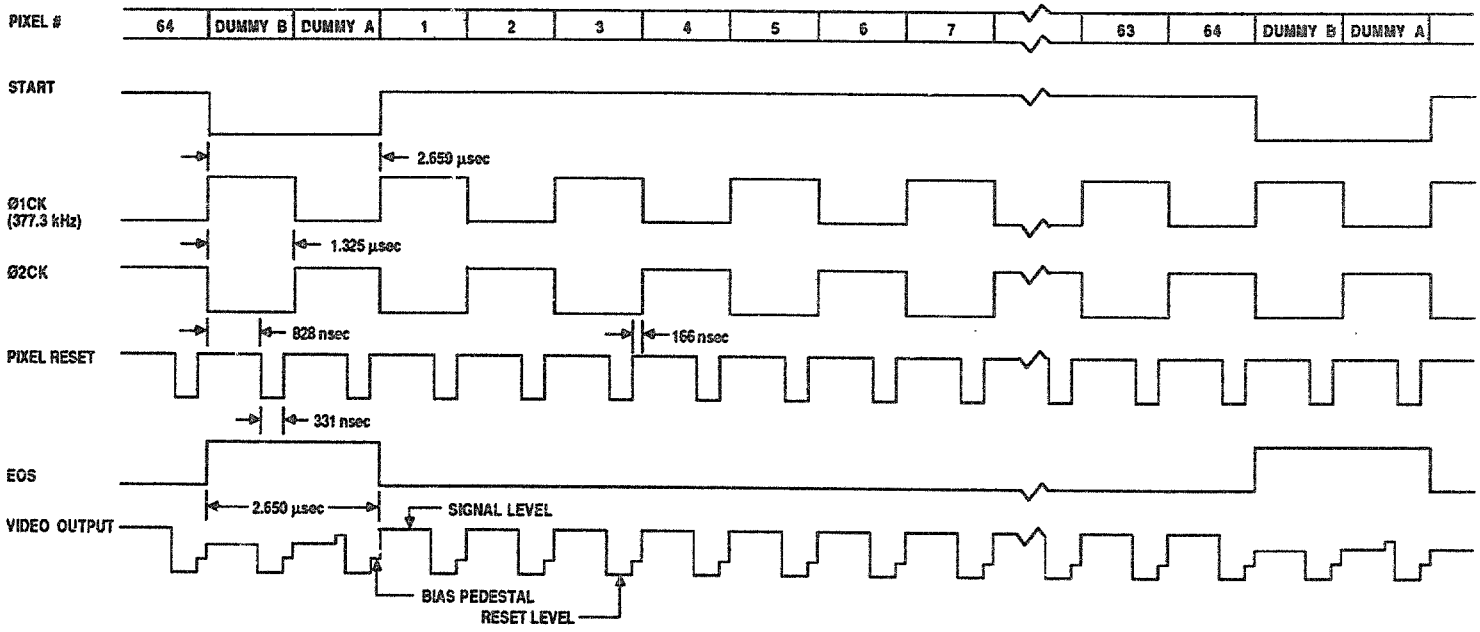

Figure 5. AVIRIS focal plane array readout timing.

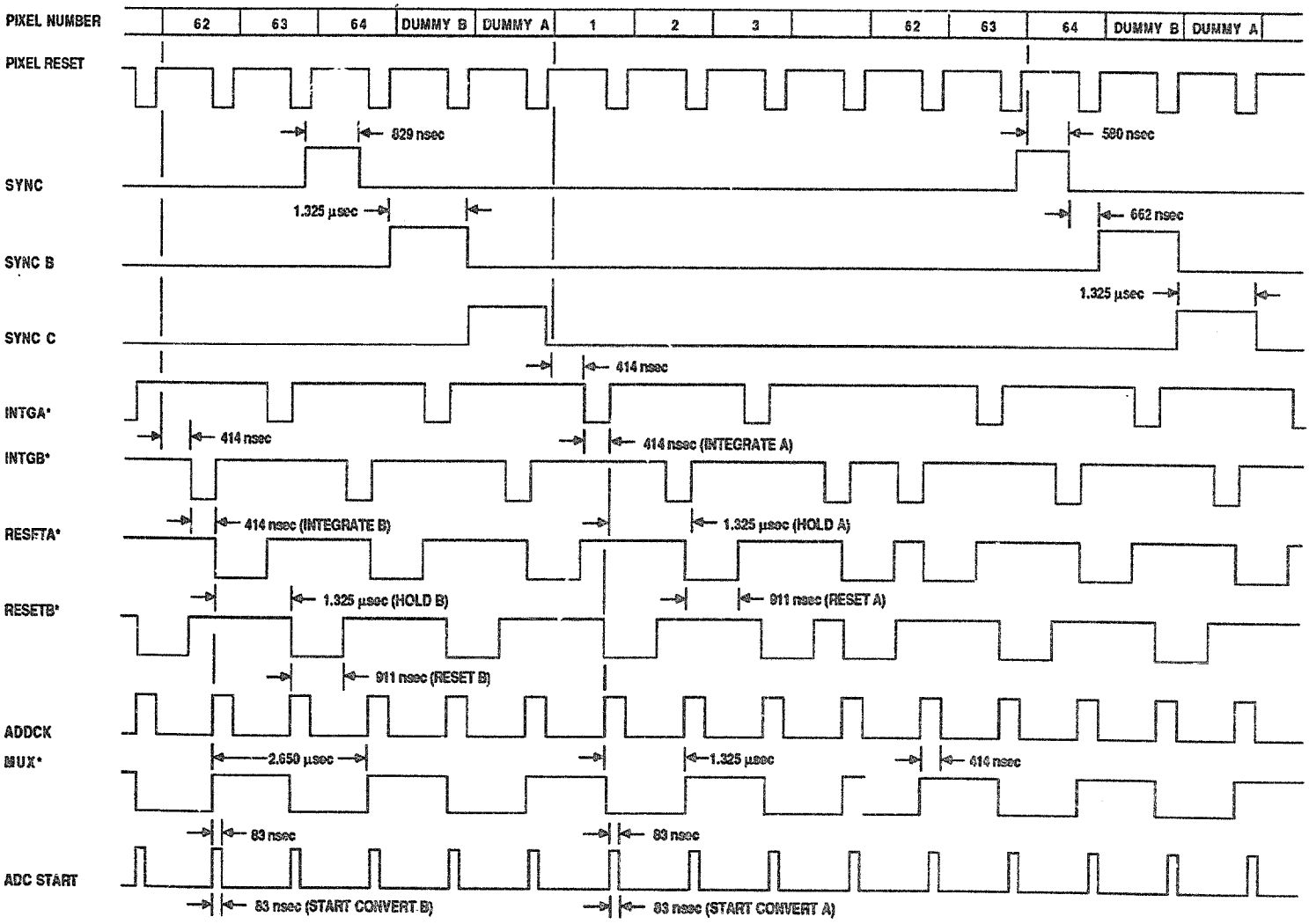

Figure 6. AVIRIS signal chain timing.

The two-phase clock, common to all four arrays, operates continuously at 377 kHz, enabling readout from each array at a rate of 7.55 X 10^5 detectors per second. Start pulses nominally occur at 87.45-μsec intervals, defining the detector integration time. Only at the start of each scan line are more frequent pulses issued to facilitate synchronization to the scan mirror motion. The digital subsystem also provides the capability to make fine adjustments to the spatial correlation between spectral data by controlling the phase relationship of start pulses issued to each array.

A dedicated signal chain and analog-to-digital converter (ADC) for each array enable the parallel processing of detector data. Preamplifier signals are further amplified, integrated, and digitized to ten bits. Timing and control signals (Figure 6), provided by the digital subsystem, are common to all signal chain channels.

Of special note is the process of offset subtraction occurring just prior to signal integration. Early in the AVIRIS system design it was noted that small changes in the detector's temperature could give rise to offset signals equal to the predicted full-scale image signal. Removal of this signal to keep the desired image signal on scale is accomplished by offset subtraction. At the start of each flight line, the foreoptics shutter is closed and the resultant offset signal is processed, digitized, and stored in an onboard memory. The shutter is reopened, and as image signals are processed, the memory data are synchronously recalled, converted to analog form, and subtracted from the appropriate detector data.

The data processing operations discussed to this point occur continually, independent of the validity of the data. Screening of invalid data such as those taken during the flyback of the scan mirror is accomplished by gating the write strobes to the FIFO buffers that receive the ADC outputs. Further data manipulations occur within these buffers, which is the subject of the next section, Data Formatting.

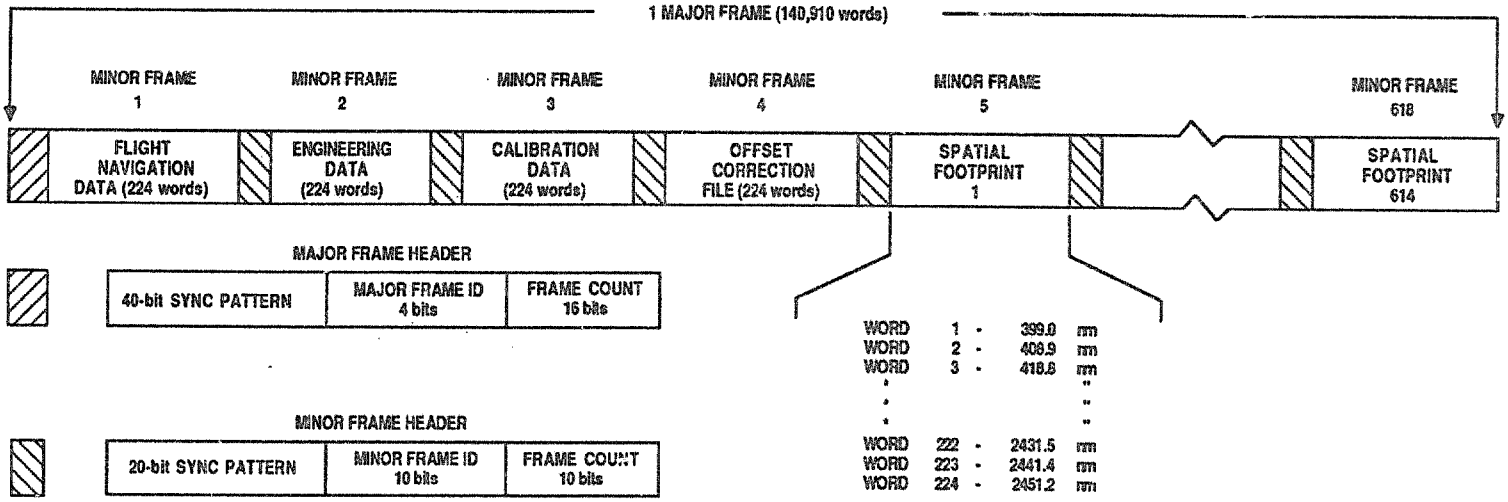

Figure 7. AVIRIS data format.

5. DATA FORMATTING

AVIRIS data are formatted according to the description in Figure 7. A major frame is equivalent to the data produced during one cross-track mirror scan. It is composed of a major frame header, containing a sync pattern, frame count, and ID, and 618 minor frames, which contain ancillary data (4) or image data (614). A minor frame consists of a four-word header, containing sync and ID, and 224 words of data. (Words are ten bits in length.) An image data minor frame organizes spectral information from the shortest wavelength measurement to the longest wavelength measurement for a specific footprint in the cross-track scan.

While this format presents the image data in a straightforward and orderly fashion, it is far from the chronological order in which the data are collected. A consequence of the AVIRIS optical design allows each spectrometer to view a different spatial footprint at any given time in the cross-track mirror scan (Figure 8). Data at the output of the ADCs, therefore, are not only spectrally misordered, but also spatially misaligned. Control of the write/read timing to the FIFO buffers is used to sort the data and place them in the required order, as illustrated in the following description.

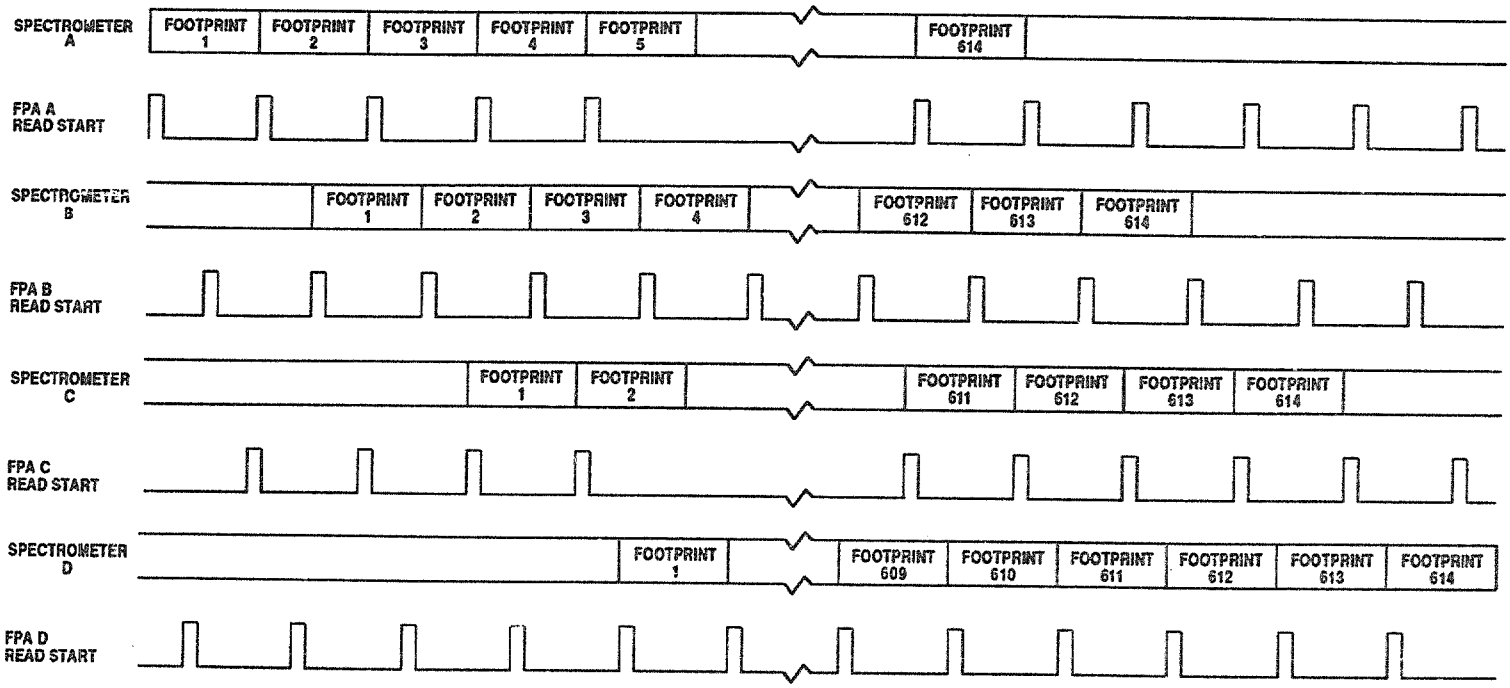

Figure 8. AVIRIS cross-track scan spatial footprint skew. This figure illustrates when each spectrometer views a particular spatial footprint. The array readouts are timed to coincide with these viewing times.

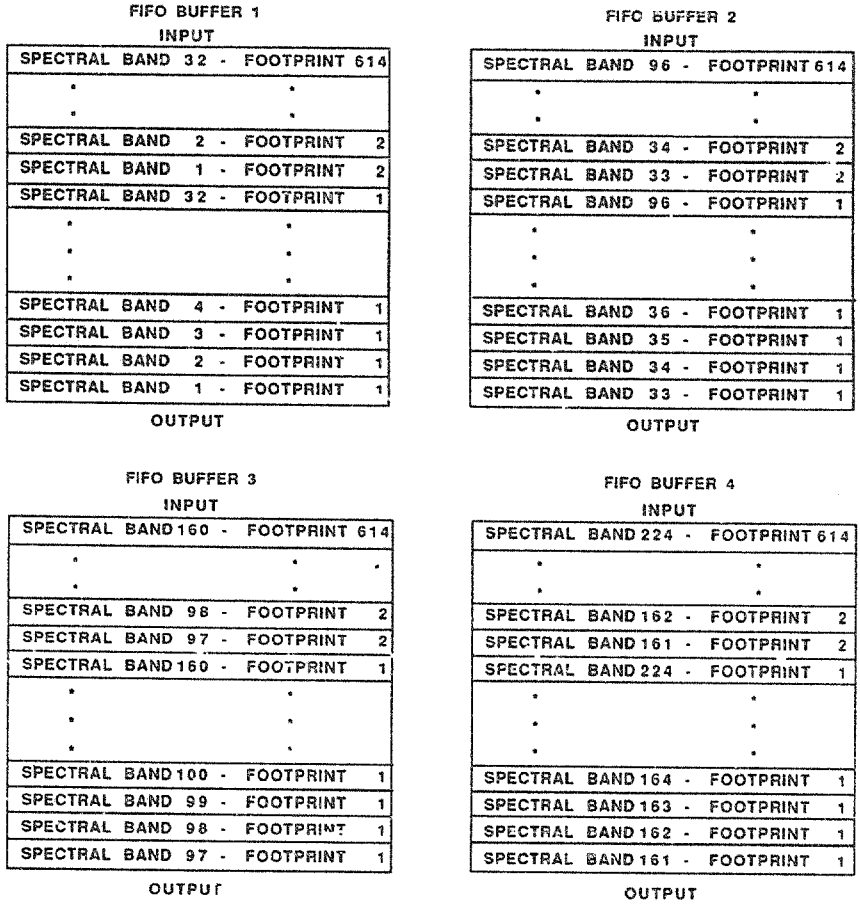

Figure 9. AVIRIS FIFO buffer fill sequence.

At the start of a scan line, the microprocessor sets up a DMA block transfer to FIFO 5 (Figure 4) containing all ancillary data and frame header information in the order defined by the AVIRIS data format. Since the data block contains more information than can be stored in the FIFO at any given time, the DMA operation continues to refill the buffer as the format routine empties it. Meanwhile, the image data processing operations have

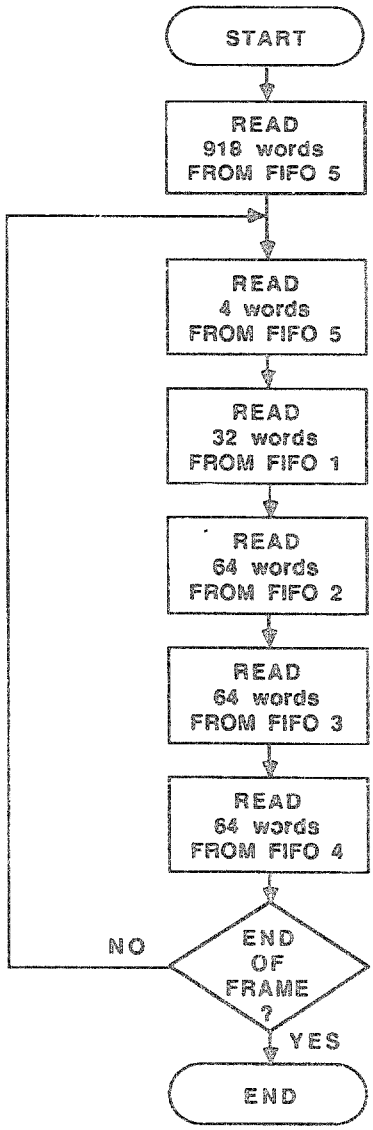

Figure 10. AVIRIS FIFO buffer read algorithm.

synchronized themselves to the scan mirror motion and begin filling FIFO buffers 1-4 with spectral information from spatial footprint one. The data in each buffer are arranged in ascending wavelengths for their respective spectrometer measurement bands (Figure 9).

As data become available at the buffer outputs, the FIFO buffer read/rate buffer write controls begin transferring data to the rate buffer (Figure 4). The process selectively moves data from FIFO buffers 1-5, as defined in Figure 10, to successive memory locations in the rate buffer, effectively building an image of the required AVIRIS format. The process continues until data from all 614 spatial footprints are collected.

The rate buffer contains enough memory to hold one major frame of data. Its purpose is to lower the continuous flow data rate to the tape recorder to an average of 17.0×10^6 bits per second from the instantaneous rate of 23.6×10^6 bits per second occurring during a cross-track mirror scan. At the averaged rate and with the data converted to a serial stream, an AVIRIS data tape will hold approximately 40 minutes of data.

6. CONCLUSIONS

The requirements for the onboard data handling and instrument control electronics created several design challenges. Among these were the need to manipulate large amounts of data at high instantaneous data rates, maximize the data storage efficiency of the tape recorder, and provide full instrument control with a minimum of pilot interface. The success of the design in meeting these challenges is demonstrated by the problem-free completion of many hours of laboratory testing and calibration as well as the successful data return from the U2 missions flown to date.

7. ACKNOWLEDGMENT

The research described in this paper was performed by the Jet Propulsion Laboratory, California Institute of Technology, under a contract with the National Aeronautics and Space Administration.

AVIRIS ground data-processing system

John H. Reimer, Jan R. Heyada, Steve C. Carpenter, William T. S. Deich, and Meemong Lee

Jet Propulsion Laboratory, California Institute of Technology
4800 Oak Grove Drive, Pasadena, California 91109

ABSTRACT

The Airborne Visible/Infrared Imaging Spectrometer (AVIRIS) has been under development at the Jet Propulsion Laboratory (JPL) for the past four years. During this same time period, a dedicated ground data-processing system has been designed and implemented to archive and process the large amounts of data expected from this instrument. This paper reviews the objectives of this ground data-processing system and presents the hardware implementation. An outline of the data flow through the system is given, and the software and incorporated algorithms developed specifically for the systematic processing of AVIRIS data are described.

1. INTRODUCTION

The Airborne Visible/Infrared Imaging Spectrometer (AVIRIS), the second in a series of imaging spectrometer instruments developed at JPL for Earth remote sensing,[1,2] has recently become operational. This instrument, flown aboard a U-2 aircraft, uses a scanner and four line arrays of detectors to image a 614-pixel swath simultaneously in 224 contiguous spectral bands (0.4 to 2.4 μm) with a ground instantaneous field of view (GIFOV) of 20 m. Ten-bit data are recorded onto 14-track high-density digital tape (HDDT) at a rate of 17 Mbit/sec, which is equivalent to 12 image lines per second. Data are written to the HDDT as a series of major frames. Each major frame contains one full-spectrum image line with associated navigation, engineering, and dark current data, as well as imbedded sync words, frame IDs, and frame counts. Record time is limited to 43 minutes by the HDDT's capacity of 5.5 Gbyte.

The need to process and archive the large volume of data generated by the AVIRIS instrument required the development of a dedicated ground data-processing system. This system, based on a VAX 11/780 minicomputer with the VMS operating system and running under the TAE/VICAR2 image processing executive, was developed and is currently operated within JPL's Image Processing Laboratory.

2. OBJECTIVES

The basic objectives of the AVIRIS ground data-processing system are to provide the following capabilities:

(1) Decommutate and archive AVIRIS data.

(2) Provide retrieval processing of archived AVIRIS data as requested by science investigators and apply appropriate radiometric and geometric rectification.

These two main processing steps, archival processing and retrieval processing, have further objectives that are more specific.

2.1 Archival processing

Archival processing is performed on all data recorded by the AVIRIS instrument. Specific archival processing requirements are as follows:

(1) Decommutate the HDDT data with playback on an Ampex HBR-3000 HDDT recorder and transfer the data directly to the host computer system.

(2) Segment the data stream into flight lines.

(3) Separate engineering, platform, calibration, and image data.

(4) Provide a scrolling video display of the image data from any one selected spectral band during the archival process for data quality assessment.

(5) Provide printouts and/or plots of engineering data to assess the health of the instrument.

(6) Generate an automated data base entry for record-keeping and data retrieval purposes.

(7) Generate black-and-white 8" x 10" photographic prints of the image data from four spectral bands (one band from each spectrometer). One print set with negatives is to be maintained as part of the archival records, while another set of prints is to be sent to the investigator(s) who requested specific flight lines.

(8) Generate archival CCT labels.

(9) Block the data as necessary to achieve an archival storage capacity of 512 full-spectrum image lines and associated auxiliary data per 6250-bpi 9-track CCT.

(10) Require no more than two weeks to archive one AVIRIS HDDT.

(11) Maintain printed records of all archived AVIRIS data.

2.2 Retrieval processing

Retrieval processing occurs when a request for data is received from a science investigator. Specific retrieval processing requirements are as follows:

(1) Provide the ability to locate data within the data base by geographic site name, latitude/longitude, or flight ID and run ID.

(2) Possess the capability to subset data in the band and/or line dimension.

(3) Conduct radiometric rectification to provide full-spectrum reconstruction accommodating spectral overlap between spectrometers, with dark current subtraction and resampling to correct for spectral readout time delays.

(4) Conduct geometric rectification to perform geometric warping to achieve correct pixel sizes and correct the relative spatial position of pixels.

(5) Block retrieved data and write them to 6250-bpi tape(s) for delivery to the investigator.

(6) Accomplish complete retrieval processing of one 10.5 km by 17.5 km full-spectrum scene (224 bands by 1024 lines by 614 samples) within two working days.

3. HARDWARE DESCRIPTION

A diagram of the AVIRIS ground data-processing system is shown in Figure 1. The system is based on a Digital Equipment Corporation (DEC) VAX 11/780 with 10 Mbytes of memory. The VAX is configured with three UNIBUS channels and one MASSBUS channel. Standard DEC peripherals include a console terminal, a line printer/plotter, two TU78 9-track 6250/1600-bpi tape drives, and six RA81 456-Mbyte disk drives. Additionally, a DEC LA100 printer is configured to print tape labels.

An Ampex HBR-3000 high-density tape drive is used to play back data recorded by the AVIRIS instrument onto HDDT. The HBR-3000 is interfaced to the VAX via a JPL-designed and -built controller interface, which in turn is connected to a DEC DRE11 alternate-buffered direct memory access (DMA) interface on one of the UNIBUS channels. The interface passes tape transport commands from the VAX to the HBR-3000 and passes data from the HBR-3000 to the VAX. Data leave the HBR-3000 as a serial bit stream. The JPL controller interface searches for and detects a specific 40-bit sync pattern imbedded in the data stream at the start of each major frame. It places each 10-bit data value following the sync pattern into the 10 least significant bits of a 16-bit word and passes the word to the DRE11, which then does a DMA transfer to the VAX. The DRE11 alternately accesses two separate 64K word areas within main memory. This allows one area to be processed while the other area is being filled, resulting in a virtually continuous data transfer.

The data system also has two Rastertech one/25 512 x 512 display devices and a Matrix QCR hardcopy film recorder with both Polaroid and 35mm capability. An OSI Laserdrive 1200 optical disk drive with Perceptics software has recently been installed, and an Interlan Ethernet controller connects the AVIRIS data system to several other systems on the Imaging Spectrometer Local Area Network (ISLAN) located at JPL.

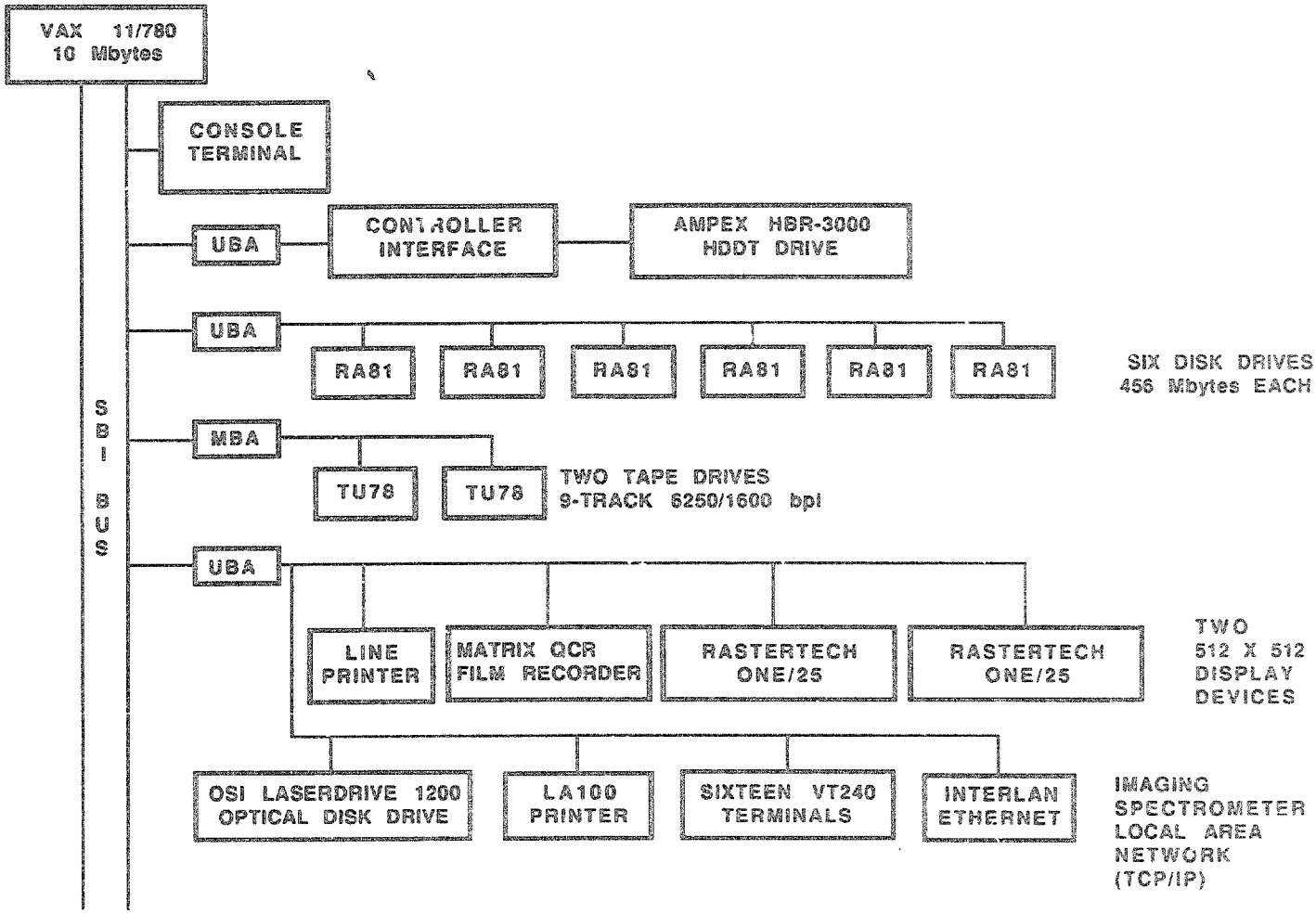

Figure 1. AVIRIS ground data-processing system.

4. OPERATION

Figure 2 shows the data flow through the AVIRIS ground data-processing system as it has been implemented. In this diagram, two subsidiary tasks, creation of an auxiliary input file and creation of the calibration file, have been shown in addition to the main archival and retrieval processing tasks.

4.1 Creation of the auxiliary file

The auxiliary file is a text file that provides the archival processing software with information not contained on the HDDT but necessary for a complete data base entry. The file is generated from the AVIRIS flight log and contains the following information for each flight line:

(1) Site name
(2) State (country for foreign flights)
(3) Principal investigator's name
(4) Principal investigator's affiliation
(5) Comments (cloud cover, visibility, etc.)

One auxiliary file is created using the editor for each HDDT and is used as a secondary input to the archival processing task.

4.2 Archival processing

Archival processing may be divided into three stages: decommutation, data reformatting, and data output. These three stages form a cycle that is repeated as data are processed in segments of 512 major frames at a time. This is the maximum amount of data stored on one archival CCT. Processing may be halted and restarted following the completion of a cycle. The time required to archive one segment is approximately 1.2

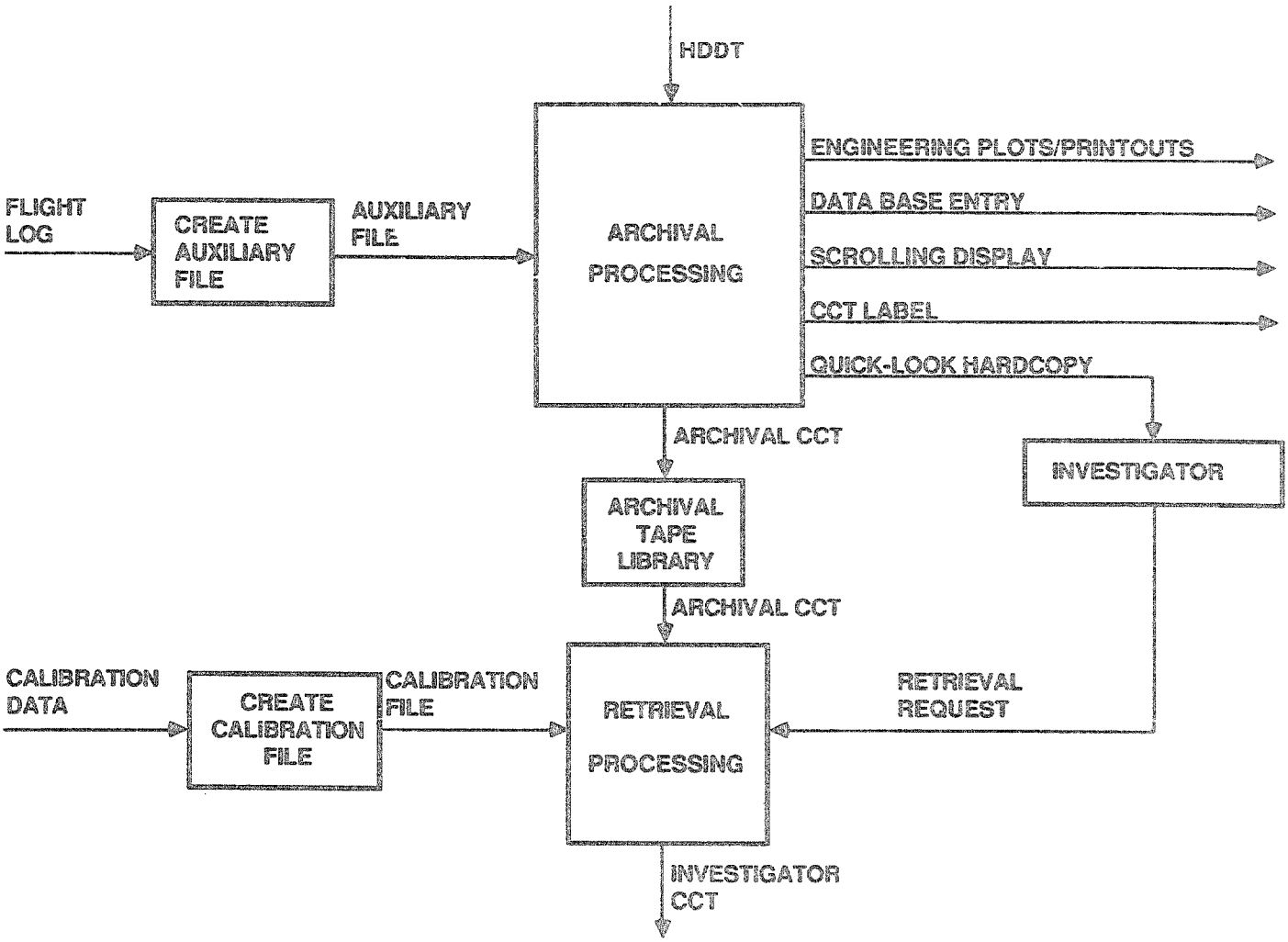

Figure 2. Data processing flow.

hours. Since a full HDDT contains 61 segments, the time required to archive a full HDDT is approximately 9 working days. Due to the real-time nature of the decommutation process, no other processing can be performed on the system during archival processing.

4.2.1 Decommutation. During decommutation, data are read into the VAX from the HBR-3000 and written directly onto magnetic disk, one major frame at a time. During this process the format of the major frame is verified and the major frame count is checked. Any corrupted or missing major frames are flagged with values of 4096. Playback of the HDDT on the HBR-3000 is done at 1/16 of the record speed, corresponding to a data rate of 1.06 Mbit/sec out of the HBR-3000 and, after the 10-bit to 16-bit conversion, 1.7 Mbit/sec into the VAX. Although the HBR-3000/VAX interface was run successfully at twice this speed, disk access/write times did not allow operation at this higher speed. Following decommutation of 512 major frames, the HBR-3000 tape transport is stopped and the HDDT is rewound slightly to position it for the next segment.

4.2.2 Data reformatting. Following decommutation, the data are read back from disk and reformatted. The data are separated into seven possible types: Pre-Cal, Navigation, Engineering, Dark Current, Offset, Image, and Post-Cal. Pre-Cal and Post-Cal data sets contain onboard calibration data taken immediately prior to and immediately following every flight line. Navigation and Engineering data are decoded from a bit-encoded format to INTEGER*4 and REAL*4 values. Image data are converted to a band interleaved by line organization and the pixels within each line are transposed to account for the scan mirror scanning from left to right. The center 512 samples of one spectral band are displayed on one of the Rastertech display devices in a scrolling manner as each line is processed. Histograms are calculated for each of the four spectral bands that are to be displayed in the quick-look hardcopy. Initial plans to simply use the eight high-order bits of each 10-bit pixel in producing the quick-look hardcopy did not result in images of acceptable quality.

4.2.3 Data output. At this point, samples of the data to be archived are output. The engineering data are printed and/or plotted. A linear auto-stretch with 1% saturation is performed separately on each of the four quick-look bands, converting them to byte data. These data are then sent to the QCR hardcopy device, exposing a 35mm negative. An example of a quick-look print is shown in Figure 3. A data base entry and a CCT label are generated using information from the data stream and the auxiliary file. Using this same information, VICAR annotation labels are generated which will be attached to the archived data sets. Finally, the data are written to the archival CCT as separate, blocked, and VICAR-labeled files.

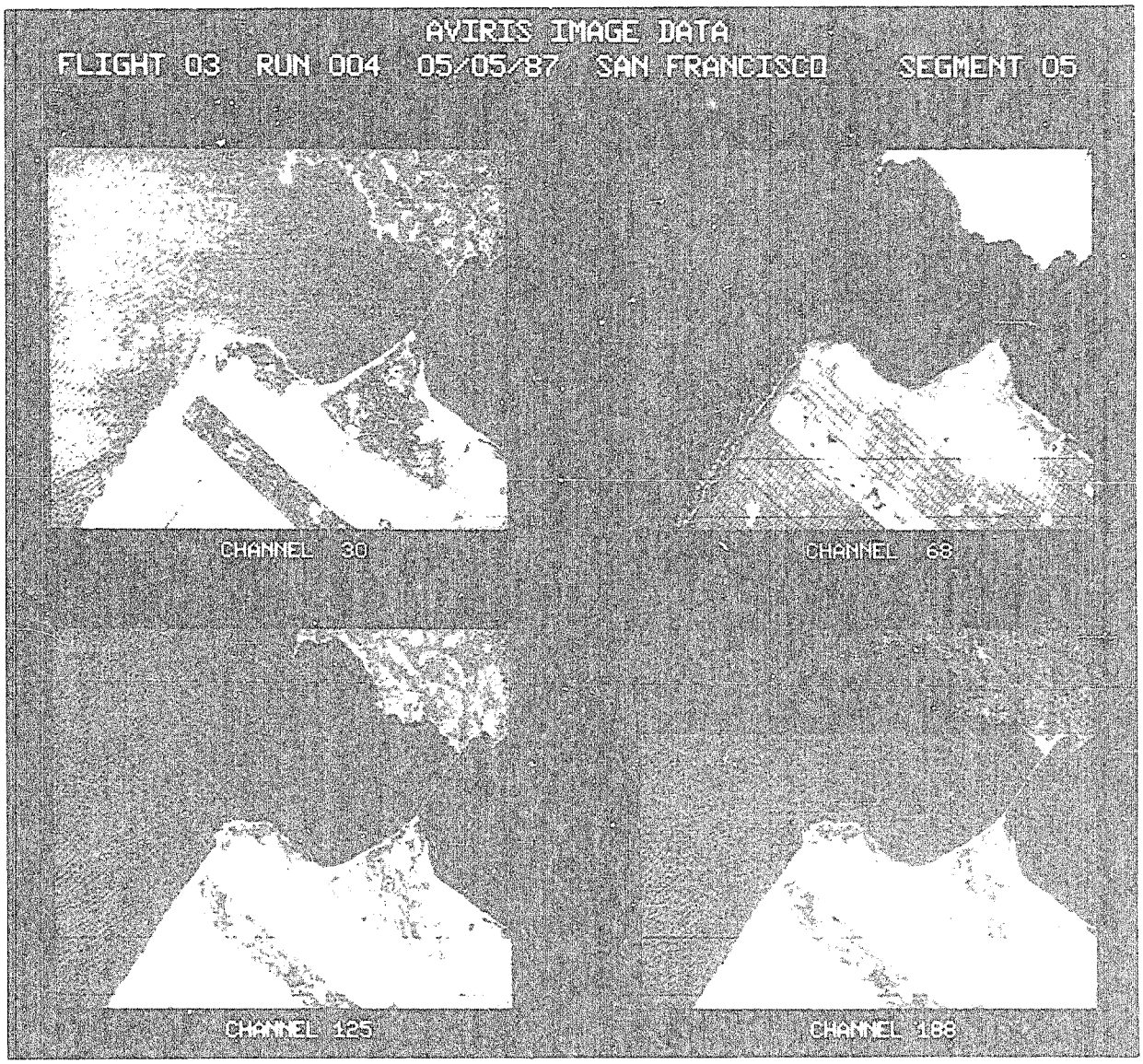

Figure 3. AVIRIS image data.

4.3 Creation of the calibration file

The calibration file, used in the radiometric rectification of AVIRIS data, is a set of REAL*4 multipliers used to convert AVIRIS DN values into radiance values in terms of $\mu W/cm^2$-nm-sr. The file is generated from laboratory calibration data taken prior to a flight season. These data consist of two components: radiance measurements of an integrating sphere light source taken by a spectroradiometer and data taken by the AVIRIS instrument while viewing the same integrating sphere. The AVIRIS laboratory calibration data are decommutated and archived in the same manner as flight data.

The calibration file is generated by first subtracting the dark current from the AVIRIS instrument data and then averaging these data over time as a function of spectral band (detector element) and cross-track sample number. A cross-track dependence is kept to account for nonuniform response with scan angle due to vignetting in the foreoptics of the

AVIRIS instrument. This results in a set of 224 x 614 mean DN values (224 spectral bands and 614 cross-track pixels). The 614 mean DN values of every spectral band are then associated with the corresponding radiance value for that spectral band, computed by resampling the spectroradiometer measurements to match the spectral spacing of the AVIRIS detector elements. Assuming detector linearity, the final set of multipliers is then computed as:

$$MULT(s,b) = RAD(b)/DN(s,b) \quad (1)$$

where s = the cross-track sample number and b = the spectral band number. This set of 224 x 614 multipliers is saved as the calibration file and used in the radiometric rectification of AVIRIS data taken during the flight season.

4.4 Retrieval processing

Retrieval processing is initiated by an investigator's request for AVIRIS data. The data are located, processed to the level desired by the investigator, and written to 6250-bpi CCT for delivery to the investigator. The time required to perform full retrieval processing on a full-spectrum 10.5 km by 17.5 km scene is approximately 2 working days. Since a full HDDT contains 30 scenes, full retrieval processing of an entire HDDT would require approximately 60 working days.

When a request for AVIRIS data is received, the first step in retrieval processing is to locate the desired data in the AVIRIS data base. This is a file-structured data base set up under DATATRIEVE. The AVIRIS data base contains information such as flight ID, run ID, flight date and time, site name, state or country of the site, site latitude and longitude, principal investigator's name and affiliation, name and location of the tape the data are stored on, and any comments noted during the recording of the data concerning instrument configuration and/or data quality. Software has been written which allows interactive interrogation of the data base. By specifying items such as flight ID, run ID, date, time, site, latitude/longitude, and/or investigator's name, information on any AVIRIS data an investigator might be interested in may be located, sorted, and printed.

After they are located, the desired data are subset to investigator specifications in the line and band dimensions, with the number of lines restricted to a maximum of 1024. The data are copied onto disk and, in the event that they span more than one archival CCT, the multiple data segments are concatenated together. Radiometric rectification and geometric rectification are then performed as requested and the data written to CCT for delivery to the appropriate investigator. Full retrieval processing of a 1024-line full-spectrum scene requires approximately 15 cpu hours.

4.4.1 Radiometric rectification. The radiometric rectification of AVIRIS data converts 10-bit DN values to REAL*4 radiance values in terms of $\mu W/cm^2$-nm-sr and linearly scales the values to 16-bit words. In the process, dark current subtraction, detector equalization, resampling to account for detector readout delays, and reconstruction of the full spectrum accounting for band overlap and varying spectral spacings between spectrometers are performed.

The first step in radiometric rectification processing is dark current subtraction. One dark current value for each detector element is recorded every major frame. Due to the presence of noise, dark current subtraction is done using a sliding mean of 101 dark current values as follows:

$$DN(s,b,l) = DN(s,b,l) - 1/101 \sum_{k=l-50}^{k=l+50} DC(b,k) \quad (2)$$

where s = the cross-track sample number, b = the spectral band number, l = the line number, and DC = the dark current.

The next step is detector equalization. Using the multipliers stored in the calibration file, DN values are converted to REAL*4 radiance values:

$$RAD(s,b,l) = DN(s,b,l)*MULT(s,b) \quad (3)$$

Resampling to correct for detector readout delays is then performed. These delays occur because the elements in the linear arrays are read sequentially. This results in the last element of an array (element #64) seeing a spot on the ground approximately one pixel further along the scan than was seen by the first element. Linear interpolation is performed between successive spatial pixels within a scan line as shown in Equation 4. As indicated by this formula and due to scan direction, time increases as the sample number decreases. The time between reading element #64 of an array and then reading element #1 of the same array (the next spatial pixel) is equivalent to reading two detector elements; thus the number 66 is used in Equation 4. Readout of the 32-element silicon array corresponds in time to readout of elements 1 through 32 within the three 64-element InSb arrays.

$$RAD'(s,b,l) = [(b'-1)/66]*RAD(s+1,b,l) + [(67-b')/66]*RAD(s,b,l) \quad (4)$$

where b' = the array element number of band b.

Following this, the full spectrum is reconstructed. Resampling is performed in the spectral direction to correct for band overlap between spectrometers and to create a spectrum with uniform spectral spacing. This step produces 210 bands from 0.4000 μm to 2.4482 μm with 9.8-nm spectral sampling. The center wavelengths of the AVIRIS detector elements are known from data taken in the spectral alignment procedure done in the laboratory. Ignoring detector element #1 from each linear array (unusable because of the readout architecture), each output band is computed by linearly interpolating between the two closest surrounding input bands:

$$RAD''(s,b,l) = \left(\frac{\lambda_b - \lambda_{b-}}{\lambda_{b+} - \lambda_{b-}} \right) [RAD'(s,b+,l) - RAD'(s,b-,l)] + RAD'(s,b-,l) \quad (5)$$

where b = the output band number, b- = the input band nearest to b with wavelength less than b, and b+ = the input band nearest to b with wavelength greater than b.

Finally, the REAL*4 radiance values are converted to 16-bit words by multiplying each radiance value by a factor of 100 and rounding to the nearest integer value. This is necessary for further processing by the geometric rectification and spectral analysis software and for the reduction of data storage requirements by a factor of two.

4.4.2 Geometric rectification. The geometric rectification of AVIRIS data involves geometric warping to correct for oversampling and for distortions caused by aircraft attitude variations. AVIRIS data is oversampled in both the cross-track and along-track directions in that the center-to-center spacing of 20-m pixels is 17.1 m. The pixels of AVIRIS images do not correspond to a rectangular array of imaged points on the ground because the aircraft is traveling forward during the time required to image successive pixels within a scan line and the aircraft is undergoing possible rotations (pitch, roll, and yaw) and possible variations in altitude and/or ground speed during image aquisition.

The first step in the geometric rectification process is to use a lookpoint model to map the input image onto a "reference plane," a horizontal coordinate plane located at sea level. One would like to map the image onto coordinates of a map of the surface; however, given some amount of terrain relief, some error in pixel location will occur. This is shown in Figure 4, where a pixel's line of sight is projected onto a sea-level plane and placed at point X, while the true pixel location on a map of the surface would place the position at X'. The coordinate system of the reference plane is arranged so that at some initial time t_0, $\hat{x}$ is to starboard, $\hat{y}$ is in the direction of aircraft travel, and $\hat{z}$ is oriented upwards; the aircraft's position is (0,0,h). (See Figure 5.)

To map a given pixel into a position on the reference plane, we assume that the following is known:

(1) t_p = time of pixel exposure
(2) $v(t)$ = horizontal velocity, known from t_o to t_p
(3) h = aircraft altitude at t_p
(4) ψ = aircraft yaw at t_p
(5) θ = aircraft pitch at t_p
(5) ϕ = aircraft roll at t_p
(7) η = angle of observation from aircraft nadir

We wish to compute the position (x,y) where a line from the aircraft at an angle η and time t_p intercepts the reference plane. The method used is to compute rotation matrices for yaw, pitch, and roll; apply the matrices to a unit vector at an angle η from the nadir of the aircraft; compute the intercept of the unit vector with the reference plane; and finally, translate the unit vector's intercept point by the amount the aircraft moved between t_o and t_p.

The aircraft's "body" coordinate system is defined as a right-handed orthonormal system, O_{RPY}, in which the origin, O, is at the aircraft center of gravity; the roll axis, $\hat{R}$, points in the forward direction; the pitch axis, $\hat{P}$, points to starboard; and the yaw axis, $\hat{Y}$, points down. (See Figure 6.) We first convert from coordinates (R,P,Y) in the O_{RPY} system to a coordinate system $O_{R_oP_oY_o}$, in which $\hat{R}_o$ is parallel to the $\hat{y}$ axis of the reference plane, $\hat{P}_o$ is parallel to the $\hat{x}$ axis of the reference plane, and the $\hat{Y}_o$ axis points in the $-\hat{z}$ direction. Yaw, pitch, and roll are defined so that one may convert from O_{RPY} to $O_{R_oP_oY_o}$ using the standard order of the angular rotations,[3] namely:

(1) Roll through $-\phi$ about the R axis
(2) Pitch through $-\theta$ about the new P axis
(3) Yaw through $-\psi$ about the Y_o axis

The rotation matrices to take O_{RPY} into $O_{R_oP_oY_o}$ are:

$$\lambda_\phi = \begin{bmatrix} 1 & 0 & 0 \\ 0 & \cos\phi & \sin\phi \\ 0 & -\sin\phi & \cos\phi \end{bmatrix}, \quad \text{(roll)} \tag{5a}$$

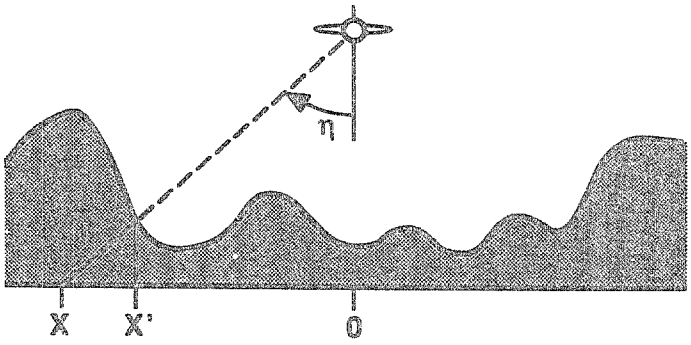

Figure 4. Pixel location error.

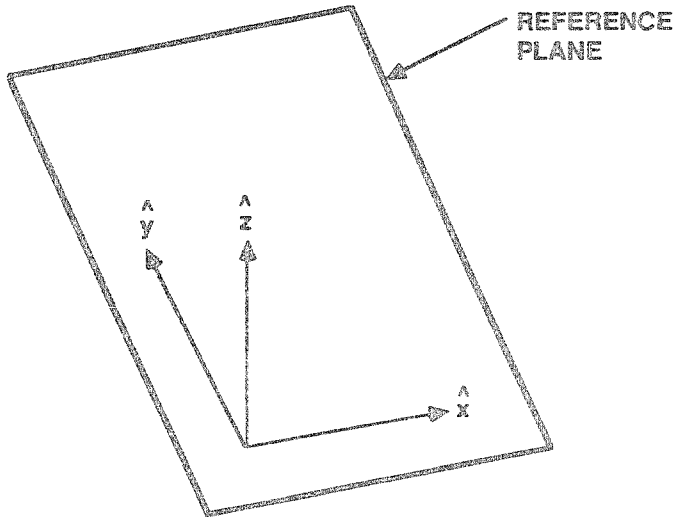

Figure 5. Reference plane coordinate system.

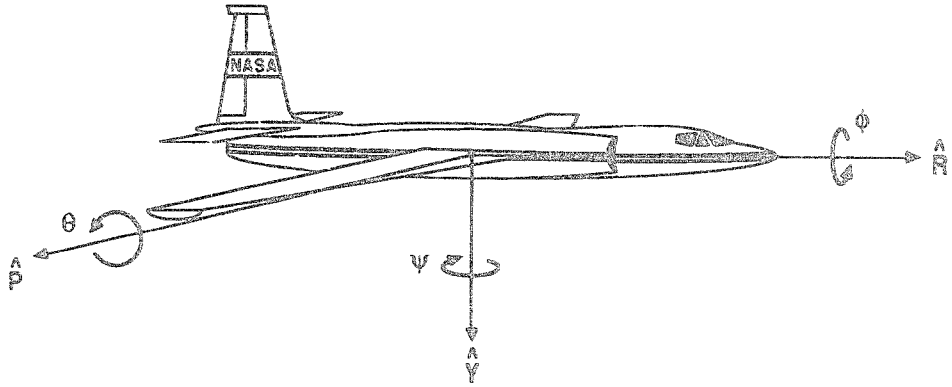

Figure 6. Aircraft coordinate system.

$$\lambda_\theta = \begin{bmatrix} \cos\theta & 0 & \sin\theta \\ 0 & 1 & 0 \\ -\sin\theta & 0 & \cos\theta \end{bmatrix}, \quad \text{(pitch)} \tag{6b}$$

$$\lambda_\psi = \begin{bmatrix} \cos\psi & \sin\psi & 0 \\ -\sin\psi & \cos\psi & 0 \\ 0 & 0 & 1 \end{bmatrix}, \quad \text{(yaw)} \tag{6c}$$

and the net rotation matrix to convert a vector in the O_{RPY} system into one in the $O_{R_oP_oY_o}$ system is:

$$\lambda_{b_o} = \lambda_\psi \lambda_\theta \lambda_\phi \tag{7}$$

In turn, a unit vector in the $O_{R_oP_oY_o}$ coordinate system may be expressed as a unit vector in the reference plane by first rotating 180 deg around the roll axis and then rotating 90 deg around the new yaw axis:

$$\lambda_r = \begin{bmatrix} 0 & 1 & 0 \\ 1 & 0 & 0 \\ 0 & 0 & -1 \end{bmatrix} \tag{8}$$

The total rotation matrix is thus:

$$\lambda_T = \lambda_r \lambda_{b_o} \tag{9a}$$

$$= \lambda_r \lambda_\psi \lambda_\theta \lambda_\phi \tag{9b}$$

$$= \begin{bmatrix} -\sin\psi\cos\theta & (\cos\phi\cos\psi + \sin\theta\sin\phi\sin\psi) & (\sin\phi\cos\psi - \sin\theta\cos\phi\sin\psi) \\ \cos\psi\cos\theta & (\sin\psi\cos\phi - \sin\theta\sin\phi\cos\psi) & (\sin\theta\cos\phi\cos\psi + \sin\phi\sin\psi) \\ \sin\theta & \sin\phi\cos\theta & -\cos\theta\cos\phi \end{bmatrix} \tag{9c}$$

Now let d' be a unit vector in the body frame that points at a pixel viewed at an angle η from the yaw axis $\hat{Y}$ in the plane perpendicular to the roll axis $\hat{R}$:

$$d' = \begin{bmatrix} 0 \\ -\sin\eta \\ \cos\eta \end{bmatrix} \tag{10}$$

In the coordinate system of the reference plane, this unit vector has the coordinates:

$$d = \lambda_T\, d' \tag{11a}$$

$$= \begin{bmatrix} -(\cos\theta\cos\psi + \sin\theta\sin\phi\sin\psi)\sin\eta + (\sin\phi\cos\psi - \sin\theta\cos\phi\sin\psi)\cos\eta \\ -(\sin\psi\cos\phi - \sin\theta\sin\phi\cos\psi)\sin\eta + (\sin\theta\cos\phi\cos\psi + \sin\phi\sin\psi)\cos\eta \\ -\sin\phi\cos\theta\sin\eta - \cos\theta\cos\phi\cos\eta \end{bmatrix} \tag{11b}$$

The intersection of the unit vector d with the reference plane can be conveniently computed when d is expressed in cylindrical coordinates: Define α to be the azimuth of the observation (measured CCW from the $\hat{x}$ axis of the reference plane), and let ρ be the angle of d away from the $-\hat{z}$ axis; $\rho = 0$ means that d is normal to the reference plane, while $\rho = \pi/2$ means that d is parallel to the reference plane. We have:

$$\rho = \pi - \cos^{-1} d_z \tag{12a}$$

$$\alpha = \tan^{-1}(d_y/d_x) \tag{12b}$$

The aircraft position at time t_p is:

$$x_a(t_p) = \int_{t_o}^{t_p} v_x(t)dv_x \tag{13a}$$

$$y_a(t_p) = \int_{t_o}^{t_p} v_y(t)dv_y \tag{13b}$$

The intercept of the line of sight from the aircraft with the reference plane is then obtained from Equations 12 and 13:

$$x = x_a + h \tan\rho \cos\alpha \tag{14a}$$

$$y = y_a + h \tan\rho \sin\alpha \tag{14b}$$

Using this procedure and the navigation data from the U-2 aircraft, an array of control points is generated mapping the image onto the reference plane. These control points are spaced approximately every 100 lines and 100 samples in the input image.

The next step is to resample these control points to obtain a regularly spaced array of points in the reference plane. This is required by the geometric warping algorithm to be used. The algorithm employed in resampling the control points is called "triangularization".[4] It connects all the points into an optimal surface formulated by searching for the shortest line segment that does not cross existing line segments. The search is applied exhaustively (i.e., for all points) by computing the vector distances from a given point to all points and sorting the distance list. Once the connections are configured, each triangle mapping (geometric transformation) is computed as:

$$\begin{bmatrix} x_1 & x_2 & x_3 \\ y_1 & y_2 & y_3 \end{bmatrix} = A \begin{bmatrix} x'_1 & x'_2 & x'_3 \\ y'_1 & y'_2 & y'_3 \end{bmatrix} + C \tag{15}$$

where

$$A = \begin{bmatrix} a_{11} & a_{12} \\ a_{21} & a_{22} \end{bmatrix}$$

$$C = \begin{bmatrix} c_1 & c_1 & c_1 \\ c_2 & c_2 & c_2 \end{bmatrix}$$

After the transformation coefficients are generated for every triangle, the program creates a regular grid. For each grid point, it determines which triangle the grid point is in and then applies the appropriate triangle transformation to compute the corresponding input grid point:

$$\begin{bmatrix} x' \\ y' \end{bmatrix} = A_i \begin{bmatrix} x \\ y \end{bmatrix} + C_i \qquad (16)$$

where i denotes the triangle within which grid point (x,y) is located.

Finally, the actual geometric warping of the image data is perfomed using the resampled control points. The software that performs this function is written to operate on data with three dimensions: lines, samples, and bands. It assumes that all bands are co-registered. The geometric warping process consists of pixel location mapping using the input control points (shown by Figure 7 and Equations 17a and 17b) and pixel intensity mapping (bilinear interpolation shown in Equation 18). Since the location mapping process is a function of the line and sample only, the location map can be shared over the third dimension, the band dimension. This sharing of the location map across the third dimension enhances the computation speed greatly.

$$s' = a1 + (s-x1)*DS1 + (l-y1)*DS2 + (l-y1)*(s-x1)*DSL \qquad (17a)$$

$$l' = b1 + (s-x1)*DL1 + (l-y1)*DL2 + (l-y1)*(s-x1)*DLS \qquad (17b)$$

where

$$DS1 = (a2-a1)/(x2-x1)$$
$$DL1 = (b2-b1)/(x2-x1)$$
$$DS2 = (a3-a1)/(y3-y1)$$
$$DL2 = (b3-b1)/(y3-y1)$$
$$DLS = [(b4-b3)-(b2-b1)]/[(x2-x1)(y3-y1)]$$
$$DSL = [(a4-a3)-(a2-a1)]/[(x2-x1)(y3-y1)]$$

$$\text{Pixel intensity } p(s,l) = P1 + (l'-il')*(P2-P1) \qquad (18)$$

where

$$P1 = p'(is',il') + (s'-is')*[p'(is'+1,il')-p'(is',il')]$$
$$P2 = p'(is',il'+1) + (s'-is')*[p'(is'+1,il'+1)-p'(is',il'+1)]$$
$$il' = INT(l')$$
$$is' = INT(s')$$

and the function INT() denotes real-to-integer conversion with truncation.

Geometric warping is performed by first reading in a grid row of the regularly spaced control points. The minimum and maximum input line numbers are computed and the corresponding portion of the input image is read into memory (see Figure 8). (This algorithm assumes that the geometric distortion does not have a large degree of rotation.) For each grid, geometric transform coefficients are computed using Equations 17a and 17b. The portion of the output image corresponding to this grid row is then constructed using the bilinear intensity interpolation (Equation 18) one line at a time for all bands. Following this, the next grid row is read and the process repeats until all grid rows have been processed. Pixels in the output image that map outside of the input image are set to zero.

5. FUTURE PLANS

Future plans for the AVIRIS ground data-processing system include the acquisition of a 1024 by 1024 International Imaging Systems IVAS display device. This will allow viewing of a full swath-width AVIRIS image. The possibility of archiving AVIRIS data on optical disk, rather than on CCT, is being investigated. The advantages to archiving the data on optical disk are a large reduction in physical storage space, increased media reliability and lifetime, and a reduced requirement for operator intervention. The disadvantages are increased media costs and slower read/write speeds. Finally, it is envisioned that sometime in the future the operation of both the AVIRIS instrument and the ground data-processing system will be shifted to Ames Research Center.

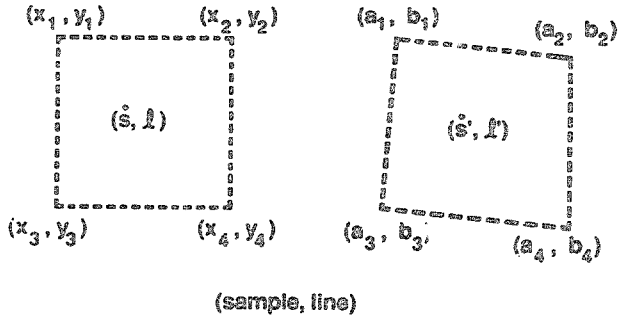

Figure 7. Location mapping.

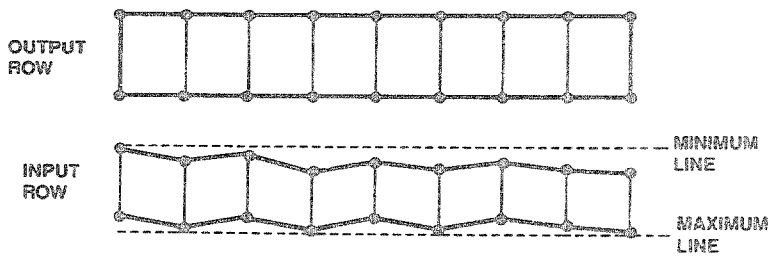

Figure 8. Grid row of control points.

6. REFERENCES

1. G. Vane, A. F. G. Goetz, and J. B. Wellman, "Airborne Imaging Spectrometer: A new tool for remote sensing," IEEE Transactions on Geoscience and Remote Sensing, Vol. GE-22, No. 6, pp. 546-549 (1984).

2. G. Vane, M. Chrisp, H. Enmark, S. Macenka, and J. Solomon, "Airborne Visible/ Infrared Imaging Spectrometer (AVIRIS): An advanced tool for earth remote sensing," Proceedings of the 1984 IEEE International Geoscience and Remote Sensing Symposium, Publication No. SP215, European Space Agency, Paris, pp. 751-757 (1984).

3. A. W. Babister, Aircraft Stability and Control, Pergamon Press, N.Y. (1961).

4. G. K. Manacher and A. L. Zobrist, "A fast, space-efficient average-case algorithm for the greedy triangulation of a point set," SIAM Journal on Computing (submitted).

7. ACKNOWLEDGMENT

The research described in this paper was carried out by the Jet Propulsion Laboratory, California Institute of Technology, under a contract with the National Aeronautics and Space Administration.

Spectral and radiometric calibration of the Airborne Visible/Infrared Imaging Spectrometer

Gregg Vane, Thomas G. Chrien, Edward A. Miller, John H. Reimer

Jet Propulsion Laboratory, California Institute of Technology
4800 Oak Grove Drive, Pasadena, California 91109

ABSTRACT

The laboratory spectral and radiometric calibration of the Airborne Visible/Infrared Imaging Spectrometer (AVIRIS) used in the radiometric calibration of all AVIRIS science data collected in 1987 is described. The instrumentation and procedures used in the calibration are discussed and the calibration accuracy achieved in the laboratory as determined by measurement and calculation is compared with the calibration requirements. Instrument performance factors affecting radiometry are described. The paper concludes with a discussion of future plans.

1.0 INTRODUCTION

AVIRIS is a second-generation imaging spectrometer developed at the Jet Propulsion Laboratory for use in earth remote sensing studies across a broad spectrum of scientific disciplines, including botany, geology, hydrology and oceanography.[1] Construction and calibration of the sensor was completed in June 1987. Data were collected for 20 investigators between June and October 1987. The calibration described in this paper was the one used to radiometrically calibrate all AVIRIS science data collected in 1987.

AVIRIS acquires images in 220 contiguous 10-nanometer (nm) spectral bands in the region between 0.40 and 2.45 micrometers (μm). The instantaneous field of view of AVIRIS is 1 milliradian and the field of view as defined by the scan angle is 30 degrees. This results in images covering a 10.5 km swath composed of picture elements (pixels) which subtend 20 m on the ground from the 20 km altitude of the NASA U-2. AVIRIS gathers spectral images in the whisk-broom imaging mode, employing foreoptics with a scan mirror which scans in one direction, then rapidly returns to the start position for the next scan line. The scan rate and detector readout timing were designed to provide a 17 percent spatial oversampling at sea level in both the cross-track and along-track dimensions. This results in the acquisition of 614 pixels in each scan line. Geometric rectification removes the oversampling, resulting in an image 550 pixels across. Twelve scans are completed per second. During the fly-back portion of the scan cycle, a shutter closes the foreoptics from the rest of the optical system while a detector dark current measurement is made.

The foreoptics are connected to four spectrometers with optical fibers. Spectrometer A contains a 32-element line array of silicon detectors and spectrometers B, C, and D each employ 64-element line arrays of indium antimonide detectors. While a total of 224 spectral bands are actually acquired, the readout architecture of the detector arrays renders the first band of each array unuseable; there are thus 220 useable raw spectral bands. The useable spectral ranges of spectrometers A, B, C, and D are 0.40 to 0.71, 0.68 to 1.28, 1.24 to 1.86, and 1.83 to 2.45 μm, respectively, as currently aligned. During radiometric calibration the spectral region covered by the 220 raw spectral bands is resampled to remove overlap between spectrometers and equalize the spectral sampling interval across the entire 0.40 to 2.45 μm region. This results in 210 spectral bands over this region in the radiometrically corrected data.

Each spectrometer additionally receives input via a second optical fiber from an onboard calibration source consisting of a tungsten lamp, a four-position filter wheel containing two neutral density filters, a didymium oxide filter and an opaque position. The neutral density filters provide broad-spectral-band energy at two intensity levels to monitor radiometric stability. The didymium oxide filter provides several spectral absorption features throughout each of the spectral regions of the four AVIRIS spectrometers to monitor spectral calibration. The opaque position is used in conjunction with the shutter in the foreoptics to provide a measurement of dark current. Complete details of the sensor can be found in the papers in these Proceedings.[2]

Work with the predecessor to AVIRIS, the Airborne Imaging Spectrometer (AIS), which was an engineering test bed sensor for infrared area detector arrays, has shown clearly the power of imaging spectroscopy as a tool for studying the earth.[3,4] The ability to acquire a complete, high resolution spectrum for each pixel in the scene has made possible from an airborne platform the direct identification of minerals and the assessment of the health and biochemical composition of plants. The data also contain spectral features arising from CO_2 and water vapor in the atmosphere; such data are of use in compensating for atmospheric absorption. To derive the maximum information from such data, however, it is critical that the instrument be well-calibrated spectrally and radiometrically. Work with AIS and with laboratory and field spectroradiometers[5,6] provided guidance in establishing the calibration requirements for AVIRIS, which are summarized in Table 1. Table 1 also includes the achieved calibration performance as determined through measurement and calculation.

Table 1. Spectral and Radiometric Calibration Requirements and Achieved Performance

Parameter	Required	Achieved
Spectral Calibration	5 nm	2.1 nm
Absolute Radiometry	10%	7.3%
Band-to-Band Radiometry	0.5%	0.4%

The requirement for spectral calibration derives from the need to accurately determine the wavelength positions of diagnostic spectral features in earth surface materials. The requirement for relative radiometric calibration, as defined by the spectral band-to-band calibration required to remove the effects of the non-uniformity of response of the detectors, derives from the need to accurately assess the relative strengths of spectral features. The requirement for absolute radiometric calibration was driven by the desire to be able to compare multitemporal data sets of dynamic earth surface materials such as plants and water to assess changes in reflectance over time, and by the need in some applications to determine the absolute magnitudes of various spectral features. Also, theoretical models of atmospheric scattering and absorption require absolutely calibrated data for their successful interpretation.

In the course of calibrating AVIRIS in the laboratory prior to the 1987 flight season, all of the calibration requirements were met. In the following pages, we discuss the details of the procedures used and summarize the results of each step of the calibration.

2.0 SPECTRAL CALIBRATION

The purpose of the spectral calibration of AVIRIS is threefold: (1) To map the wavelength distribution of light falling on the detector elements to within 5 nm, (2) to determine the wavelength bandwidth falling on each detector element, and (3) to determine the spectral sampling interval of each spectrometer as defined by the spacing between the center wavelengths of each spectral band. The steps in performing this work are: (1) Calibrating a laboratory monochromator, (2) aligning the monochromator with AVIRIS, and (3) recording the scan of a narrow spectral bandwidth of light from the monochromator across the AVIRIS detectors.

2.1 Monochromator calibration

A Jarrell-Ash model 82-487 laboratory monochromator is used in the spectral calibration of AVIRIS. By choosing the widths of the entrance and exit slits, the spectral bandwidth of the monochromator can be tailored as desired. In order to cover the full wavelength range of AVIRIS, three gratings are alternately employed. Wavelength output of the laboratory monochromator is controlled by the angular position of the grating, which is provided by a worm and gear drive attached to a position counter.

Calibration of the monochromator is performed with a mercury pen lamp, using multiple orders of the emission line at 546.1 nm. A plot of the monochromator counter reading as a function of order times 546.1 nm is used to determine the relationship between the counter reading and wavelength. Figure 1 shows such a plot for the monochromator. The circles on the plot represent the observed counter

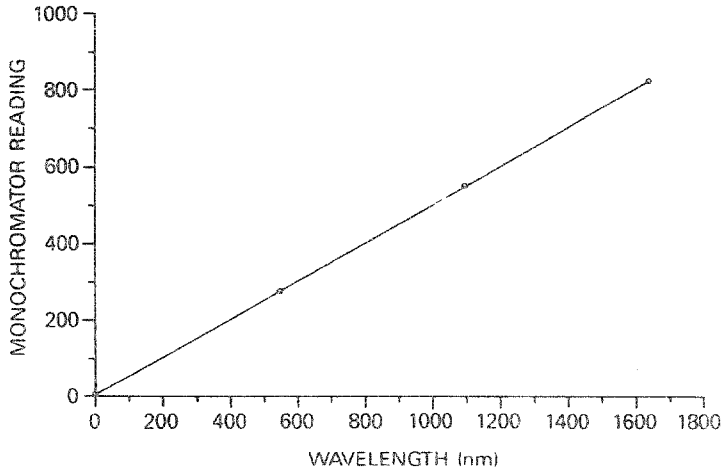

Figure 1. Plot of monochromator reading as a function of wavelength. The straight line is a least squares fit to the multiple orders of the 546.1 nm mercury line.

readings for zero, first, second, and third orders of the mercury emission line. The straight line connecting the circles is a least squares linear fit to the data. The fit line passes within 1 nm of each data point. The slope and y intercept of the plot are used to determine the calibration factor necessary to convert the counter number to the output wavelength. In calibrating AVIRIS for the 1987 flight season, the monochromator counter reading was taken to be a linear function of output wavelength. The error inherent in making this assumption is included in the calibration error budget.

2.2 AVIRIS spectral calibration procedure

The linearity of spectral dispersion of each AVIRIS spectrometer is determined before it is integrated with the AVIRIS foreoptics. The output of the monochromator is focussed onto a test optical fiber similar to the one connecting the spectrometer and foreoptics, filling the full numerical aperture of the fiber. The wavelength of the monochromator is scanned at a spectral bandwidth of 1 nm. The monochromator counter reading is noted at the peak signal level from each detector element as measured on an oscilloscope. The counter reading is then converted to wavelength and plotted against the spectral band number. A least squares fit of the center wavelength versus the spectral band number is performed on the data and the deviation of each point from that fit is measured. A plot of wavelength versus spectral band number for the first spectrometer in AVIRIS is shown in Figure 2a. Figure 2b shows a plot of the deviation of each spectral band from the least squares fit. Similar plots were made for the other three AVIRIS spectrometers. The standard deviation of the departure from the least squares fit was 0.71, 0.60, 0.58, and 1.84 nm for spectrometers A, B, C, and D, respectively.

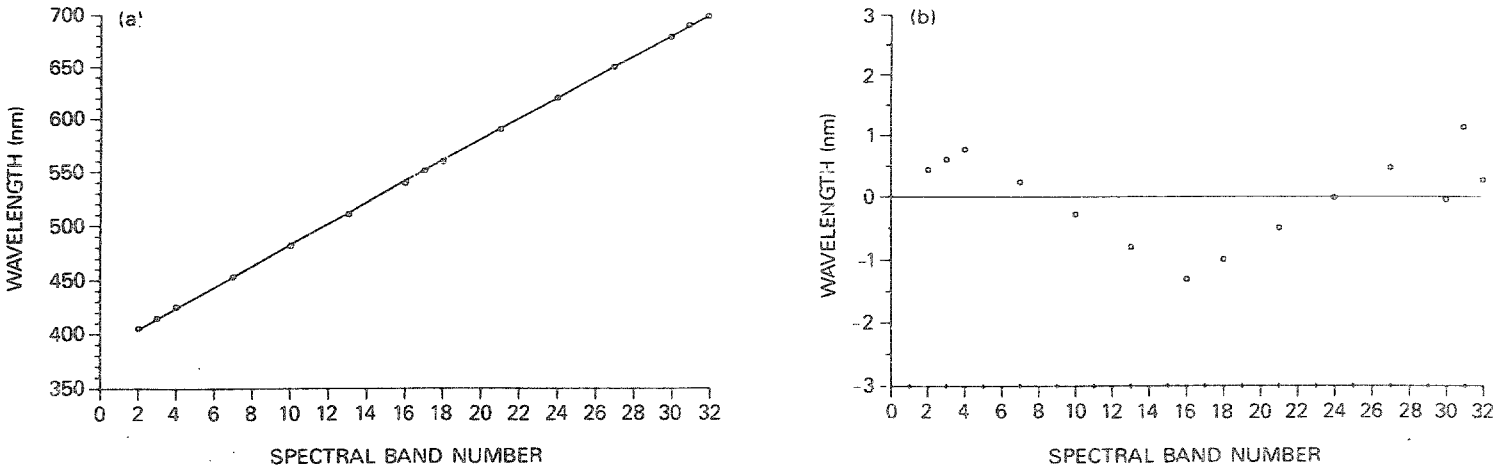

Figure 2. (a) Wavelength versus spectral band number for spectrometer A. The straight line is a least squares fit to the measured data. (b) Deviation of the wavelength position of each spectral band versus the least squares fit.

The laboratory setup for performing the spectral calibration of AVIRIS is shown schematically in Figure 3. The calibration is performed after the spectrometers have been integrated with the foreoptics. A tungsten light source is imaged onto the entrance slit of the monochromator. The exit slit of the monochromator is placed at the focus of a 40 inch effective focal length Space Optics Research Lab (SORL) 8 inch aperture collimator. The collimator is centered and aligned so that the full aperture of the AVIRIS foreoptics is filled. In this arrangement, AVIRIS is suspended on a gantry above the collimator. Several spectral bands are chosen for each spectrometer to give a representative sample at the ends and middle of the spectral ranges of the spectrometers. For a given AVIRIS detector element, monochromatic light of 1 nm bandwidth at increasing wavelength is put into the instrument and the output signal level from that spectral band is recorded as a function of monochromator wavelength, using the AVIRIS ground support computer. A typical plot from spectral band 9, Spectrometer A, is shown in Figure 4. Analysis of this plot shows that the peak signal occurs at 475 nm, which is taken as the center wavelength of the spectral band defined by that detector element. The full spectral width at half the maximum signal from the plot is 9.6 nm, which is taken to be the wavelength bandwidth of AVIRIS spectral band 9.

The spectral sampling interval, which is defined as the spacing between the center wavelengths of the individual spectral bands, is determined by fitting a straight line to the several spectral bands mapped in each spectrometer according to the method outlined above. The slope of this line is the spectral sampling interval and is used to extrapolate the center wavelengths of the remaining spectral bands in the spectrometer. This approach is employed rather than individually mapping each spectral band because the dispersion of each spectrometer is linear to at least 1.84 nm over its spectral range. The small error resulting from using this assumption is incorporated into the spectral calibration error budget.

2.3 Results of the spectral calibration

Table 2 summarizes the average spectral bandwidth, the spectral sampling interval, the standard deviation of the linearity measurement, the monochromator calibration accuracy, and the AVIRIS spectral calibration accuracy for each spectrometer. The average bandwidth was

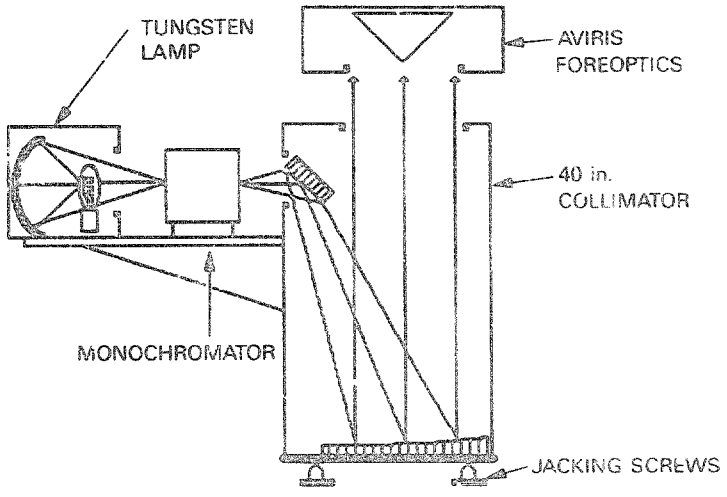

Figure 3. Laboratory setup used in performing the spectral calibration of AVIRIS.

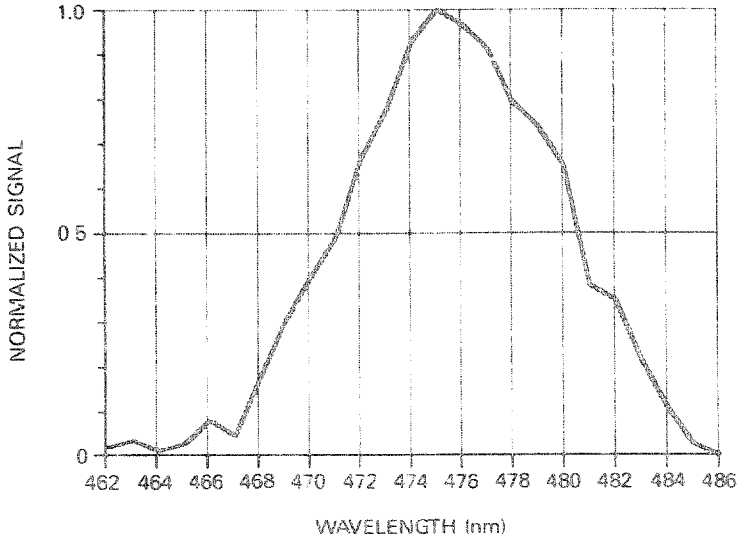

Figure 4. Spectral response curve for spectral band 9 in spectrometer A.

calculated by averaging the several spectral bandwidths measured in each spectrometer using the narrow band monochromatic light scan technique described earlier. The spectral sampling interval was calculated from the slope of the line passing through those data. The standard deviation of the linearity measurement represents the magnitude of the error introduced by assuming linear dispersion. The monochromator calibration accuracy was measured by performing multiple calibrations with the mercury emission line source and noting the repeatability. The AVIRIS spectral calibration accuracy was then calculated by combining the latter two quantities in Table 2, derived from measurements in a root sum square fashion. The resulting spectral calibration accuracies exceed the requirements.

Table 2. AVIRIS Spectral Calibration

Parameter (in units of nm)	Spectrometer			
	A	B	C	D
Average Bandwidth (FWHM)	9.7	9.7	9.0	11.6
Spectral Sampling Interval	10.0	9.58	9.86	9.85
Std. Dev. of Linearity Measurement	0.71	0.60	0.58	1.84
Monochromator Calibration Uncertainty	0.5	0.5	0.5	1.0
AVIRIS Spectral Calibration Accuracy	0.9	0.8	0.8	2.1

3.0 RADIOMETRIC CALIBRATION

Radiometric calibration of AVIRIS involves four steps. The first is the calibration of a spectroradiometer against a standard lamp traceable to a National Bureau of Standards (NBS) lamp. The second step is the calibration of the AVIRIS radiance source, a 40-inch-diameter integrating sphere, with the spectroradiometer. Third is the acquisition with AVIRIS of a file of digital numbers (DNs) of the integrating sphere output. Finally, using the spectral calibration, the light transfer curves (radiance versus wavelength) from the integrating sphere, and the DN output acquired with AVIRIS of the sphere, a table of multipliers is constructed which is the calibration file that is applied to all subsequent AVIRIS data to convert the raw instrument DN to radiance. Each of the steps involved in the construction of the calibration file has an error budget associated with it which determines the absolute and relative radiometric calibration accuracies achievable. In the remainder of this section, we describe the steps leading up to the application of the calibration file to the AVIRIS data. In the next section of the paper, we present an analysis of the radiometric calibration accuracy.

3.1 Calibration of the spectroradiometer

An Optronics Laboratories model 746 spectroradiometer system is used for radiometric calibration of the AVIRIS integrating sphere. The spectroradiometer is equipped with a silicon detector for use in the 0.4 to 1.1 μm region and a lead sulfide detector with a thermal electric cooler for use over the 0.9 to 2.5 μm region. The system also includes a monochromator with an integrated chopper, a matched set of gratings and filters, a digital grating drive controller, a detector preamplifier, and a lock-in radiometer. In addition, a 2 inch diameter telescope with a 1.5 degree field of view is used to measure a portion of the integrating sphere surface area comparable to that viewed by AVIRIS. Calibration of the spectroradiometer is done with the telescope in place. During calibration, the entire system is controlled using an MS-DOS compatible computer which automates the processing of data collection and recording. The computer is also used for data reduction.

The laboratory setup used is shown in Figure 5. The spectroradiometer system is positioned on a computer-controlled rotating stage to alternately view a freshly prepared 6 inch square pressed halon target at a 45 degree angle normal to its surface, and the AVIRIS integrating sphere. The pressed halon target is used to calibrate the spectroradiometer in units of radiance. A new halon target is made prior to each calibration using the procedure described by Weidner and Hsia.[7] Placed between the halon target and the spectroradiometer are baffles designed and positioned to eliminate stray light from entering the spectroradiometer optics. The halon target is illuminated with a tungsten lamp calibrated as a standard of irradiance by Optronics Laboratories against an NBS-calibrated lamp. The calibrated tungsten lamp is powered by an Optronics calibrated constant-current power supply.

A file of spectral radiance values for the standard lamp-halon target-spectroradiometer configuration is calculated using the expression

$$L(\lambda) = \frac{I(\lambda) \cos 45° R(\lambda)(50\ \text{cm})^2}{\pi(D\ \text{cm})^2} \quad (1)$$

where $L(\lambda)$ is the radiance viewed by the spectroradiometer, $I(\lambda)$ is the irradiance of the calibrated lamp as provided by the manufacturer, $R(\lambda)$ is the reflectance of the halon target[7], 50 cm is the distance at which the lamp was calibrated, and D is the distance between the spectroradiometer and the halon target. DNs are collected with the spectroradiometer at the AVIRIS spectral sampling interval by viewing the halon target illuminated by the standard lamp. A calibration file consisting of a set of multipliers is generated which adjusts the DN output of the spectroradiometer at each wavelength to match the corresponding spectral radiance of the illuminated halon target. This file is applied to all subsequent measurements made with the spectroradiometer to correct its DN output to absolute radiance.

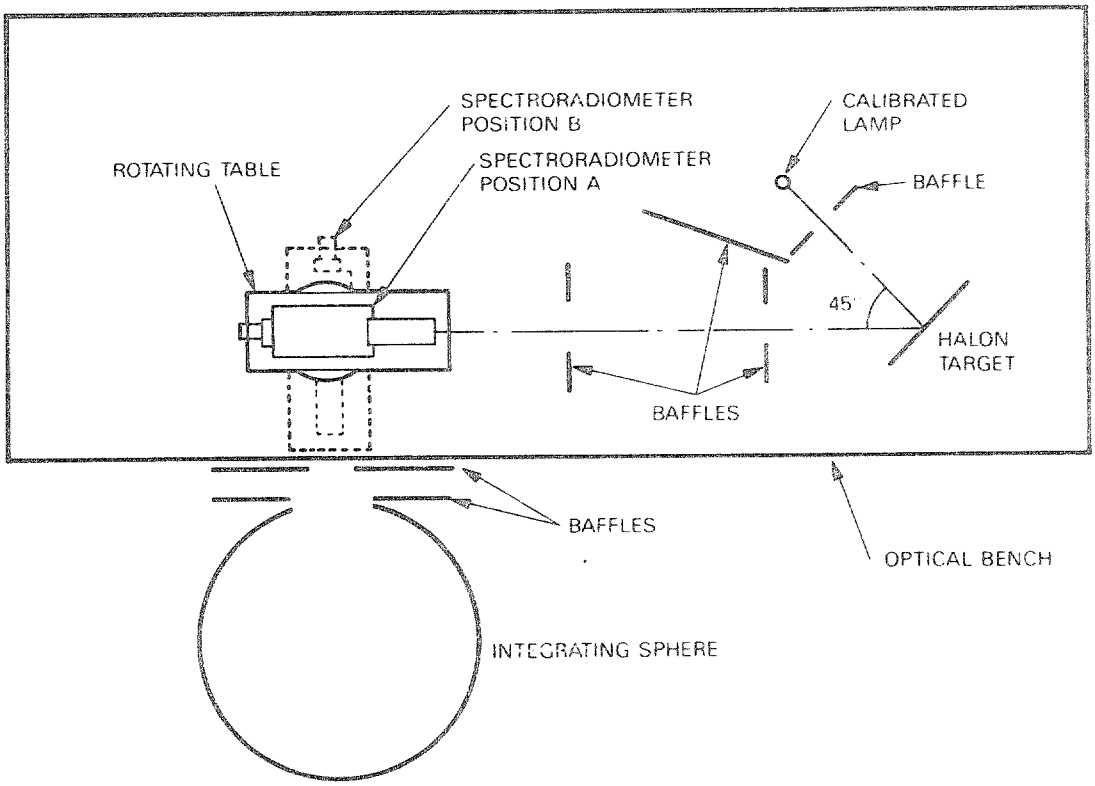

Figure 5. Laboratory setup used in calibrating the AVIRIS spectroradiometer and integrating sphere. All components except the integrating sphere are bolted to an optical bench.

3.2 Calibration of the integrating sphere

The radiance source used in the radiometric calibration of AVIRIS is a 40 inch diameter spun aluminum integrating sphere, built by Labsphere Incorporated, with a 16 inch diameter aperture. The interior of the sphere is coated with barium sulfate and is illuminated with four tungsten/halogen 500 watt lamps. The lamps are mounted external to the sphere and cooled with a double ventilating system having a forced-air input and an additional exhaust fan. Each lamp housing and cooling system is isolated from the interior of the sphere by an 8-inch-diameter water-free quartz diffuser. Outside the sphere, between the diffuser and each lamp, is located an aluminum aperture wheel with five sets of holes giving five intensity levels per lamp. The intensity level nomenclature is level A for highest intensity and level E for lowest. The four lamp/aperture wheel combinations can be combined to provide a wide range of light intensities within the sphere. A common setting used during AVIRIS calibration is EEEE, which corresponds to each lamp set at the smallest, or E, aperture. The lamps are powered with an Electronics Measurements Corp. current- and voltage-regulated power supply.

Two criteria are essential for the integrating sphere to be an adequate stimulus for calibrating AVIRIS. First, the radiance must be uniform across the entire 16 inch aperture. The aperture size was chosen to overfill the AVIRIS field of view by 25 percent at the recommended viewing distance of 12 inches from the plane of the aperture.[8] Second, the output of the sphere should be constant with time. Uniformity of radiance across the aperture was measured as a function of angle and as a function of position across the aperture by the manufacturer using a narrow field of view photometer, and at JPL using the Optronics spectroradiometer. The radiance output was found to be uniform to within 1 percent across the aperture for all lamp settings except those using less than all four lamps. The worst case was for illumination with only one lamp; a 2.3 percent loss of radiance was found at the outer 2 inches of the aperture opposite the lamp. This setting is not used in radiometric calibration of AVIRIS. Constancy of output of the sphere was measured by calibrating the sphere 20 consecutive times over a period of four hours, which is approximately the time required to complete an AVIRIS calibration. The radiance output was observed to be constant to within 1.1 percent.

The setup for performing the radiometric calibration of the integrating sphere is shown in Figure 5. After the spectroradiometer has been calibrated against the illuminated halon target, the rotating table is commanded to move the spectroradiometer to a viewing position normal to the plane of the 16 inch aperture. The sphere and spectroradiometer are arranged so that the spectroradiometer views the center of the aperture at a distance of 12 inches from the aperture, duplicating the viewing geometry used in calibrating AVIRIS. Large flat baffles painted Cadillac™ black are used to minimize stray light reflected between the sphere and AVIRIS. These baffles are used in the same relative positions when viewing the sphere with the spectroradiometer. After a 30 minute warm-up period, the spectroradiometer acquires data from the integrating sphere. These raw DNs are converted to radiance as described above. The results of a typical calibration of the AVIRIS integrating sphere are shown in Figure 6. This is one of the light transfer curves in radiance versus spectral band number subsequently used to convert AVIRIS DNs to radiance.

3.3 Calibration of AVIRIS

AVIRIS, the integrating sphere, and the spectroradiometer are all located in the same laboratory, which is temperature and humidity stabilized. After the sphere has been calibrated, it is moved into position beneath AVIRIS, which is suspended from a gantry. Placed between AVIRIS and the integrating sphere is the hatch window from the U-2. The distance of the window from the AVIRIS scan mirror

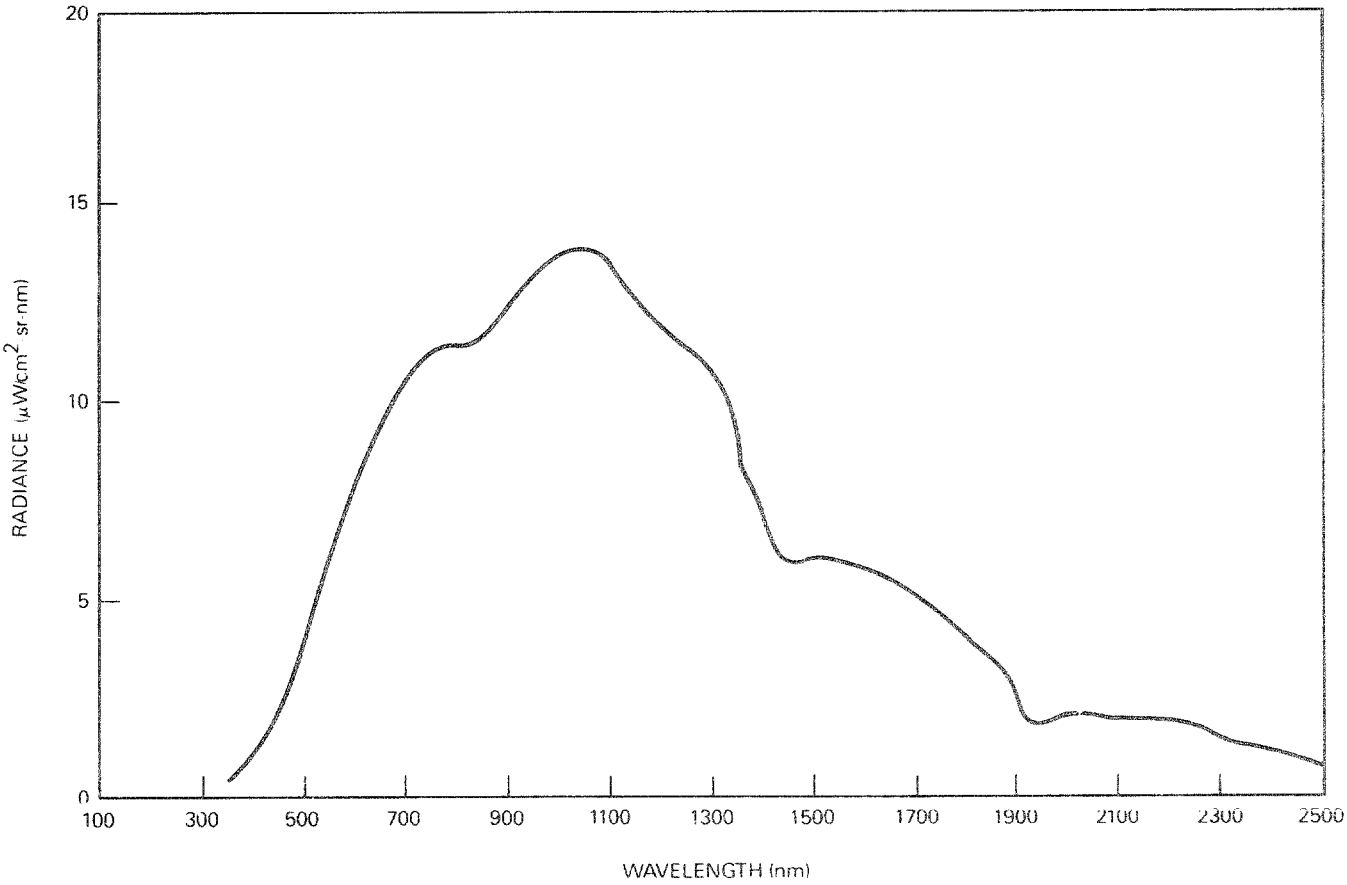

Figure 6. Typical light transfer curve from the AVIRIS integrating sphere at the lowest four-lamp output level (setting EEEE).

is the same as in the airplane. Following the same warm-up procedure used in calibrating the sphere, AVIRIS data are acquired from the sphere at several aperture settings over several hours. During an initial calibration of AVIRIS, data were acquired at 20 sphere intensity settings to determine the linearity of response of AVIRIS. The instrument was found to be linear to within the limits of the measurement technique, which was limited by the thermally induced drift in instrument output discussed in the next section of this paper. In the current instrument configuration, the AVIRIS response was determined to be linear to within 2.4 percent. This allows an adequate radiometric calibration to be performed using less than the full suite of 20 integrating sphere output settings. Two settings have been chosen which, in combination, optimize the signal levels in AVIRIS across the 0.40 to 2.45 μm range. At each of these settings, 20 consecutive sets of data are acquired at five minute intervals. Each data set consists of 10 seconds or 120 scan lines of data, with each scan line containing 614 readings of the sphere output across the 30 degree scan angle of AVIRIS. The mean values of 100 of the scan lines of data are obtained for each run at each wavelength, and the mean of the 20 runs at each of the two integrating sphere output levels is obtained, from which the calibration file is constructed. The details of this process follow.

3.4 Creation of the calibration file

The calibration file used to convert AVIRIS DN values into radiance values is a set of multipliers consisting of 32-bit floating point numbers generated from the laboratory calibration data. These data consist of two components: radiance measurements of the two integrating sphere intensity levels taken with the spectroradiometer, and data taken with AVIRIS while viewing the integrating sphere at the same two intensity levels. These data are decommutated and archived in the same manner as flight data. In generating the calibration file, one of the two integrating sphere intensity settings is chosen for each AVIRIS spectral band based on the criterion of maximum signal without saturation. In generating the calibration file, the data from the one intensity level chosen for the specific spectral band and the zero point on the radiance versus DN plot are used in calculating the multipliers for that spectral band.

The first step in generating the calibration file is subtraction of the dark current from the AVIRIS data. Dark current subtraction is done individually on each of the 100 lines of data using the mean dark current for those 100 lines. For each spectral band the corresponding AVIRIS data are then averaged over time as a function of cross-track sample number. At a given integrating sphere setting, the mean DN value for a given spectral band and cross-track (spatial) sample number is obtained from 2000 DN values (20 sets of data at that integrating sphere output level times 100 samples per data set). This results in a set of 224 x 614 mean DN values for the 224 spectral bands and the 614 cross-track pixels. A cross-track dependence is kept in order to account for non-uniform response with scan angle due to vignetting in the foreoptics of AVIRIS. Examples of cross-track plots of DN versus sample number are shown in Figures 7a - 7d for four of the 20 data sets taken at integrating sphere output level EEEE. These examples show that both the mean value and the shape of the cross-track plots vary over time and in a manner that is uncorrelated between spectrometers. This variation enters into the calculation of calibration accuracy discussed in the next section of the paper.

The next step in generating the calibration file is to associate the 614 cross-track mean DN values of every spectral band with the corresponding radiance value for that spectral band, computed by resampling the spectroradiometer measurements to match the spectral

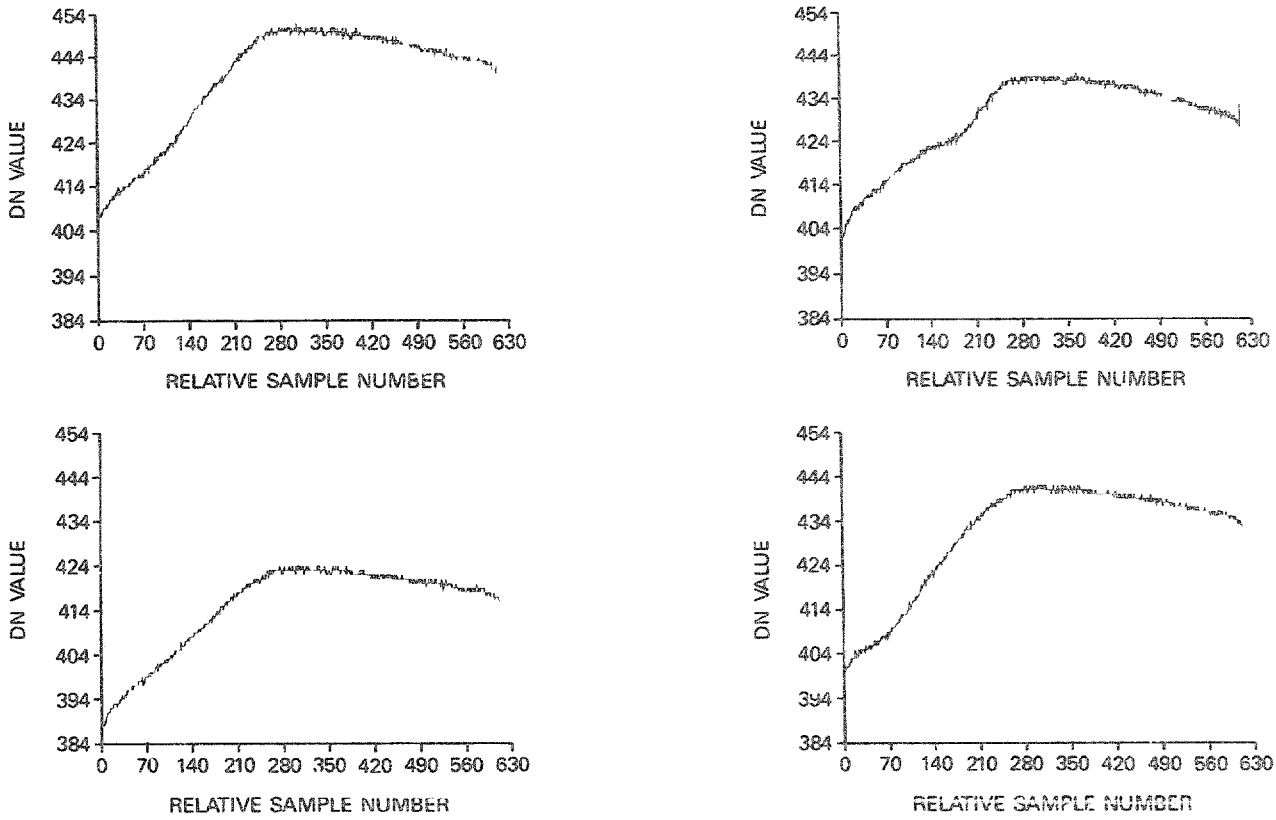

Figure 7. (a) Plots of four sets of raw AVIRIS DN after dark current subtraction versus relative cross-track sample number for spectral band 30, Spectrometer A. Each set of data was acquired from the AVIRIS integrating sphere at output level EEEE.

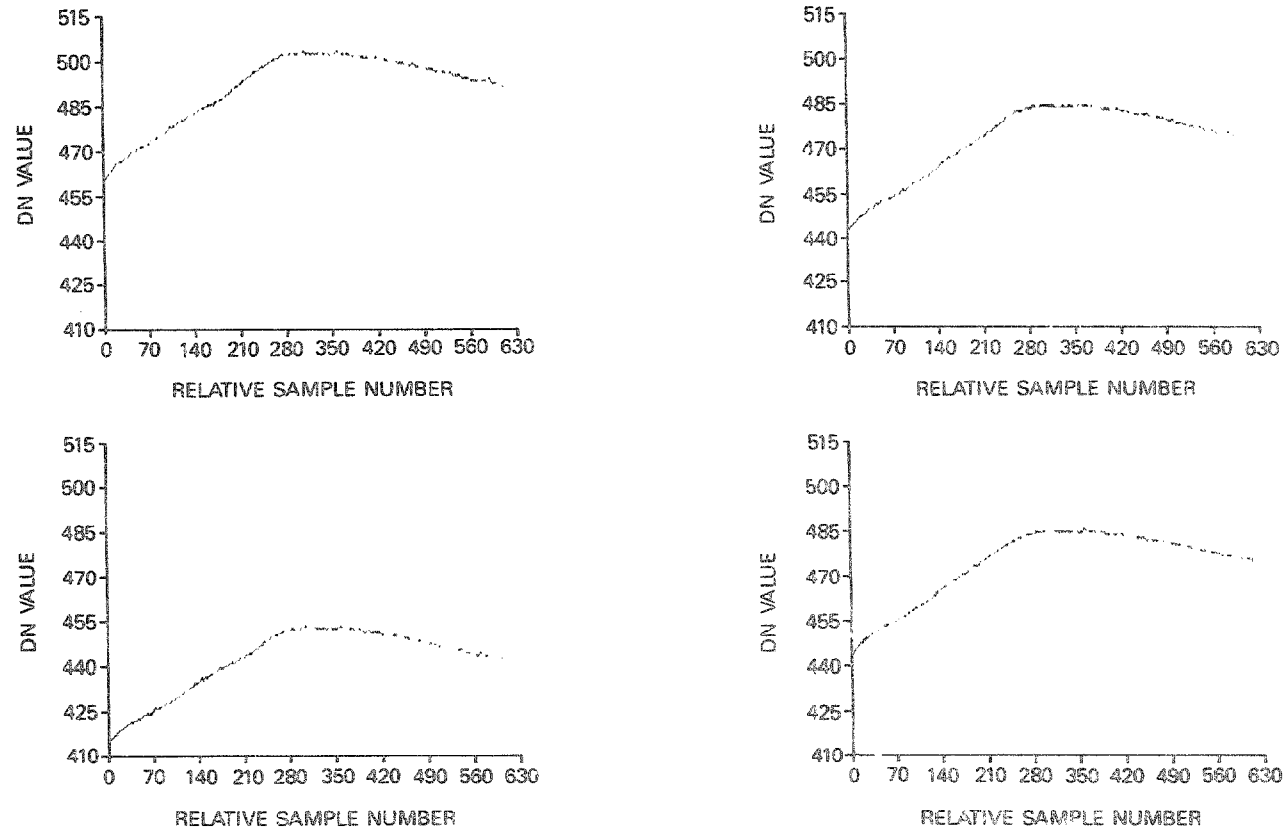

Figure 7. (b) Plots of four sets of raw AVIRIS DN after dark current subtraction versus relative cross-track sample number for spectral band 68, Spectrometer B. Each set of data was acquired from the AVIRIS integrating sphere at output level EEEE.

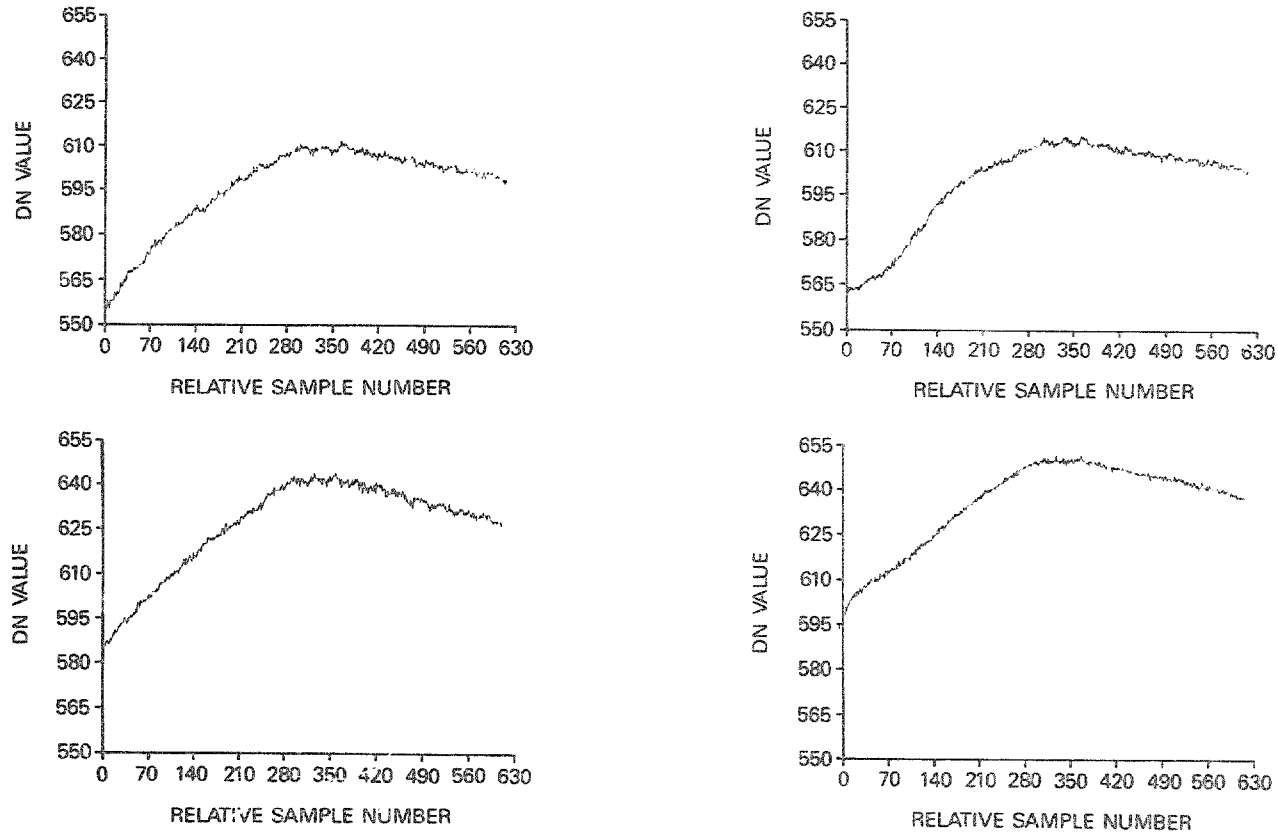

Figure 7. (c) Plots of four sets of raw AVIRIS DN after dark current subtraction versus relative cross-track sample number for spectral band 125, Spectrometer C. Each set of data was acquired from the AVIRIS integrating sphere at output level EEEE.

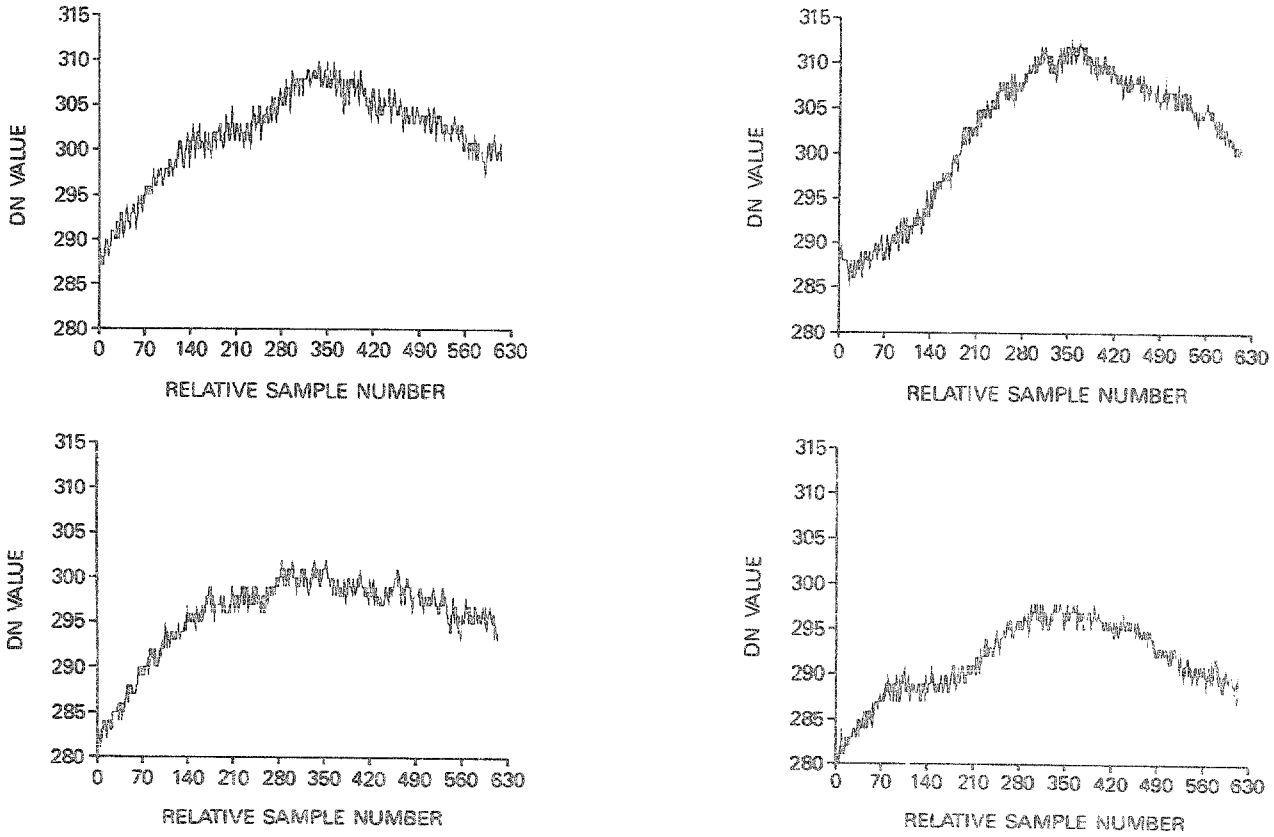

Figure 7. (d) Plots of four sets of raw AVIRIS DN after dark current subtraction versus relative cross-track sample number for spectral band 188, Spectrometer D. Each set of data was acquired from the AVIRIS integrating sphere at output level EEEE.

spacing of the AVIRIS detector elements. Assuming instrument response linearity, the final set of multipliers is computed as follows:

$$MULT(s,b) = RAD(b)/DN(s,b) \quad (2)$$

where s is the cross-track sample number, b is the spectral band number, RAD(b) is the radiance of the integrating sphere, and DN(s,b) is the signal level recorded by AVIRIS. This set of 224 x 614 multipliers is saved as the calibration file and used in the radiometric calibration of all subsequent AVIRIS data.

3.5 Application of the calibration file to AVIRIS data

The radiometric calibration of AVIRIS flight data converts 10-bit DN values to 32-bit floating point radiance values in terms of $\mu W/cm^2$-nm-sr and linearly scales the values to 16-bit integers. In the process, dark current subtraction, detector equalization, resampling to account for detector readout delays, and reconstruction of the full spectrum accounting for spectral band overlap and varying spectral spacings between spectrometers are performed.

The first step in radiometric calibration processing of flight data is dark current subtraction. One dark current value for each detector element is recorded at the end of each scan line. Dark current subtraction is done using a sliding mean of 101 dark current values as follows:

$$DN(s,b,L) = DN(s,b,L) - 1/101 \sum_{k=L-50}^{L+50} DC(b,k) \quad (3)$$

where s is the cross-track sample number, b is the spectral band number, L is the line number, and DC is the dark current.

The next step is detector response equalization. Using the multipliers stored in the calibration file, DN values are converted to 32-bit floating point radiance values, RAD(s,b,L):

$$RAD(s,b,L) = DN(s,b,L)*MULT(s,b) \quad (4)$$

Application of the multipliers at this point should remove the cross-track response asymmetry caused by foreoptics vignetting. Figures 8a - 8d show representative cross-track plots of integrating sphere data before and after this process. These figures show that while there is significant improvement, deviations from an ideal horizontal plot still exist due to time variance in the shape of the cross-track plots. Note the change in scales between the raw and radiometrically calibrated data. The magnitude of the vignetting in the raw data is about 8%. The departure from the uniform cross-track response after calibration is 2% or less and is time-varying, as discussed in section 4.3 of the paper.

Resampling to correct for detector readout delays is performed next. These delays occur because the detector elements in the line arrays are read sequentially. This results in the last element of an array acquiring a signal from a spot on the ground approximately one pixel further across the scan than was acquired by the first element. Linear interpolation is performed between successive spatial pixels within a scan line as shown in equation 5. As indicated by this equation, time increases as the sample number decreases. The time between reading out element number 64 of an array and subsequently reading out element number 1 of the same array at the next spatial pixel in the scene is equivalent to two detector element readout periods; thus the number 66 is used in equation 5. Readout of the 32 element silicon array corresponds in time to readout of elements 1 through 32 within the three 64 element InSb arrays.

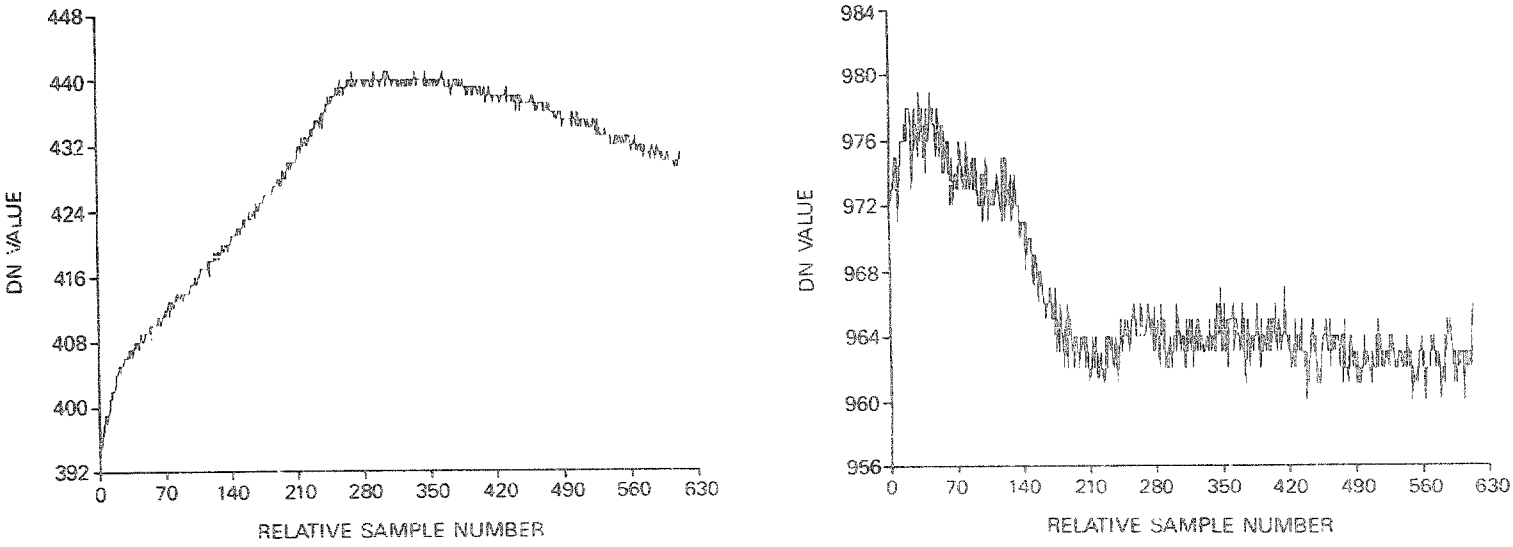

Figure 8. (a) Plots of raw (left) and radiometrically corrected (right) AVIRIS DN versus relative cross-track sample number for spectral band 30, Spectrometer A. Note the difference in scales of the vertical axes of the two plots.

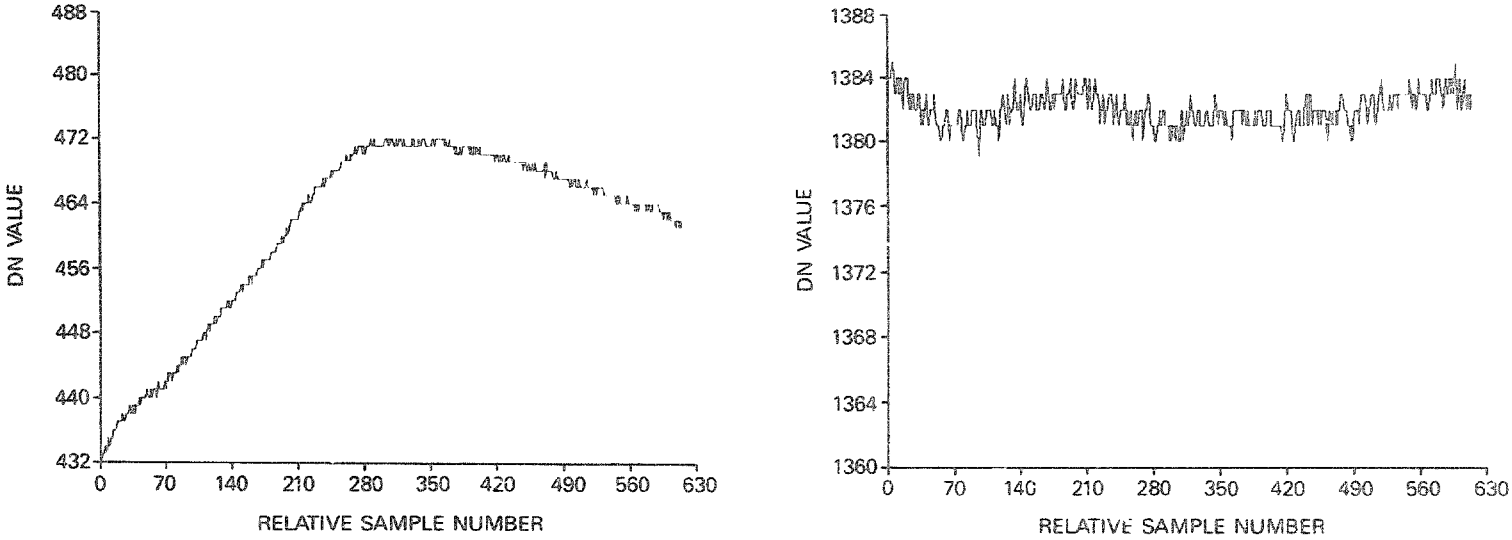

Figure 8. (b) Plots of raw (left) and radiometrically corrected (right) AVIRIS DN versus relative cross-track sample number for spectral band 68, Spectrometer B. Note the difference in scales of the vertical axes of the two plots.

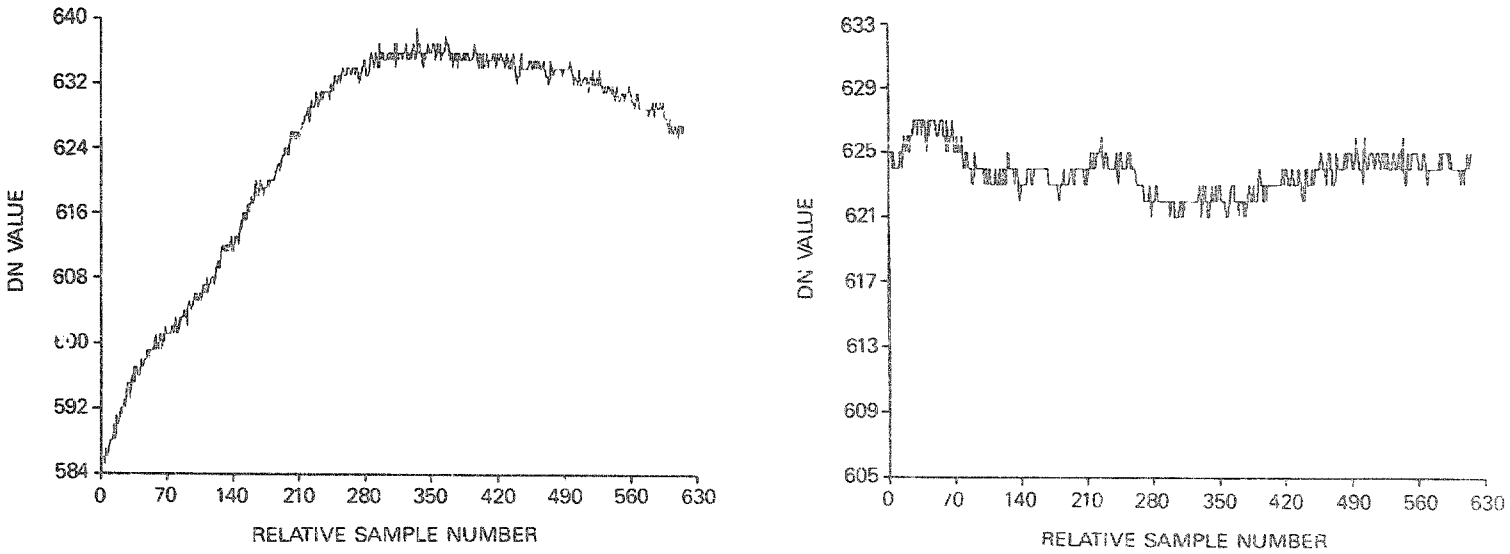

Figure 8. (c) Plots of raw (left) and radiometrically corrected (right) AVIRIS DN versus relative cross-track sample number for spectral band 125, Spectrometer C. Note the difference in scales of the vertical axes of the two plots.

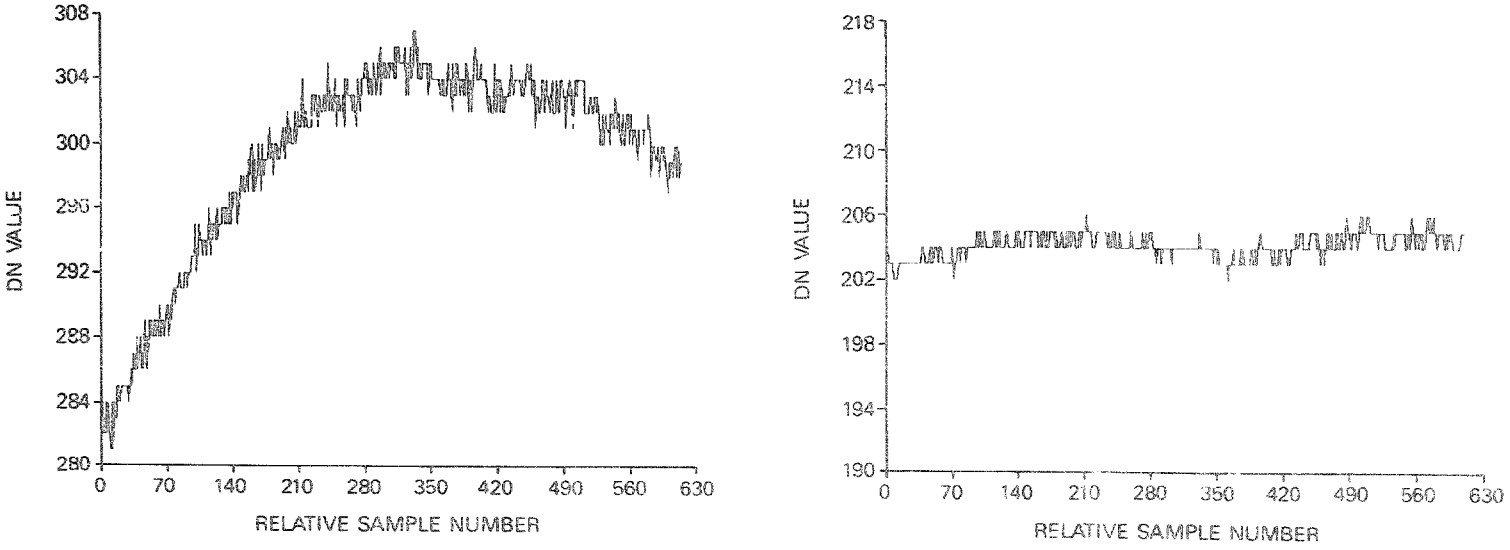

Figure 8. (d) Plots of raw (left) and radiometrically corrected (right) AVIRIS DN versus relative cross-track sample number for spectral band 188, Spectrometer D. Note the difference in scales of the vertical axes of the two plots.

$$RAD'(s,b,L) = [(b'-1)/66]*RAD(s+1,b,L) + [(67-b')/66]*RAD(s,b,L) \quad (5)$$

where b' is the detector array element number of spectral band b.

Following this, the full spectrum is reconstructed. Resampling is performed in the spectral direction to correct for spectral band overlap between spectrometers and to create a spectrum with uniform spacing of spectral band center wavelengths. This step produces 210 spectral bands from 0.4000 to 2.4482 μm with 9.8 nm spectral sampling. The center wavelength falling on each AVIRIS detector is determined during spectral calibration. Ignoring detector element number 1 in each spectrometer, unusable because of the readout architecture of the arrays, each resampled spectral band is computed by linearly interpolating between the two closest spectral bands using equation 6:

$$RAD''(s,b,L) = \left(\frac{\lambda_b - \lambda_{b-}}{\lambda_{b+} - \lambda_{b-}}\right) [RAD'(s,b+,L)-RAD'(s,b-,L)] + RAD'(s,b-,L) \quad (6)$$

where b is the resampled spectral band number, b- is the spectral band nearest to b with wavelength less than b, and b+ is the spectral band nearest to b with wavelength greater than b. Finally, the 32-bit floating point radiance values are converted to 16-bit integers by multiplying each radiance value by a factor of 100 and rounding to the nearest integer value.

As a check of the software and procedure, radiometric rectification was applied to the integrating sphere data used in generating the calibration file. The results are shown in Figure 9. Figure 9a is a spectral plot of the raw AVIRIS data, while Figure 9b is a spectral plot of the same data following radiometric rectification. This may be compared to the spectrum of the integrating sphere at the same output intensity shown in Figure 6.

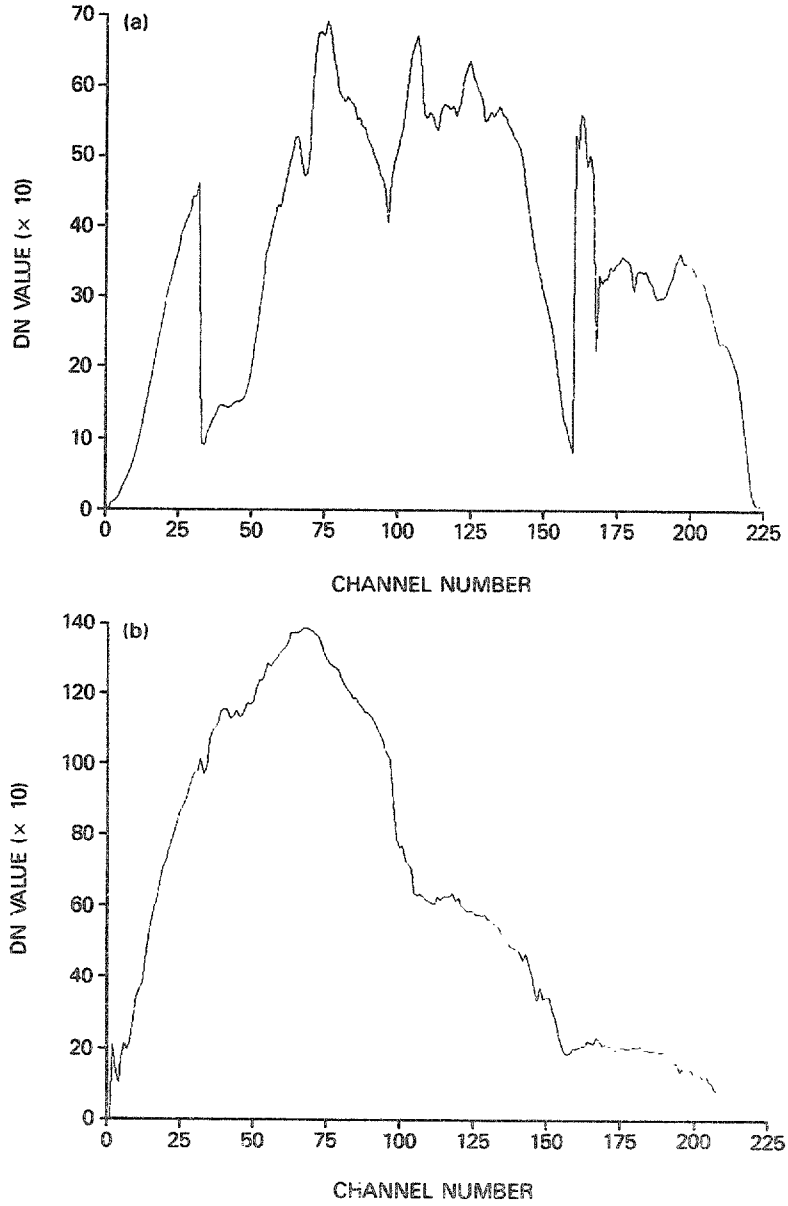

Figure 9. (a) Plot of raw AVIRIS DN after dark current subtraction versus spectral band number from the integrating sphere output level EEEE. (b) Plot of radiometrically corrected AVIRIS data versus spectral band number for the same integrating sphere output level. Compare this plot to the integrating sphere light transfer curve in Figure 6.

4.0 RADIOMETRIC CALIBRATION ACCURACY

The radiometric calibration accuracy of AVIRIS is limited by the accuracy of the integrating sphere calibration, the temporal stability of AVIRIS, the spectral calibration of AVIRIS, and such factors as sensitivity to polarization and to spectral and spatial stray light. Following is a discussion of these factors and a summary of the laboratory radiometric calibration accuracy of the instrument.

4.1 Accuracy of the integrating sphere calibration

The accuracy of the integrating sphere calibration was determined by calculating the uncertainty of the transfer from the irradiance of the standard lamp to the radiance of the halon target, measuring the uncertainty in the performance of the spectroradiometer, and measuring the uncertainty in the performance of the integrating sphere. The uncertainty associated with the use of the external irradiance standard and errors associated with its use were calculated using a differential propagation of errors analysis.[9] This calculation included the uncertainty of the calibration of the irradiance standard as provided by Optronics, the uncertainty of the reflectance of the pressed halon target, and the uncertainties introduced by the geometry of the calibration setup. The total uncertainty in the transfer of irradiance to radiance was calculated to be 2.0 percent.

The uncertainty present in the spectroradiometer measurements can be characterized by considering those factors contributing to system drift and the accuracy of the wavelength calibration. Factors contributing to system drift include chopper phase error, detector noise, and optical alignment within the spectroradiometer. These factors are contained in the overall repeatability of the measurements made with the spectroradiometer system. The repeatability was determined by performing a calibration of the spectroradiometer at the beginning and end of the calibration of the integrating sphere and comparing the results with previous calibrations of the spectroradiometer. The mean difference in the before and after calibrations was 1.8 percent. The spectral calibration uncertainty of the spectroradiometer is given by the manufacturer as 1 nm. This has been measured and confirmed at JPL. Spectral calibration uncertainty has its greatest effect on the steepest portion of the light transfer curve for a tungsten lamp, which from Figure 6 is at about 1.4 μm. A 1 nm uncertainty in spectroradiometer spectral calibration results in a radiance uncertainty of 0.5 percent at that wavelength.

The uncertainty present in the output of the integrating sphere is determined by the accuracy and stability of the lamp power supplies, the degradation with time of the lamps, and the uniformity of radiance across the output aperture of the sphere. The systematic error contributed by the integrating sphere is characterized by the repeatability of its calibration with the spectroradiometer. Multiple calibrations of the integrating sphere over several months, with each calibration consisting of several calibrations during the course of a day, give a repeatability of 1.1 percent, which accounts for power supply accuracy and stability, lamp irradiance drifts, and other unknown error sources. The uniformity of the radiance over the output aperture also affects the integrating sphere calibration accuracy. Work cited earlier gave a worst-case uniformity of 1.0 percent for the lamp and aperture settings used in calibrating AVIRIS.

Table 3 summarizes all the factors affecting the accuracy of the radiance calibration of the AVIRIS integrating sphere. Because these factors are uncorrelated, the contribution from each error source has been combined using the square root of the sum of the squares approach to arrive at a total uncertainty of 3.1 percent.

Table 3. Integrating Sphere Calibration Error Budget

Parameter	Magnitude (%)
Irradiance Transfer Uncertainty	2.0
Spectroradiometer Stability	1.8
Spectroradiometer Radiance Calibration	
Uncertainty due to Spectral Calibration Uncertainty of 1 nm	0.5
Integrating Sphere Output Stability	1.1
Radiance Uniformity Across Integrating Sphere Output Port	1.0
Integrating Sphere Calibration Accuracy	3.1

4.2 Temporal stability of AVIRIS response

The temporal stability was determined from the 20 sets of integrating sphere data acquired during the final calibration of AVIRIS prior to the start of flights aboard the U-2 in June 1987. As described earlier, these data were acquired at 5 minute intervals in an air conditioned laboratory whose temperature was maintained at 68 degrees F to assure the cycling of heaters designed to keep the four spectrometers at constant temperature. The heaters are distributed around the barrel of each spectrometer to maintain constant barrel length and geometry,

which both affect the alignment between the optical elements. Table 4 shows the results of the stability performance evaluation. Tabulated is the mean dark-current-corrected DN from one spectral band from each of the spectrometers, averaged over the full scan. The mean was constructed from 100 scan lines of data. Runs 7, 11 and 15 are missing due to a tape-read error during decommutation. Below each column of mean values for each run is the mean of all 17 runs, the maximum deviation from the mean, and the ratio of the maximum deviation to the mean. The table shows spectrometer B to have the largest drift in output over the 95 minutes of instrument operation, while spectrometer D has the smallest drift.

Table 4. Spectrometer Stability Versus Time

Run Number	Time (min)	Spectrometer (Spectral Band) Signal Level in DN			
		A (30)	B (68)	C (125)	D (188)
1	0	439	473	597	301
2	5	429	492	600	302
3	10	439	458	607	301
4	15	438	466	612	299
5	20	434	450	613	303
6	25	434	455	619	301
7	30				
8	35	430	447	622	301
9	40	429	461	624	299
10	45	416	442	626	296
11	50				
12	55	424	438	632	300
13	60	421	446	630	296
14	65	427	474	635	294
15	70				
16	75	431	474	636	292
17	80	431	440	635	296
18	85	436	464	640	297
19	90	436	439	636	298
20	95	431	458	635	291
Mean:		431	457	623	298
Std Dev:		6.34	15	13.4	3.5
Std Dev/Mean:		1.5%	3.3%	2.2%	1.2%
Max Dev:		15	35	26	7
Max Dev/Mean:		3.5%	7.7%	4.2%	2.4%

Two factors have been identified to account for the drift in output: (1) The spectrometer heaters are causing a distortion in the barrel geometry while they are on the heating cycle. This causes the signal to drift off the detector array in a direction perpendicular to the dispersion, resulting in a drop in signal while the heaters are on, but no shift in spectral alignment. After the heater of a given spectrometer switches off, the temperature of the barrel becomes uniform across the barrel and the geometry returns to optimal, as does the output signal level. (2) The alignment of the spectrometers is also affected by thermally induced warpage of the rails on which the spectrometers are mounted. This effect results in a similar shift of image position on the detector arrays.

There are potentially two ways of correcting for the thermally induced drift in signal output of the spectrometers. The onboard calibrator was designed to provide information for such corrections. The signal from the onboard calibrator falling on the detectors of each spectrometer, however, has proven to be insufficiently stable to be of use for this correction. Plans for improving the stability of the onboard calibrator signal are discussed in section 5.0 of the paper. The second way of correcting for the signal level output drift of the spectrometer is by referencing the output of each spectrometer to that of the most stable of the spectrometers, spectrometer D. This is done by taking advantage of the spectral overlap between spectrometers. Spectrometer C output can be corrected by adding or subtracting an offset which makes the output of the last three spectral bands equal to the output of the corresponding first three spectral bands of spectrometer D. Similarly, spectrometer B can be corrected relative to C, and spectrometer A can be corrected relative to B, thus limiting the drift of all spectrometers to that of spectrometer D, which is 2.4 percent. This correction is not applied to AVIRIS data during routine radiometric rectification, but the data for making the correction are readily available to those investigators wishing to perform it. Plans for improving the output stability of all four spectrometers are discussed later in the paper.

4.3 Other factors affecting radiometric calibration accuracy

Five additional instrument-related factors have been identified which affect the absolute radiometry of AVIRIS. These are: (1) Non-systematic vibrationally induced fluctuations in instrument output level, (2) polarization sensitivity, (3) spectral calibration uncertainty, (4) spectral stray light, and (5) spatial stray light. The non-systematic vibrational effects were noted earlier in the plots of DN versus cross-track scan position (Figures 7 and 8). They occur randomly in the output of the spectrometers, but at roughly two frequencies: There is a

signal level fluctuation of as much as 2.0 percent occurring intermittently approximately once per scan cycle. A higher frequency fluctuation is occasionally seen of magnitude 0.7 percent of the signal level with a frequency between 12 and 18 cycles per scan line. These effects do not occur throughout all four spectrometers at the same time. Because of their random nature, they must be included in the calibration error budget. Their nature and eventual removal will be addressed in section 5.0 of the paper.

Polarization sensitivity is measured by placing filters that polarize visible and infrared wavelengths between the AVIRIS foreoptics and the integrating sphere and recording instrument output level as a function of filter polarization angle. A maximum signal loss of 5.0 percent was measured. The effect of spectral calibration uncertainty was calculated by determining the uncertainty of the radiance at the steepest part of the light transfer curve of the integrating sphere, which occurs at 1.4 μm. An uncertainty of 0.8 nm in the spectral calibration of spectrometer C, which covers this wavelength, yields a radiance uncertainty of 0.5 percent.

Spectral stray light affects radiometric calibration accuracy by contaminating adjacent spectral bands to a degree that is scene-variant. The measurement of spectral stray light is difficult, however, and an adequate technique for characterizing its magnitude in the AVIRIS spectrometers has not yet been devised. A crude measurement has been made by illuminating the instrument with narrow bandwidth light from the laboratory monochromator to establish the signal level on detector elements away from the one illuminated with the monochromator. Within the limits of the instrument electronic noise level, we estimate that the magnitude of the spectral stray light does not exceed 2 percent.

Spatial stray light affects radiometry by scattering light from adjacent pixels of the scene into nearby pixels. It too, is scene-dependent. In an instrument such as AVIRIS, only the foreoptics contribute to spatial stray light. Its magnitude in the AVIRIS foreoptics was measured by illuminating the foreoptics with collimated light passed through a 1 mrad slit. The signal levels were measured across the full field of view of AVIRIS. Measurements were made with the 1 mrad illumination falling on the center of the AVIRIS field of view and at 10 and 20 degrees to either side of the center. The contribution of spatial stray light in the pixels immediately adjacent to the illuminated pixel was 2.0 percent. The signal level at the next pixel was less than 0.3 percent. The 2.0 percent figure was used in the calculation of the overall radiometric accuracy.

4.4 AVIRIS radiometric calibration accuracy

The accuracy of the absolute radiometry of AVIRIS was calculated by taking the root sum square of all the elements discussed above and was found to be 7.3 percent. The quantities used in the calculation are summarized in Table 5. This is the accuracy of the laboratory radiometric calibration of the instrument. Work in progress on the airborne radiometric performance of the instrument using data from the onboard calibrator indicates that the signal levels are less stable in the U-2 than in the laboratory, because the air temperature in the bay of the airplane containing AVIRIS is about 32 degrees F, compared to the 68 degree air temperature in the laboratory. The lower temperature causes the spectrometer heaters to cycle more frequently and for longer periods.

Table 5. Total AVIRIS Radiometric Calibration Error Budget

Parameter	Magnitude (%)
Integrating Sphere Calibration Accuracy	3.1
AVIRIS Thermally Induced Output Drift	2.4
AVIRIS Vibrationally Induced Output Drift	
Low Frequency	2.0
High Frequency	0.7
Polarization Sensitivity	5.0
Radiometric Effect of Spectral Calibration Uncertainty	0.5
Spectral Stray Light	2.0
Spatial Stray Light	2.0
AVIRIS Radiometric Calibration Accuracy	7.3

The relative radiometry of the instrument is affected primarily by the accuracy of the spectral calibration of the instrument, for this determines how well the radiance of the integrating sphere at a given wavelength is matched to the corresponding AVIRIS wavelength. Relative radiometry refers to the equalization of detector response so that if, for example, two adjacent detector elements centered at λ_n and λ_{n+1} are illuminated with light at those respective wavelengths but of the same intensity, the output intensity of those detectors after radiometric calibration is equal. Because the output intensity of the integrating sphere varies with wavelength, inaccuracies in the spectral

calibration can result in inaccuracies in the uniformity correction or relative radiometry. The relative radiometric accuracy can be measured by applying the radiometric calibration to one of the 20 sets of data collected from the integrating sphere and comparing the ratio of the radiance at two adjacent wavelengths from those corrected data to the ratio of the integrating sphere radiance at the same wavelengths as measured by the calibrated spectroradiometer. This was done at several wavelengths. The results of the analysis gave a relative radiometric calibration accuracy of 0.4 percent.

5.0 FUTURE PLANS

Further refinements to the laboratory calibration of AVIRIS are planned through additional experiments in calibrating the integrating sphere and through improvements to AVIRIS designed to remove the effects that limit the instrument radiometry. During the 1987-88 winter, the instrument will undergo several improvements at JPL, including a realignment of the foreoptics to remove the vignetting, replacement of the preamplifier and clockdriver boards with more robust versions that are less sensitive to vibration, reconfiguration of the spectrometer heaters with a new thermal control circuit and optimized placement of the heaters to minimize distortion to the spectrometer barrel during the heating cycle, and finally, installation of kinematic mounts between the spectrometers and the instrument mounting rails to reduce the transmission of vibration and warpage from the mounting rails, and reduce the conductive heat loss from the spectrometers to the mounting rails. Also, a stabilized power supply will be installed in the onboard calibrator, and the alignment of the optical fibers from the calibrator to the spectrometers will be improved. Both modifications together should improve the stability of the onboard calibrator signal.

In addition to the work described above, a field calibration experiment was performed in September 1987 to determine the in-flight radiometry of AVIRIS for comparison with the laboratory calibration. Analysis of the data is just beginning at the time of this writing. Additional field experiments are planned in 1988 to verify the performance of AVIRIS and its laboratory calibration after the improvements described above are completed. Results of the next laboratory calibration and the following field calibration experiment will be documented in an AVIRIS project calibration report in 1988.

6.0 ACKNOWLEDGEMENTS

The authors would like to express their gratitude to many colleagues for helpful suggestions and stimulating discussions on radiometric calibration which have helped us greatly in developing the procedures described in this paper: At JPL, Jim Conel, Robert Green, Deanne Tucker, Frank Palluconi, Harold Lang, Mike Abrams, John Wellman and Dave Norris; at the University of Arizona, Phil Slater; at the U.S. Department of Agriculture, Ray Jackson; and at the Goddard Space Flight Center, Bruce Guenther.

The work described in this paper was carried out at the Jet Propulsion Laboratory, California Institute of Technology, under a contract with the National Aeronautics and Space Administration.

7.0 REFERENCES

1. G. Vane, M. Chrisp, H. Enmark, S. Macenka and J. Solomon, "Airborne visible/infrared imaging spectrometer: an advanced tool for earth remote sensing," Proc. 1984 IEEE Int'l. Geoscience and Remote Sensing Symposium, SP215, 751-757 (1984).
2. W. M. Porter and H. T. Enmark, "A system overview of the Airborne Visible/Infrared Imaging Spectrometer (AVIRIS)," Proc. SPIE, 834 (1987).
3. G. Vane and A. F. H. Goetz, "Terrestrial imaging spectroscopy," Remote Sensing of Environment, 24(1), in press (1987).
4. A. F. H. Goetz, G. Vane, J. E. Solomon and B. N. Rock, "Imaging spectrometry for earth remote sensing," Science, 228(4704), 1147-1153 (1985).
5. D. Tucker and G. Vane, "Radiometric calibration of the Airborne Imaging Spectrometer," in Proceedings of the Second Airborne Imaging Spectrometer Data Analysis Workshop, Gregg Vane and Alexander F. H. Goetz, eds., JPL Publication 86-35, Jet Propulsion Laboratory, Pasadena, CA, 17-20 (1986).
6. J. E. Conel, R. O. Green, G. Vane, C. J. Bruegge and R. E. Alley, "AIS-2 radiometry and a comparison of methods for the recovery of ground reflectance," in Proceedings of the Third Airborne Imaging Spectrometer Data Analysis Workshop, Gregg Vane, ed., JPL Publication 87-30, Jet Propulsion Laboratory, Pasadena, CA, 18-47 (1987).
7. V. R. Weidner and J. J. Hsia, "Reflection properties of pressed polytetrafluoroethylene powder," J. Opt. Soc. Am., 71(7), 856-861 (1981).
8. P. N. Slater, personal communication (1986).
9. P. R. Bevington, Data Reduction and Error Analysis for the Physical Sciences, 336 pp., McGraw Hill, New York (1969).

First results from the Airborne Visible/Infrared Imaging Spectrometer (AVIRIS)

Gregg Vane

Jet Propulsion Laboratory, California Institute of Technology
4800 Oak Grove Drive, Pasadena, California 91109

ABSTRACT

After engineering flights aboard the NASA U-2 research aircraft in the winter of 1986-87 and spring of 1987, extensive data collection across the United States was begun with the Airborne Visible/Infrared Imaging Spectrometer (AVIRIS) in the summer of 1987 in support of a NASA data evaluation and technology assessment program. This paper presents some of the first results obtained from AVIRIS. Examples of spectral imagery acquired over Mountain View and Mono Lake, California, and the Cuprite Mining District in western Nevada are presented. Sensor performance and data quality are discussed, and in the final section of the paper, plans for the future are described.

1.0 INTRODUCTION

The Airborne Visible/Infrared Imaging Spectrometer (AVIRIS) is the second in a series of instruments under development at the Jet Propulsion Laboratory (JPL) leading to an observatory-class high resolution imaging spectrometer aboard the NASA polar orbiting Earth Observing System (Eos) in the mid-1990s.[1] AVIRIS was conceived of as an operational airborne sensor for routine collection of spectral images to provide data essential for developing new methodologies for information extraction from hyperspectral data acquired from space.[2] This new class of data has proven to be of considerable value to a wide range of earth science disciplines, including botany, geology, atmospheric science and remote sensing science.[3, 4] Work with the predecessor to AVIRIS, the JPL-built Airborne Imaging Spectrometer (AIS)[5], has established a broad community of earth scientists who are now positioned to take advantage of the more comprehensive data sets provided by AVIRIS and its spaceborne successors. Many papers published over the past several years on results obtained with data from AIS attest to the utility of imaging spectroscopy in addressing a broad range of earth science problems.

A thorough description of AVIRIS, its calibration and the AVIRIS ground data processing facility can be found in the papers in these proceedings (see, for example, Porter and Enmark[6], Vane et al.[7], and Reimer et al.[8]). The characteristics of AVIRIS are summarized briefly here. The sensor acquires images from the NASA U-2 aircraft in the whisk-broom imaging mode. Foreoptics consisting of a two-faceted scan mirror and other relay mirrors focus light from one ground instantaneous field of view (GIFOV) onto four optical fibers, as shown in Figure 1. Each fiber terminates in one of four spectrometers, where the light is dispersed off an aspheric grating and focussed onto a line array of detectors. Figure 2 is an artist's rendering of the flight hardware, showing the physical layout of the instrument's major components. Spectrometer A has a 32-element line array of silicon detectors and covers the spectral range 0.40 to 0.71 μm; Spectrometers B, C, and D each have a 64-element line array of indium antimonide detectors and cover the spectral ranges 0.68 to 1.28, 1.24 to 1.86, and 1.83 to 2.45 μm, respectively. Each picture element (pixel) on the ground is imaged in 220 spectral bands. After resampling to equalize the spectral sampling interval and remove the overlap between spectrometers, this reduces to 210 spectral bands in the radiometrically calibrated data.[7] In each cycle of the foreoptics scan mirror, 614 cross-track pixels are acquired. Twelve scans per second are made as the forward motion of the aircraft provides the along-track scan. Each pixel is 20 by 20 m at sea level from the nominal altitude of the U-2, with a pixel-to-pixel center spacing of 17 m to minimize spatial undersampling over mountainous terrain. The oversampling is corrected during geometric rectification of the data at the AVIRIS ground data processing facility. The result is an image 550 pixels wide, spanning 10.5 km on the ground. On board the aircraft, the raw data are digitized to 10 bits and recorded on a high-density tape recorder at the rate of 17 Mbps. An onboard calibrator provides a frequent update of the detector dark current and instrument spectral and radiometric performance. The observational characteristics of the AVIRIS system are summarized in Tables 1, 2, and 3.

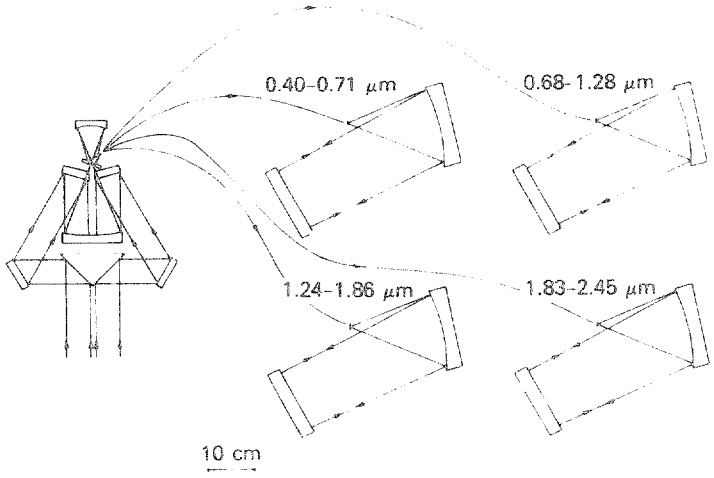

Figure 1. Schematic diagram of the AVIRIS optical configuration.

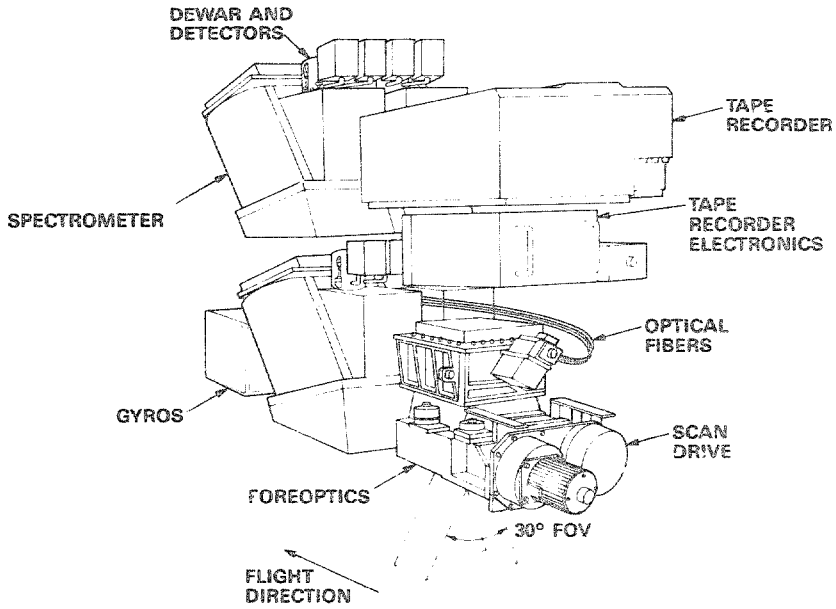

Figure 2. Artist's drawing of the AVIRIS flight hardware showing the physical layout of the major subsystems.

Table 1. General Performance of AVIRIS

Parameter	Performance
Spectral Coverage	0.40 to 2.45 μm
Spectral Sampling Interval	9.6 to 10.0 nm
Number of Spectral Bands	
Raw Data	220
Radiometrically Corrected Data	210
Instantaneous Field of View (IFOV)	0.95 mrad
Ground IFOV from U-2 Aircraft	20 m
Angular Field of View (FOV)	30 deg
Ground FOV from U-2 Aircraft	10.5 km
Number of Cross-Track Pixels	
Raw Data	614
Geometrically Corrected Data	550
Data Encoding	10 bits
Data Rate	17 Mbps
Radiometric Calibration Accuracy (Laboratory)	
Absolute	7.3%
Spectral Band-to-Band	0.4%
Spectral Calibration Accuracy	2 nm

Table 2. Required and Achieved Performance of AVIRIS Scanner

Parameter	Required	Achieved
Scan Rate	12 Scans/sec	12 Scans/sec
Cumulative Pixel Position Error over 1 Scan Line	0.5 Pixel	0.26 Pixel
Maximum Pixel-to-Pixel Position Error within 1 Scan Line	0.1 Pixel	0.06 Pixel
Uncompensated Motion of Scan Drive Housing due to Vibration	0.1 Pixel	0.01 Pixel

Table 3. AVIRIS Signal-to-Noise Performance in the Laboratory

Spectrometer	Wavelength (μm)	Required SNR	Measured SNR[a]
A	0.7	100:1	150:1
B	1.0	None	140:1
C	1.6	None	70:1
D	2.2	50:1	30:1

[a] The measured performance is from integrating sphere data normalized to a scene (ground) albedo of 0.5 through a standard mid-latitude, mid-summer atmosphere with 23-km visibility.

Acquisition of data with AVIRIS for scientific applications began in June 1987 and continued through the middle of October 1987, when the instrument was returned to JPL for a post-season calibration and instrument upgrades. Data were acquired over vegetated sites in Florida, Minnesota, Oregon and California, over the ocean off the California coast near San Francisco, and over geological sites in Colorado, Wyoming, Utah, Nevada, Arizona and California. Also, data were collected over a radiometric calibration site in the Mojave Desert of California. Most of the flight activity in 1987 was done in support of the NASA-sponsored AVIRIS data evaluation and technology assessment program, although several investigators were funded outside this program by NASA to conduct basic earth science research. During the course of the summer, data were acquired for a total of 20 investigators. In the following section of the paper, early results from three of the sites under study by the AVIRIS project are presented.

2.0 FIRST RESULTS FROM AVIRIS

AVIRIS is flown in the NASA U-2 aircraft from the Ames Research Center at Moffett Field, California. Because of the proximity to the San Francisco peninsula with its varied cultural and natural surface features, the first images acquired with AVIRIS were from that area. Figure 3 shows a suite of four spectral images acquired over the Moffett Field and Mountain View areas in June 1987 at the start of scientific data acquisition. Shown are raw data to which no radiometric or geometric corrections have been applied except for an onboard roll correction performed during image acquisition. Figure 3(a) is from Spectrometer A, spectral band 30, centered at 0.682 μm; Figure 3(b) is from Spectrometer B, spectral band 68, centered at 1.014 μm; Figure 3(c) is from Spectrometer C, spectral band 125, centered at 1.518 μm; and Figure 3(d) is from Spectrometer D, spectral band 188, centered at 2.095 μm. The images are 614 pixels across and 512 lines in length. One scan line of 614 pixels is acquired in one twelfth of a second; 512 scan lines are acquired in about 43 seconds. Figure 3 represents a small portion of a much longer flight line beginning at Point Reyes, north of San Francisco, and extending south to San Jose, which is a few kilometers south of Mountain View. The total flight line length was over 100 km, which represents about 7 minutes of data acquisition.

A visual inspection of the images in Figure 3 reveals several characteristics of the quality of the AVIRIS data. The inherent geometry of the raw images is good, as evidenced by the straight runways at Moffett Field and other linear features in the scene. The stability of the detector output on a time scale from one twelfth of a second to 43 seconds is also good, as can be seen by the uniformity of the images. Indeed, over the entire 7 minutes of the total flight line over the San Francisco area, the detector output appeared to be stable, except for the offset in the spectral images from Spectrometer D, discussed below. The spatial resolution appears to match the performance expected from laboratory measurements of the instrument instantaneous field of view. For example, the dikes separating the evaporation ponds to the east of Moffett Field are 15 to 20 meters wide; the AVIRIS pixel size from the 20 km altitude of the U-2 is 20 m. The dikes are clearly visible in

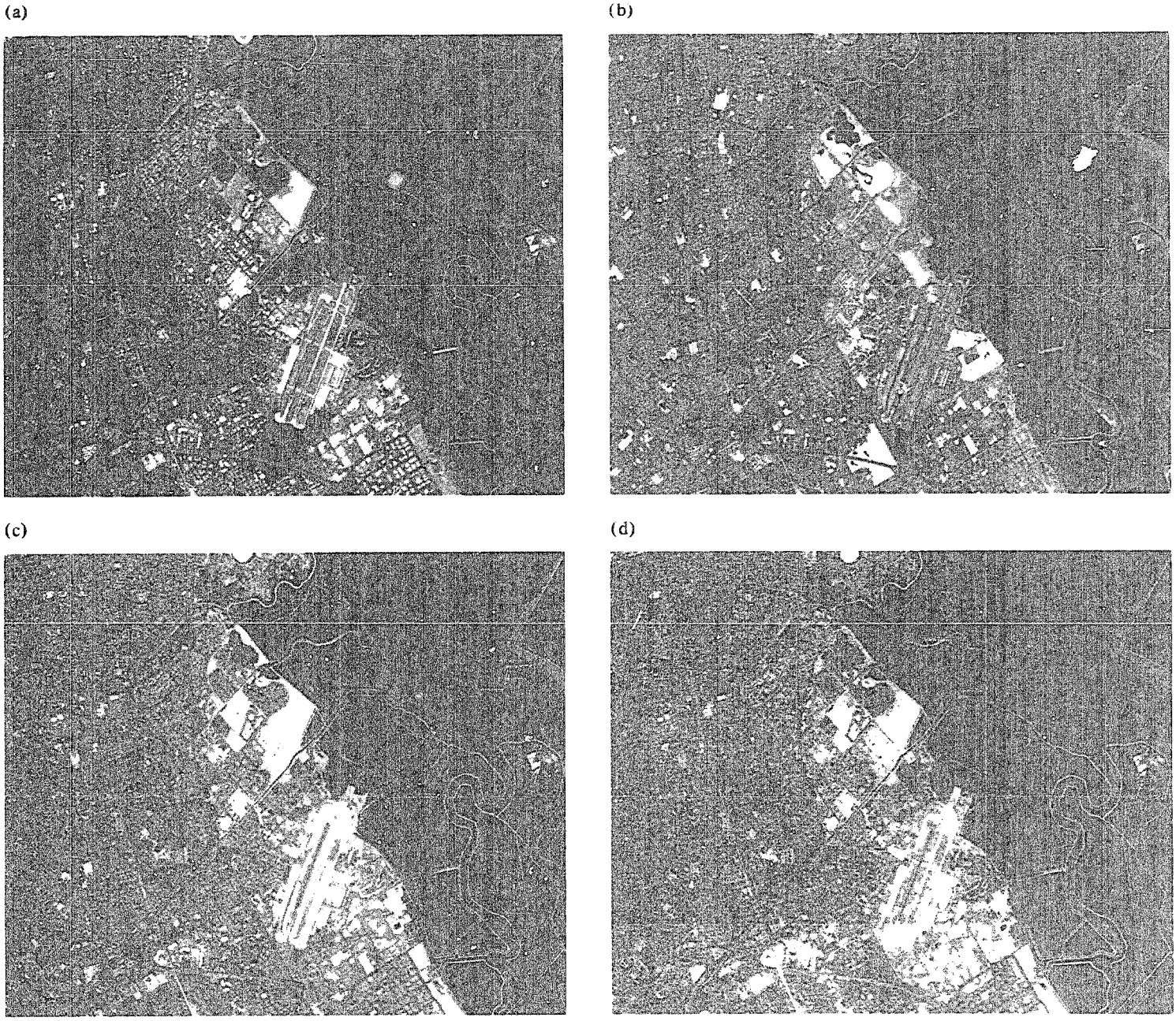

Figure 3. Four 10-nm spectral images from Mountain View, California, each from a different AVIRIS spectrometer: (a) image A is from spectrometer A, spectral band 30, centered at 0.682 μm; (b) image B is from spectrometer B, spectral band 68, centered at 1.014 μm; (c) image C is from spectrometer C, spectral band 125, centered at 1.518 μm; and (d) image D is from spectrometer D, spectral band 188, centered at 2.095 μm. These images are from raw data; no radiometric or geometric correction has been applied except for aircraft roll compensation performed during data acquisition. In addition to these four images, another 216 10-nm images across the spectral range from 0.40 to 2.45 μm were acquired simultaneously.

the images in Figure 3, appearing as thin, dark features (the tops of the dikes) outlined on either side by bright lines (the salt deposits on the flanks of the dikes). The visual appearance of the images also indicates the range in signal-to-noise ratios (SNRs) among the four AVIRIS spectrometers. The SNRs measured in the laboratory for spectral bands 30 and 68 are in excess of 100:1 for a surface albedo of 0.5, for spectral band 125 about 70:1, and for band 188 about 30:1. Figure 3(d) exhibits one of the artifacts of the AVIRIS electronics characteristic of the instrument configuration during the 1987 flight season. The offset in brightness occurring near the bottom of the image is the result of a vibrationally induced change in a potentiometer setting in the preamplifier circuit, which caused a step change in the offset applied to the data during onboard processing. In addition to this non-subtle effect occurring most frequently in Spectrometer D, at the end of the flight season it was discovered that a long-term drift in the setting of the same potentiometer caused a variation in the overall signal level that, while not obvious from a visual inspection of the images, has an effect on instrument radiometry. This effect appears throughout all four spectrometers to varying degrees during the flight season. The cause of the problem will be removed during instrument refurbishment in the winter of 1987-88.

A color rendition of the Moffett Field image is shown in the frontispiece to the Proceedings. Using radiometrically corrected data, the image was produced from three 0.01 μm wide spectral bands centered at 0.557, 0.665, and 0.910 μm. These spectral bands were assigned the colors blue, green, and red, respectively. In this rendition, red corresponds to healthy vegetation and blue/green corresponds to water. Note the degree of shading in the water in the southern part of San Francisco Bay and in the evaporation ponds to the east of Moffett Field. This shading is indicative of variations in the concentration and composition of suspended particulates in the water. The Moffett Field data set has been archived at JPL as one of two standard products available to investigators wishing to gain experience in working with AVIRIS data. The second data set, described below, is from Cuprite, Nevada. A copy of either data set can be obtained by writing to the author.

Figure 4 shows another image acquired with AVIRIS in the first flight season. Shown is an image in spectral band 68 (1.014 μm) of Mono Lake, California. Mono Lake is an extinct volcanic caldera some 15 km in diameter, located at about 2500 m above sea level. It provides a good test of instrument performance because of the very high albedo contrast between the dark water and the bright evaporite deposits on the islands and along the shores of the lake. The north shore of the lake is characterized by broad, contiguous beaches of seasonal bright evaporite crust and dark basalt pebbles that extend with more or less lateral continuity an arcuate distance of 15 km. Visual inspection of the image indicates that the boundaries between these high contrast areas remain sharp, verifying that AVIRIS does not suffer from the effects of residual imagery which result from inefficient charge transfer during detector readout, and from such optical effects as stray light. The image also attests to the large dynamic range of the sensor. Details in the image are clear over a wide range of surface brightnesses. Note the thin, filamentous cumulus cloud over the lake.

Figure 5 is an image acquired over the Cuprite mining district in western Nevada; shown is spectral band 68, centered at 1.014 μm. The mining district straddles U.S. Highway 95 approximately 30 km south of Goldfield, Nevada. The eastern half of the district is an area of extensive hydrothermal alteration within a sequence of rhyolitic welded ash flow and air fall tuffs. The altered units consist of a central core of almost pure silica, a ring of opalized rocks containing alunite and kaolinite, and an outer argillized zone containing mainly kaolinite, montmorillonite, and opal, and some limonite.[9] Cuprite has been studied extensively over the past 10 years with almost every remote sensing instrument operating in the wavelength region between 0.4 and 14 μm.

Using the Spectral Analysis Manager (SPAM) software developed at JPL[10], spectra were constructed after radiometric calibration of the data from the areas indicated in Figure 5. Area "A" is the Stonewall Playa. A representative spectrum obtained from the average of a 5 by 5 pixel portion of the playa is shown in Figure 6. The spectrum has the characteristic shape of the solar irradiance curve convolved with the absorption spectrum of the earth's atmosphere. The major absorption features at 1.4 and 1.9 μm are due to atmospheric water. Using the wavelength position mapping feature of SPAM, many of the smaller atmospheric absorption features were located in terms of their wavelength positions in the AVIRIS data. The first number associated with each identified feature in Figure 6 was obtained from the AVIRIS data in this manner. The information in parentheses indicates the wavelength position of the feature according to the LOWTRAN VI atmospheric model, and the atmospheric constituent(s) causing it. As can be seen, there is very good agreement between the AVIRIS-derived and LOWTRAN wavelength positions. Note the CO_2 absorption features at 1.58 and 1.61 μm. These features are separated by only 0.03 μm, but are clearly resolved at the AVIRIS spectral sampling level, indicating that the spectral resolution of the instrument as defined by the Nyquist sampling theorem is being realized. According to the Nyquist theorem, a spectrum sampled at 0.01 μm intervals is sampled at a spectral resolution of 0.02 μm.

Figures 7, 8, and 9 show spectra from areas B, C, and D, respectively, in Figure 5. The spectra were constructed after dividing the Cuprite scene by the spectrum in Figure 6 to correct for atmospheric and solar insolation effects. Area B is known locally as Kaolinite Hill for its extensive and well-exposed deposit of the clay mineral kaolinite. The wavelength positions of the absorption features were determined using the SPAM software and agree closely with the laboratory-determined wavelength positions for these features.[11, 12] The identification of the double absorption feature at 2.16 and 2.21 μm was one of the major criteria in specifying the spectral and radiometric resolution of AVIRIS. Through analysis of AIS spectra from Kaolinite Hill and laboratory spectral analysis, it was determined that a SNR of about 50:1 is required to resolve the double absorption feature at the AVIRIS spectral resolution. As noted earlier in the paper, the SNR of AVIRIS at this wavelength during the 1987 flight season was only 30:1. The feature has been resolved nonetheless because of the excellent exposure of the mineral at Cuprite.

Other minerals at Cuprite which are difficult to distinguish from kaolinite visually are alunite, whose spectrum is shown in Figure 8, and Buddingtonite, whose spectrum is shown in Figure 9. Alunite occurs widely throughout the Cuprite area, while Buddingtonite has been observed only in a few locations at the site. The occurrence of Buddingtonite at Cuprite was discovered only in 1985 through the analysis of AIS spectra.[13] Its occurrence there represents the fifth known location for the mineral in a hot spring environment, where it is associated with disseminated gold deposits. The absorption features at 2.02 and 2.11 μm are its chief diagnostic features distinguishing it spectrally from the other minerals at Cuprite. Alunite is distinguished by its absorption feature at 2.16 μm, which, at the spectral resolution of AVIRIS, is resolved as a double absorption feature. The secondary feature occurs at 2.20 μm.

3.0 FUTURE PLANS

During the course of instrument checkout and calibration prior to the start of data collection with AVIRIS in the summer of 1987, several areas of less-than-optimal performance were identified and an upgrade program was planned for the period between the 1987 and 1988 flight seasons. A performance deficiency related to changes in offset has been discussed in this paper. Thermally induced drift in signal levels resulting from distortion of the spectrometer alignment, and an 8 percent vignetting on the left side of the foreoptics were also discovered. Further, a small amount of systematic noise in Spectrometer D, and random noise in both Spectrometer C and D resulted in lower SNRs than the instrument model predicts should be achievable in these spectrometers. Aside from the lower SNR performance, the net effect of most of the deficiencies is a degradation in the absolute radiometry of the data. To remove these performance-limiting factors and place the sensor in its final configuration for long-term operations, the following activities will be conducted in the winter of 1987-88. After a complete post-flight-season spectral and radiometric calibration of AVIRIS, the instrument will be disassembled for rework. To remove the offset drift and minimize the random and periodic electronic noise, the preamplifier and clock driver board designs will be modified and new boards fabricated. To remove vignetting in the foreoptics, the optics will be realigned. The thermally induced drift in signal level will be addressed by (1) implementing a new spectrometer heater design, and (2) floating the spectrometers on kinematic mounts. The latter should also minimize the effects of the vibrational environment. A few other small tasks will be completed during this winter that will improve the reliability of the sensor for long-term operations.

Figure 4. Raw AVIRIS image of Mono Lake, California, in spectral band 68, centered at 1.014 μm. No radiometric or geometric correction has been applied. The scene is approximately 10.5 by 20 km in area.

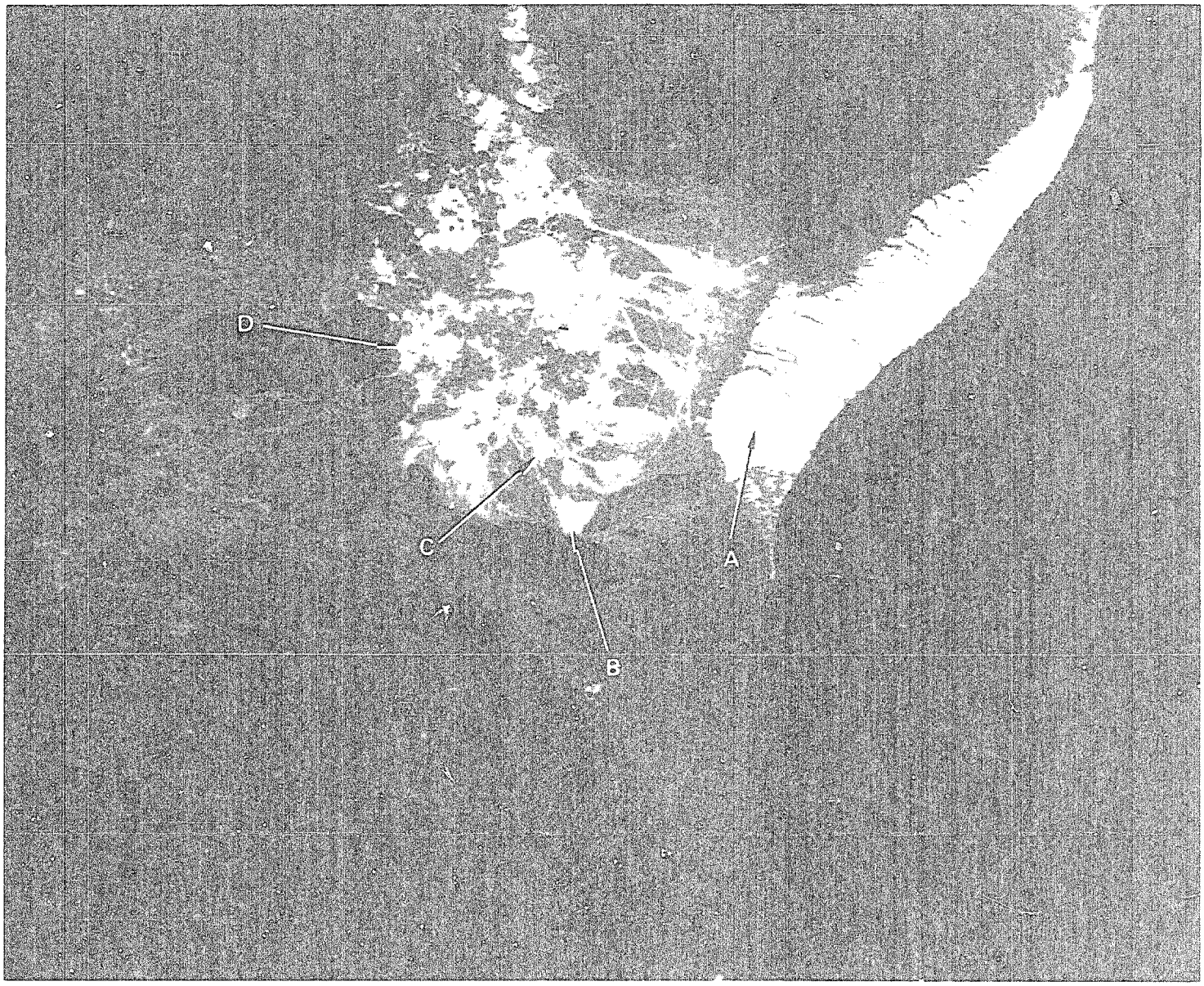

Figure 5. AVIRIS image of the Cuprite mining district, Nevada, in spectral band 68, centered at 1.014 μm. A is Stonewall Playa, B is Kaolinite Hill, C marks the location of a deposit of the mineral alunite, and D marks the location of a deposit of the mineral Buddingtonite.

In addition to the upgrades to the instrument, further work is planned in the areas of data processing and instrument calibration. Results from further analysis of flight data will be used to determine whether additional efficiency can be achieved at the ground data processing facility by reducing some of the steps involved in the application of the radiometric calibration to the flight data. Further analysis of the procedures used in the laboratory for obtaining the data for the radiometric calibration file will be conducted to determine if additional calibration accuracy can be achieved. Field experiments to check the spectral and radiometric calibration of AVIRIS in the air were conducted in the summer of 1987. Analysis of these data is just beginning. Additional experiments are planned for 1988 to check instrument performance after the upgrades are completed.

NASA is planning a data collection campaign with AVIRIS in 1988 for the atmospheric science, botany, geology, hydrology, oceanography, and remote sensing science communities. Part of the work in 1988 will be the completion of the data evaluation and technology assessment program begun in 1987. The remainder will be in support of ongoing research in the earth sciences. Data collection in 1988 will take place in the United States and Canada, but future deployments outside North America are already under consideration. AVIRIS is expected to be the major sensor for gathering high spectral resolution imagery across the 0.4 to 2.5 μm region until the launch of the Earth Observing System (Eos) in the mid-1990s. The goal of the AVIRIS project is to collect, process, and distribute consistent, well-calibrated data in support of the earth system science program leading to Eos and beyond.

4.0 ACKNOWLEDGEMENTS

During the past three years, 45 engineers, scientists and support personnel have worked hard at JPL to bring the AVIRIS system to completion. The author would like to express his deep gratitude to all those whose efforts have contributed to the success of this joint endeavor. The work described in this paper was carried out at the Jet Propulsion Laboratory, California Institute of Technology, under a contract with the National Aeronautics and Space Administration.

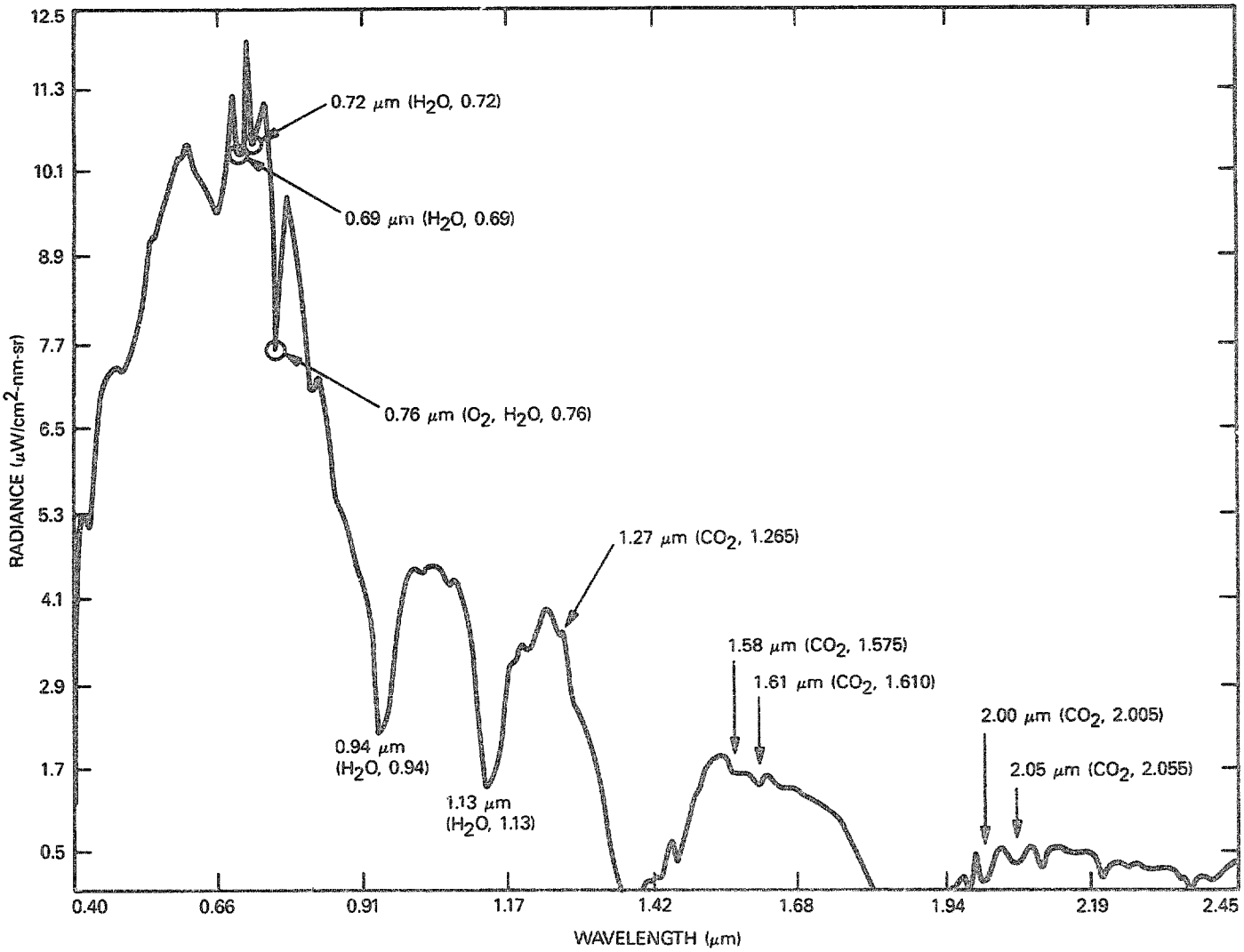

Figure 6. Full spectrum of a 5 by 5 pixel area in the center of Stonewall Playa. The data have been radiometrically corrected as described by Vane et al.[7] The wavelength positions of several atmospheric absorption features are indicated. The first number is derived from the AVIRIS data. In parentheses are the wavelength position of that feature from the LOWTRAN VI atmospheric model, and the atmospheric constituent(s) responsible for it.

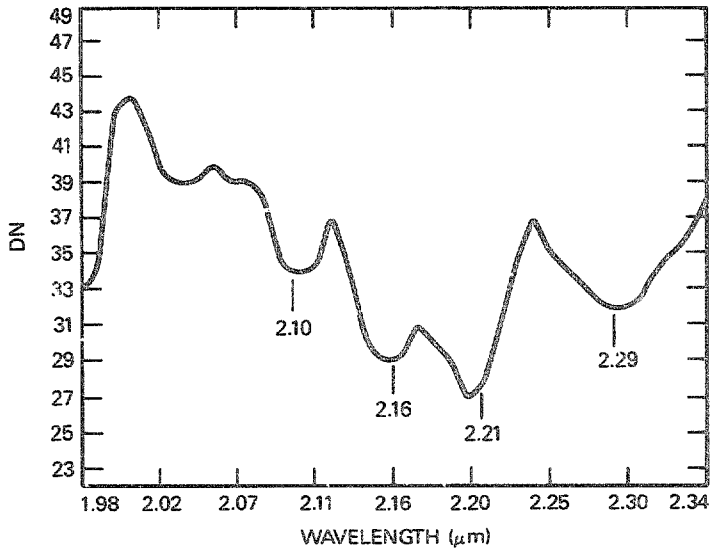

Figure 7. Single pixel spectrum from Kaolinite Hill showing the diagnostic double absorption feature at 2.16 and 2.21 μm due to the OH molecule in the kaolinite crystal lattice. The data were divided by the spectral reflectance curve in Figure 6 to remove the effects of solar insolation and atmospheric absorption.

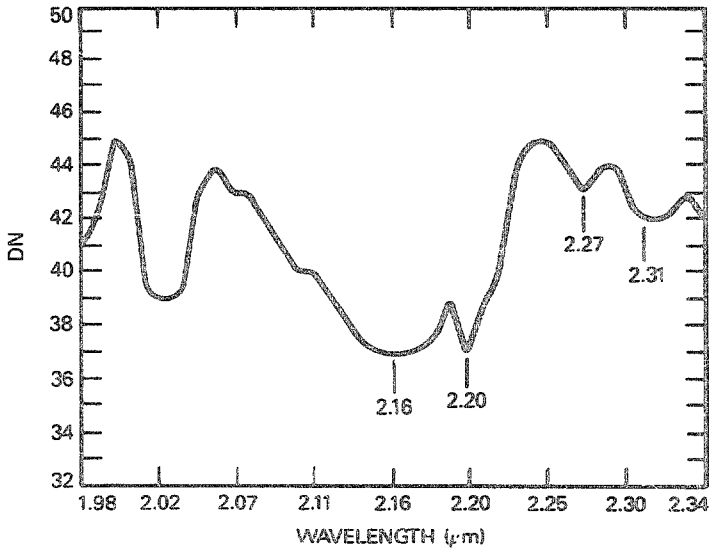

Figure 8. Single pixel spectrum of the mineral alunite from location C in Figure 5. The data were divided by the spectral reflectance curve in Figure 6 and show the diagnostic absorption feature at 2.16 μm resolved into its doublet. The secondary feature is at 2.20 μm.

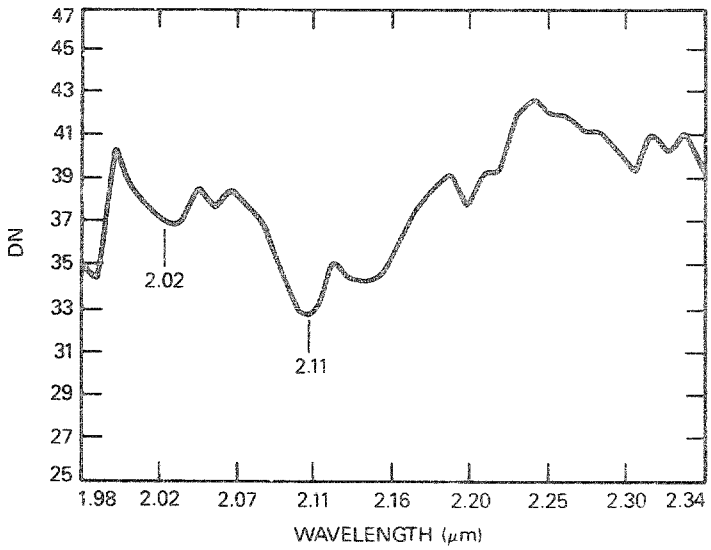

Figure 9. Single pixel spectrum of the mineral Buddingtonite from location D in Figure 5. The data were divided by the spectral reflectance curve in Figure 6. Characteristic absorption features at 2.02 and 2.11 μm identify this mineral.

5.0 REFERENCES

1. A. F. H. Goetz et al., "High resolution imaging spectrometer: Science opportunities for the 1990s," NASA TM 86129(2c) (1987).
2. G. Vane, M. Chrisp, H. Enmark, S. Macenka and J. Solomon, "Airborne Visible/Infrared Imaging Spectrometer: An advanced tool for earth remote sensing," Proc. 1984 IEEE Int'l. Geoscience and Remote Sensing Symposium, SP215, 751-757 (1984).
3. G. Vane and A. F. H. Goetz, "Terrestrial imaging spectroscopy," Remote Sensing of Environment, 24(1), in press (1987).
4. A. F. H. Goetz, G. Vane, B. N. Rock and J. E. Solomon, "Imaging spectrometry for earth remote sensing," Science, 228(4704), 1147-1153 (1985).
5. G. Vane, A. F. H. Goetz and J. B. Wellman, "Airborne Imaging Spectrometer: A new tool for earth remote sensing," IEEE Trans. on Geoscience and Remote Sensing, GE-22(6), 546-549 (1984).
6. W. M. Porter and H. T. Enmark, "A system overview of the Airborne Visible/Infrared Imaging Spectrometer (AVIRIS)," Proc. SPIE, 834 (1987).
7. G. Vane, T. G. Chrien, E. A. Miller and J. H. Reimer, "Spectral and radiometric calibration of the Airborne Visible/Infrared Imaging Spectrometer," Proc. SPIE, 834 (1987).
8. J. H. Reimer, J. R. Heyada, S. C. Carpenter, W. T. S. Deich and M. Lee, "AVIRIS ground data processing system," Proc. SPIE, 834 (1987).
9. M. J. Abrams, R. P. Ashley, L. C. Rowan, A. F. H. Goetz and A. B. Kahle, "Mapping of hydrothermal alteration in the Cuprite mining district, Nevada, using aircraft scanner images for the spectral region 0.46 to 2.36 μm," Geology, 5, 713-718 (1977).
10. A. S. Mazer, M. Martin, M. Lee and J. E. Solomon, "Image processing software for image spectrometry data analysis," Remote Sensing of Environment, 24(1), in press (1987).
11. R. N. Clark, T. King, M. Klejwa, G. A. Swayze and N. Vergo, "High spectral resolution reflectance spectroscopy of minerals," submitted to Jour. Geophysical Res. (1987).
12. C. Inouye, A. F. H. Goetz and S. Schultz, "Reflectance spectra of 156 minerals," JPL Publication in preparation, Jet Propulsion Laboratory, Pasadena, CA (1987).
13. A. F. H. Goetz and V. Srivastava, "Mineralogical mapping in the Cuprite mining district, Nevada," in Proceedings of the Airborne Imaging Spectrometer Data Analysis Workshop, Gregg Vane and Alexander F. H. Goetz, eds., JPL Publication 85-41, Jet Propulsion Laboratory, Pasadena, CA, 22-31 (1985).